이학박사 학위논문

형태가 제어된 반도체 기반 나노복합체의 응용에 관한 연구

Applications of Morphology-Controlled Semiconductor-Based Nanocomposites

2018 년 8 월

서울대학교 대학원
화학부 물리화학 전공
이 재 원

A Ph. D. Dissertation

Applications of Morphology-Controlled Semiconductor-Based Nanocomposites

By Jaewon Lee

Supervisor: Professor Du-Jeon Jang
Major: Physical Chemistry

Department of Chemistry
Graduate School of Seoul National University

August 2018

Abstract of Dissertation

Chapter 1 reports a brief overview of semiconductor nanomaterials havnig peculiar optical and physical properties. Especially, theses novel features are strongly related to three crucial parameters such as shape, size, and surface conditions. Thus, the size and shape-dependent phenomenon of nanosized-materials are explained in detail. In addition, efficient synthetic approaches, as well as application strategies, to well-defined nanocrystals with controlled shape and size are also described.

Chapter 2 describes that SnO_2/ZnS nanocomposites of SnO_2 quantum dots (QDs)-deposited ZnS nanorods having highly enhanced photocatalytic activity and photostability have been fabricated via a facile two-step hydrazine-assisted hydrothermal process without involving any surface treatments. A rational synthesis of high-quality SnO_2/ZnS heterojunction nanocomposites via a simple and friendly manner has been reported for the first time. Furthermore, The incorporation of SnO_2 QDs increases the photocatalytic efficiency of ZnS nanorods due to the following reasons: high separation of photogenerated charge carriers owing to type II band configuration, direct contact at interfaces, increased active surface sites, and extended the light absorption range to the visible region. Thus, our prepared SnO_2/ZnS nanocomposites are considered to have great potential for photodegradation nanocatalysts in the field of waste-water treatment.

Chapter 3 presents that Cu(I)-exchanged ZnS nanoadsorbents having highly efficient adsorption performances toward cationic dyes and heavy metals have been fabricated via facile cation exchange using pristine ZnS nanostructures as templates. Their surface properties such as surface charges and areas have been controlled by adjusting the molar ratio of Cu to Zn ($R_{Cu/Zn}$). The adsorption efficiency of Cu-exchanged ZnS nanoadsorbents is highest at a $R_{Cu/Zn}$ value of 0.4 because the net surface charges of the nanocomposites resulting from the substitution of Cu(I) ions for Zn(II) ions in the ZnS lattice are electronically most negative. Furthermore, the adsorption of cationic dyes to our nanoadsorbents is found to be mainly driven by attractive electrostatic interactions while van der Walls forces also play a role. Overall, our prepared Cu-exchanged ZnS nanoadsorbents are suggested to have great potential applicability in the treatment of wastewater containing cationic dyes or heavy metals.

In Chapter 4, the thickness and the morphologies of silver nanoshells have been tuned facilely and eco-friendly via laser irradiation. The irradiation of nanosecond laser pulses has transformed silver seeds or nanoparticles adsorbed to the silica surfaces of $Ag@SiO_2$ nanostructures into silver nanoshells, producing $Ag@SiO_2@Ag$ nanostructures having highly enhanced catalytic performances. The catalytic degradation of rhodamine B has been found to occur on silver nanoshells (k_1 process) or on core silver nanospheres (k_2 process); whereas the k_2 value changes hardly, the k_1 value increases largely by chemical reduction and/or laser treatment. Laser irradiation enhances the

catalytic performances of silver-based sandwich nanostructures by lowering the energy barrier (E_a) of the k_1 process, and E_a is reduced by the energetically favorable formation of the activated complex. The increment of catalytic performances resulting from the decrease of E_a has been considered to arise from the surface restructuring process, as well as the coverage increase, of silver nanoshells during laser irradiation.

Chapter 5 presents that SiO_2-coated Ag/Au composite hollow nanoboxes having high catalytic performances and enhanced catalytic reusability have been fabricated via a galvanic replacement reaction of SiO_2-coated silver nanocubes. Compared with SiO_2-coated Ag nanocubes, SiO_2-coated Ag/Au composite nanoboxes have been found to catalyze the degradation of 4-nitrophenol more rapidly in the presence of $NaBH_4$ due to their high surface area. In contrast to bare Ag/Au composite nanoboxes, SiO_2-coated Ag/Au composite nanoboxes can be recycled continuously for the catalytic degradation of 4-nitrophenol in the presence of $NaBH_4$. We consider that silica coating enhances the stability of Ag/Au composite nanoboxes enormously by blocking the dissolution and aggregation of nanoparticles thoroughly.

Keywords: Heterojunction, Hybrid nanostructures, Photocatalysts, Photoluminesence, Noble-metal

Student Number: 2012-23049

Table of Contents

List of Figures and Tables

Figure 1-10. Scheme of possible adsorption mechanisms. Reproduced from ref. 30.

Figure 2-1. TEM (left) and SEM (right) images of ZnS nanorods (top) and SnO_2/ZnS ($R_{Sn/Zn}$ = 0.10) nanocomposites (bottom).

Figure 2-2. TEM images of SnO_2/ZnS nanocomposites having $R_{Sn/Zn}$ values of 0.04 (a), 0.08 (b), 0.12 (c), and 0.15 (d); the arrows indicate SnO_2 quantum dots.

Figure 2-3. HRXRD patterns of SnO_2/ZnS ($R_{Sn/Zn}$ = 0.10) nanocomposites (a) and pristine ZnS nanorods (b). The standard diffraction lines of rutile SnO_2 and wurtzite ZnS are also shown for comparison.

Figure 2-4. HRTEM images (a and b) and SAED pattern (c), HAADF-STEM image (d), and EDX elemental mapping images (e–g) of a SnO_2/ZnS ($R_{Sn/Zn}$ = 0.10) nanocomposite.

Figure 2-5. Zn 2p (a), S 2p (b), Sn 3d (c), and O 1s (d) XPS spectra of SnO_2/ZnS ($R_{Sn/Zn}$ = 0.10) nanocomposites. The O 1s spectrum has been deconvoluted into three Gaussian curves.

Figure 2-6. UV-vis diffuse-reflectance spectra of SnO_2/ZnS nanocomposites with indicated $R_{sn/zn}$ values.

Figure 2-7. Decay kinetic profiles at 554 nm (a)**,** first-order decay profiles (b) and degradation rate constants (c) of RhB via SnO_2/ZnS nanocomposites with indicated $R_{Sn/Zn}$ values.

Figure 2-8. N_2 adsorption-desorption isotherms (a) and pore-size distributions (b) of SnO_2/ZnS nanocomposites with indicated $R_{Sn/Zn}$ values.

Figure 2-9. PL spectra (a) and emission decay profiles at 325±20 nm (b) of SnO_2/ZnS nanocomposites with indicated $R_{Sn/Zn}$ values. Samples were suspended in ethanol and excited with 266 nm laser pulses.

Figure 2-10. First-order decay profiles of RhB via pristine ZnS (a) and SnO_2/ZnS ($R_{Sn/Zn}$ = 0.10) nanocomposites (b) in the presence of indicated scavengers. PL spectra of TAOH generated by light irradiation in the presence of SnO_2/ZnS ($R_{Sn/Zn}$ = 0.10) nanocomposites for durations indicated in the units of min (c).

Figure 2-11. Schematic for the degradation mechanism of RhB over a SnO_2/ZnS heterojunction nanostructure under light irradiation.

Figure 2-12. Stability test of SnO_2/ZnS ($R_{Sn/Zn}$ = 0.10) nanocomposites (a) and pristine ZnS nanorods (b) via repeated photocatalytic RhB-degradation experiments.

Table 2-1. Catalytic degradation rate constants, BET surfaces areas, and average pore sizes of nanocatalysts.

Table 2-2. PL intensities and emission decay kinetic constants of SnO_2/ZnS nanocomposites with indicated $R_{Sn/Zn}$ values suspended in ethanol.

Figure 3-1. TEM (left) and SEM (right) images of Cu-exchanged ZnS ($R_{Cu/Zn}$ = 0.4) nanosheets (a), nanobelts (b), and nanorods (c).

Figure 3-2. HRXRD patterns of Cu-exchanged ZnS nanorods with indicated $R_{Cu/Zn}$ values. The standard diffraction lines of orthorombic Cu_2S and wurtzite ZnS are also shown for comparison.

Figure 3-3. HRTEM images (a and b) and FFT pattern (c) of a Cu-exchanged ZnS ($R_{Cu/Zn}$ = 0.4) nanorod. The yellow marks of the panel a and the yellow lines of the panel b indicate stacking faults and planar defects, respectively, while the red lines of the panel b and the red arrows of the panel c designate lattice alignments and defect sites, respectively.

Figure 3-4. HAADF STEM image (a), EDX elemental mapping images (b-d), and area-normalized line-scanned elemental intensity profiles (e) of a Cu-

exchanged ZnS ($R_{Cu/Zn}$ = 0.4) nanorod for Zn, Cu, and S along the indicated line of the insetted HAADF STEM image.

Figure 3-5. Zn 2p (a), S 2p (b), Cu 2p (c), and O 1s (d) XPS spectra of Cu-exchanged ZnS ($R_{Cu/Zn}$ = 0.4) nanorods. The S 2p spectrum has been deconvoluted into two Gaussian curves.

Figure 3-6. Absorption spectra of RhB after adsorption on Cu-exchanged ZnS nanosheets (a), nanobelts (b), and nanorods (c) with indicated $R_{Cu/Zn}$, where 'free' indicates nanocomposites-free. Removal percentages of RhB depending on the $R_{Cu/Zn}$ values of indicated nanocomposites (d). (RhB concentration, 10 μM; adsorbent dosage, 0.125 g/L; contact time, 180 min)

Figure 3-7. Dosage effect of indicated Cu-exchanged ZnS nanoadsorbents with a $R_{Cu/Zn}$ value of 0.4 on the removal percentage of RhB.

Figure 3-8. Time-dependent q_t of RhB having indicated various initial concentrations in the presence of Cu-exchanged ZnS ($R_{Cu/Zn}$ = 0.4) nanosheets (a), nanobelts (b), and nanorods (c).

Figure 3-9. $R_{Cu/Zn}$-dependent zeta potentials of indicated Cu-exchanged ZnS nanoadsorbents.

Figure 3-10. N_2 adsorption-desorption isotherms (a) and pore-size distributions (b) of indicated Cu-exchanged ZnS nanoadsorbents.

Figure 3-11. Absorption spectra (a) and removal percentages (b) of RhB after indicated different cycles. TEM images of Cu-exchanged ZnS ($R_{Cu/Zn}$ = 0.4) nanoadsorbents reused for indicated cycle times (c), where each scale bar indicates 300 nm. (RhB concentration, 10 μM; adsorbed dosage, 0.125 g/L; contact time, 180 min).

Table 3-1. Kinetic and intra-particle diffusion parameters for adsorption of RhB on Cu-exchanged ZnS ($R_{Cu/Zn}$ = 0.4) nanorods at different initial RhB concentrations.

Table 3-2. Langmuir and Freundlich isotherm parameters for adsorption of RhB onto Cu-exchanged ZnS ($R_{Cu/Zn}$ = 0.4) nanoadsorbents.

Figure 4-1. Schematic illustration of processes to produce Ag@SiO_2@Ag sandwich nanostructures. The orange indicates silver while the blue indicates silica.

Figure 4-2. TEM images of (a) Ag@SiO_2, (b) Ag@SiO_2@Ag_{seeds}, and (c) Ag@SiO_2@Ag_{NPs} nanostructures (left) before and (right) after irradiation with 355 nm pulses of 6 ns for 30 min. Each scale bar indicates 100 nm.

Figure 4-3. EDX elemental maps and area-normalized line-scanned elemental intensity profiles of a Ag@SiO_2@Ag_{NPs} nanostructure (a) before and (b) after irradiation with 355 nm for 30 min for (red) Ag, (green) Si, and (blue) O along the indicated lines of the insetted STEM images. Note that the actual particle transformed into the particle in (b) is different from the particle in (a).

Figure 4-4. Maximum-normalized surface-plasmon resonance spectra of (blue) Ag@SiO_2, (green) Ag@SiO_2@Ag_{seeds}, and (red) Ag@SiO_2@Ag_{NPs} nanostructures (a) before and (b) after irradiation with 355 nm pulses of 6 ns for 30 min.

Figure 4-5. Absorption spectra at 30 °C of KBH_4-added aqueous RhB solutions, measured at elapsed times indicated in the units of min after adding aqueous colloidal solutions of (a) Ag@SiO_2, (b) Ag@SiO_2-L, (c) Ag@SiO_2@Ag_{seeds}, (d) Ag@SiO_2@Ag_{seeds}-L (e) Ag@SiO_2@Ag_{NPs}, and (f) Ag@SiO_2@Ag_{NPs}-L nanoparticles.

Figure 4-6. $\ln(A/A_0)$ vs. t for the catalytic degradation of 11 μM RhB(aq) in the presence of 1.1 mM KBH_4 at temperatures indicated in the units of °C via

nanocatalysts of (a) $Ag@SiO_2$, (b) $Ag@SiO_2$-L, (c) $Ag@SiO_2@Ag_{seeds}$, (d) $Ag@SiO_2@Ag_{seeds}$-L, (e) $Ag@SiO_2@Ag_{NPs}$, and (f) $Ag@SiO_2@Ag_{NPs}$-L.

Figure 4-7. Arrhenius plots for (a) the k_1 and (b) the k_2 catalytic-degradation rate constants of 11 μM RhB(aq) in the presence of 1.1 mM KBH_4 via nanocatalysts of (closed squares) $Ag@SiO_2@Ag_{seeds}$, (open squares) $Ag@SiO_2@Ag_{seeds}$-L, (closed circles) $Ag@SiO_2@Ag_{NPs}$, and (open circles) $Ag@SiO_2@Ag_{NPs}$-L.

Figure 4-8. Compensation law plots for (a) the k_1 and (b) the k_2 catalytic-degradation rate constants of (closed squares) $Ag@SiO_2@Ag_{seeds}$, (open squares) $Ag@SiO_2@Ag_{seeds}$-L, (closed circles) $Ag@SiO_2@Ag_{NPs}$, and (open circles) $Ag@SiO_2@Ag_{NPs}$-L.

Figure 4-9. First-order kinetics, $\ln(A/A_0)$ vs. t, for the catalytic degradation of 11 μM RhB(aq) via $Ag@SiO_2@Ag_{NPs}$-L nanostructures in the presence of 1.1 mM KBH_4 at 30 ˚C, for five indicated recycles.

Table 4-1. Rate Constants (k) and Induction Times (t_o) at 30 °C, Activation Energies (E_a), Frequency Factors (A), Activation Enthalpies ($\Delta H^{\ddagger}$), and Activation Entropies ($\Delta S^{\ddagger}$) for the Catalytic Degradation of Rhodamine B via Silver-Based Nanocatalysts in the Presence of KBH_4.

Figure 5-1. TEM images of (a) Ag nanocubes, (b) Ag/Au alloy nanoboxes, (c) SiO_2-coated Ag nanocubes, and (d) SiO_2-coated Ag/Au composite nanoboxes.

Figure 5-2. (a) Area-normalized EDX line-scanned elemental intensity profiles of a SiO_2-coated Ag/Au composite nanobox for (squares) Au, (circles) Ag, (triangles) Si, and (crosses) O along the indicated dashed line of the insetted STEM image. (b) EDX elemental maps of the above STEM image.

Figure 5-3. Peak-normalized absorption spectra of (squares) Ag nanocubes, (triangles) SiO_2-coated Ag nanocubes, (diamonds) Ag/Au composite

nanoboxes, and (circles) SiO_2-coated Ag/Au composite nanoboxes suspended in water.

Figure 5-4. Absorption spectra of $NaBH_4$-added aqueous 4-nitrophenol solutions, measured at elapsed times indicated in the units of min after adding aqueous colloidal solutions of (a) SiO_2-coated Ag/Au composite nanoboxes and (b) SiO_2-coated Ag nanocubes at 25 ^oC. (c) Decay kinetic profiles at 400 nm of the above described absorption spectra of (closed) SiO_2-coated Ag nanocubes and (open) SiO_2-coated Ag/Au composite nanoboxes.

Figure 5-5. First-order kinetics, $\ln(A/A_0)$ vs. time, for 4-nitrophenol catalyzed by using (a) SiO_2-coated Ag nanocubes and (b) SiO_2-coated Ag/Au composite nanoboxes at different temperatures of (squares) 10, (circles) 25, and (triangles) 40 ^oC. (c) Arrhenius plots for the reduction reaction of 4-nitrophenol catalyzed by (open) SiO_2-coated Ag/Au composite nanoboxes and (closed) SiO_2-coated Ag nanocubes in the presence of $NaBH_4$.

Figure 5-6. Absorption-decay kinetic profiles of 4-nitrophenol catalyzed by (open) SiO_2-coated Ag/Au composite nanoboxes and (closed) bare Ag/Au composite nanoboxes, recycled at (circles) the third time and (squares) the fourth time, in the presence of $NaBH_4$ at 25 ^oC.

Figure 5-7. TEM images of (a) SiO_2-coated Ag/Au composite nanoboxes before a catalysis experiment, and (b) SiO_2-coated composite Ag/Au nanoboxes after running catalysis experiments 5 times.

Table 5-1. Comparison of rate constants, frequency factors, and activation energies for the reduction of 4-nitrophenol via SiO_2-coated nanocatalysts in the presence of $NaBH_4$.

Chapter 1. General Introduction

1.1. Physical Properties of Nanosized Materials

The physical properties of nano-sized materials differ fundamentally from those of the bulk-sized ones as the material size approaches quantum mechanical scale.[1] Optimization of structure, morphology, and electronic is of fundamental importance for the design of nanostructures with favorable properties. Especially, the decrease in the particle size from bulk to nanoscale are ascribable to increase in the surface energy.[2] Due to the fine grain sizes and consequently high density of interfaces, nanomaterials show a variety of properties as above mentioned; these include increased strength/hardness, enhanced diffusivity, higher electrical resistivity, increased surface area, higher coefficient of thermal expansion, and lower thermal conductivity. The diverse physical properties of nanomaterial are described in the following sentences.

Optical Properties. Nanomaterials have attracted significant interests for their novel optical properties, which is remarkably different compared with bulk-sized materials.[1,2] With the increase of nanotechnology, it is essential to understand the detailed concepts for photonic properties of nanoparticles. The optical properties of nanomaterials can be finitely controlled by adjusting the dimensions, shape, and size of nanocrystals. In particular, in the case of optical absorption of semiconductor-based nanostructures, optical spectroscopy show the energy difference between electronic states. The reduction in particle size shifts the absorption edge from the infrared to the visible region, resulting in the increase in the band gap energy of semiconductor (Figure 1-1).[3] Meanwhile,

photoluminescence (PL) can be defined as the emission of light when excited with light irradiations such as X-ray/UV/electrons (Figure 1-2).[4] Optical excitation of semiconductor nanoparticles often leads to both band-edge and shallow/deep trap emission. The size dependence of the excitonic emission has been investigated reasonably through the effective-mass approximation process.[5] The PL in semiconductor nanoparticles is quite complex and most nanoparticles exhibit broad and Stokes-shifted luminescence arising from the traps of surface states. As the nanoparticles become smaller, the amounts of surface states and surface/volume ratio increases gradually, reducing the excitonic emission. Thus, surface states can determine the physical properties, especially the optical properties of nanoparticles.

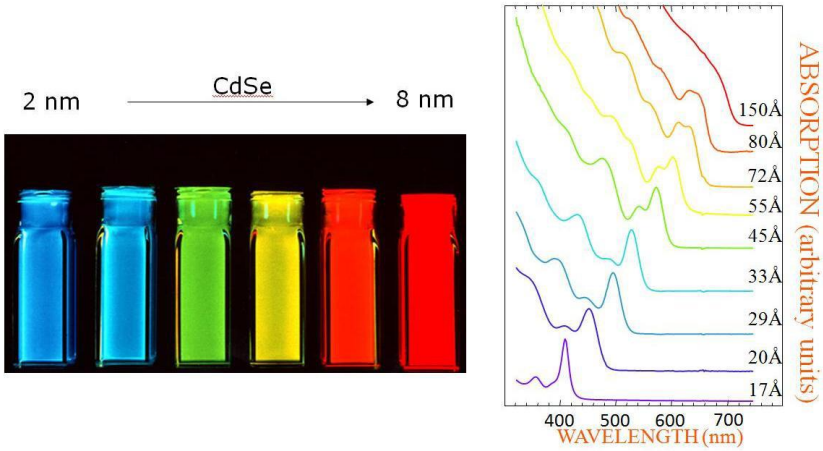

Figure 1-1. Size dependence of the optical absorption spectra of colloidal CdSe nanoparticles. Reproduced from ref. 3.

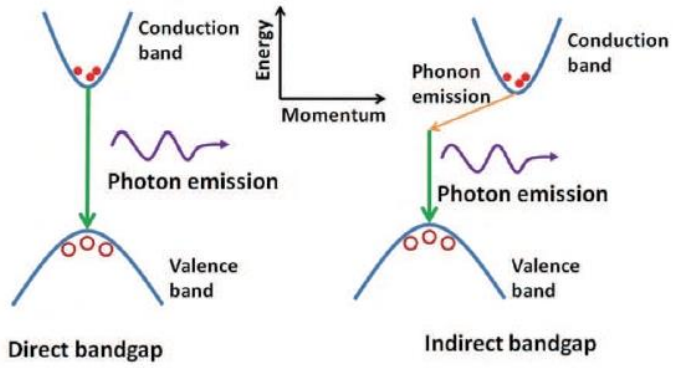

Figure 1-2. Photon emission process in the direct bandgap and indirect bandgap semiconductors. Reproduced from ref. 4.

The optical properties of metallic nanomaterials are also determined by size and morphologies.[5-8] Colloidal solutions of the noble metals such as gold, silver, and copper exhibit the characteristic colors which have received significant interest from researches (Figure 1-3).[7] The physical origin of the light absorption by metal nanostructures is the coherent oscillation of the electrons in conduction band, which are induced by interacting electromagnetic field. The electromagnetic waves can also propagate along the interface between conducting materials and a dielectric over a broad range of frequencies. The oscillation modes comprise an electromagnetic field coupled to the oscillations of electrons and are called surface plasmons.[9] The SPR spectra of noble-metal nanostructures can be also calculated by resolving the Maxwell's equations. The theory has been developed and modified by many researchers, resulting in the invention of Mie theory.[6-9] Later, this theory was further extended to apply to describe the optical properties of metallic spherical nanoparticles.

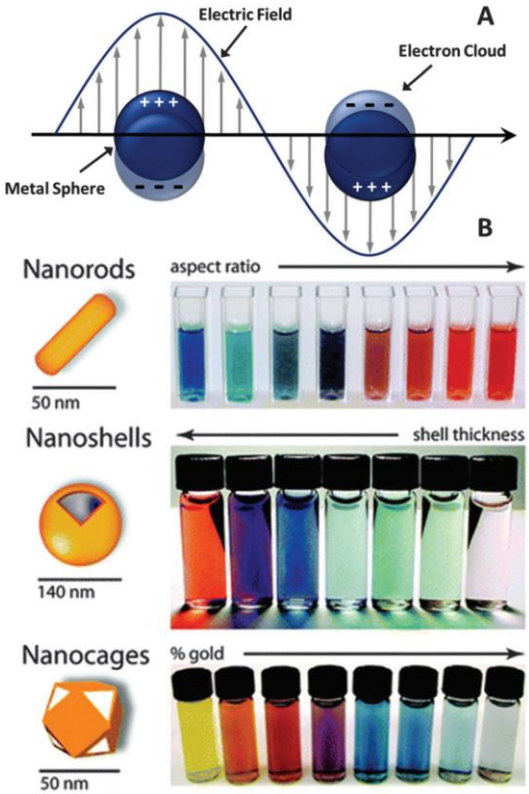

Figure 1-3. Schematic illustrating a localized surface plasmon on a metal nanoparticle. Reproduced from ref. 7.

Electronic Properties. The electrical conductivity of the materials is regulated by its electronic structure as well as band structure (Figure 1-4).[10] A metallic materials indicated that the uppermost energy band is partly filled or totally filled and the next unoccupied band overlap in energy. On the other hand, in the case of semiconductors, the completely filled valance band (VB) and the empty conduction band (CB) are separated by an energy bandgap (<3 eV).[2,6] The electrons can be excited from the VB to CB by light or heat, showing the partial conductivity. Diverse parameters such as temperature, light intensity, and size can also affect the instinctive conductivity of the materials. As the

particle size is decreased to nanometer scale, the band gap increases progressively, resulting in the reduction of conductivity.[10] As for metal nanoparticles, the density of states (DOS) in the CB and VB are decreased and electronic properties changed together; the quasi-continuous DOS is replaced by quantized levels with a size dependent, revealing that the metal does not show bulk metallic or semiconducting properties.[11]

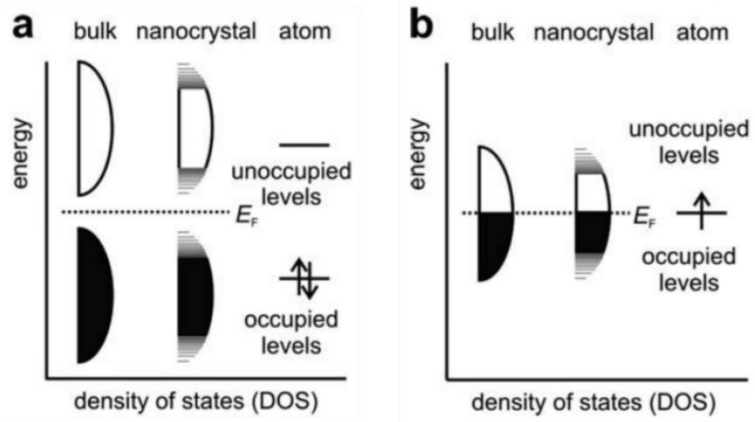

Figure 1-4. Schematic illustration of the density of states going from bulk (left) to nanocrystal (middle) to an isolated atom (right) for semiconducting (a) and metallic materials (b). Reproduced from ref. 10.

1.2. Fabrication and Morphology Control of Nanostructures

Nanomaterials play a key role for applications of nanoscience and nanotechnology such as energy sources, environment, health, and medical treatments. Thus, the continuous and in-depth research of nanomaterials are placed in a significantly important position. The factors driving the current attention in nanoparticle research is the perceived need not only for further

miniaturization of both optical and electronic devices, but also for the engineering of the anisotropy nanostructure from zero to three dimension (Figure 1-5).[12] Furthermore, precise control of parameters such as size and shape shows unique properties of the nanostructures as well as chemical and physical properties adjusted as desired.[13,14] Thus, researchers have investigated efficient synthetic routes of well-defined inorganic nanostructures with a tunned size and shape.

Critical Factors of Structure and Morphology Determination. Nanostructure formation can be simply divided in two-step processes; first, nucleation has been initiated by sudden increase of monomer concentration up to super-saturation levels; second, the continuous growth from the crystal seeds has taken place with consumption of monomers (Figure 1-6).[13] The structure and morphology of nanocrystals is affected by several factors during these nucleation and growth processes.[14] Initially, the crystal phase of the seed at nucleation steps is the critical factor for morphology of nanocrystal because of its characteristic unit cell structure.[1] When the nanocrystal seeds are organized with a specific crystal phase, several parameters for tuning the subsequent growth progress can influence the final morphology of nanocrystals; the key parameters are as following; the comparative nanocrystal growth regime between kinetic and thermodynamic procedure, the role of surface selective capping agents, and the intrinsic surface energy of different crystallographic surfaces.[15]

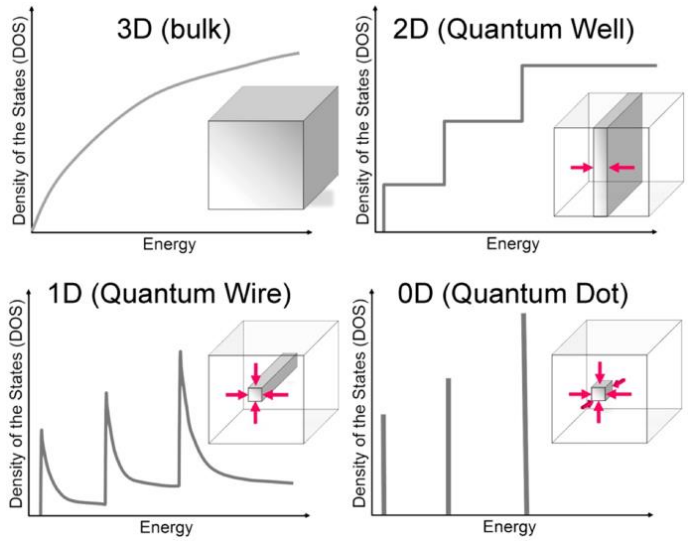

Figure 1-5. Electronic DOS for a bulk 3D crystalline material, a 2D QW, a 1D NW or NT, and a 0D QD. The insets report a cartoon showing the corresponding spatial confinement: confinement directions are defined by arrows. Reproduced from ref. 12.

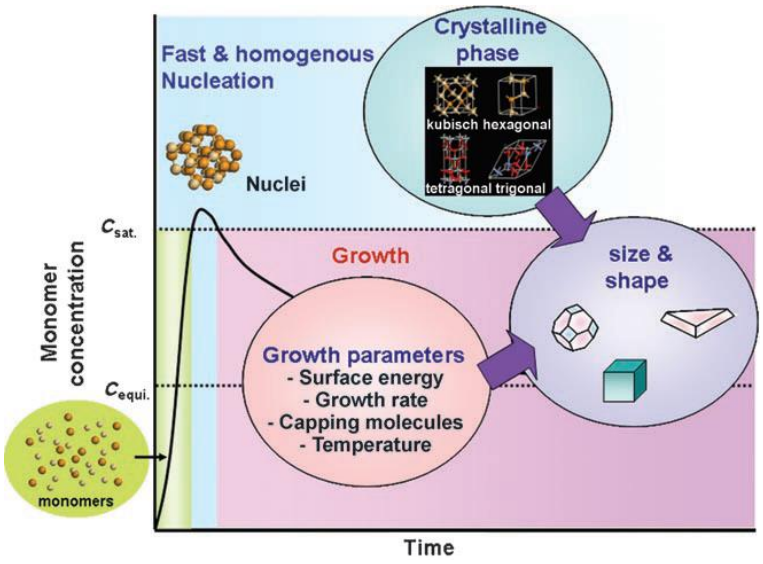

Figure 1-6. Crystal growth processes and key factors for shape determination. Reproduced from ref. 13.

Types of Alloy Nanocrystals. Alloy nanocrystals are significantly important in diverse areas of nanoscale engineering due to the continuous control of their physical and optical properties via the gradual variation of their composition.[16] Alloyed semiconductor-based nanomaterials offer wealth of opportunities for the adjusted development of new materials and devices, such as electronic devices, light-emitting diodes, electromagnetic-radiation detectors, catalysts, and biological labels.[11] Semiconductor alloys are also categorized into the following groups; (a) binary alloys: mixtures of two elemental semiconductor, (b) pseudo binary(commonly "ternary") alloys: ternary alloys are mixtures of two compound semiconductor where only one element is changed, keeping the remaining elements in common, (c) pseudoternary, quaternary or higher order alloys: mixtures of three, four, or more compound semiconductors.[16]

Alloying semiconductors influence the energy band structure and minimum energy gap, lattice parameter, mechanical constants, optical and electronic conduction properties, and other aspects of the resulting material. The lattice parameter can be estimated reasonably using Vegard's Law, which describes that the lattice constant of an alloy crystal: $E_{alloy} = xE_A + (1-x)E_B$, x is the mole fraction, E_A,E_B and E_{alloy} are the band-gap energy of pure composition A, pure composition B, and the alloyed material, respectively.[16] Briefly, the lattice constant can change linearly with composition of the alloy from that of one compound or elemental constituent to that of the other.[11] Most mechanical properties also shift linearly with alloy composition as these properties are affected by substantial volumes of the semiconductor crystal. Meanwhile,

optical and electronic properties are determined by very small voumes of semiconductor crystal and do not scale simply with composition.

Types of Core/Shell Nanocrystals. Two core/shell types are categorized as type I and type II band alignment, respectively.[2] The type I core/shell has a larger band gap of the shell than the core, and consequently both the charge carriers confined in the core. As for type II structure, either the valence band edge or the conduction band edge of the shell is located in the band gap of the core; the staggered band structure is attributable to separation of the charge carriers in the different regions of the core/shell structure.[17] Type I heterojunction nanostructures underwent optical transition between the electron and hole states, whose wave functions are localized in the same region in real space. On the other hand, as to type II heterojunction nanostructures, the electron and hole lie in different regions. In type I nanocomposites, the shell is employed to 'passivate' the surface of the core, with the purpose to improve its optical properties. The shell separates physically the optically active surface core nanocrystal from its surrounding medium.[2] Thus, the sensitivity of the optical properties changes in the local environment of the nanocrystal surface. With respect to the core, the core/shell systems can also enhance the stability against photodegradation. At the same time, the shell growth reduces the number of surface dangling bonds, which can act as trap states for charge carriers and reduce the fluorescence quantum yield (QY).[18]

In type II systems, the shell growth aims at a significant red shift of the emission wavelength of the nanocrystals. The staggered band alignment leads

to a smaller effective band gap, than that of each one of the constituting core and shell materials.[19] These systems tune the emission color with the shell thickness towards spectral ranges, which are difficult with other materials. In contrast to the type I systems, the PL decay times are strongly prolonged in type II core/shell nanostructures, due to the lower overlap of the electron and hole wave functions. As one of the charge carriers (electron or hole) is located in the shell, an over growth of type II core/shell nanostructures with an outer shell of an appropriate material can be used in the same way as in type I systems, to improve the fluorescence QY and photostability.[2]

Various methods have been employed not only for the synthesis of nanostructures, but also for the fabrication of nanocomposites such as alloy and core/shell structures. Two main classes can be divided; first and second is bottom-up and top-down approach, respectively, as indicated in Figure 1-7.[2] In the case of top-down method, destructive process is necessary; larger molecules are decomposed into smaller units and then transformed into suitable nanoparticles. Examples of this method are nanolithography, laser ablation, sputtering, grinding/miling, and other decomposition approaches.[6] Furthermore, it was determined that the size of nanocrystals decreases with the increase of the time.

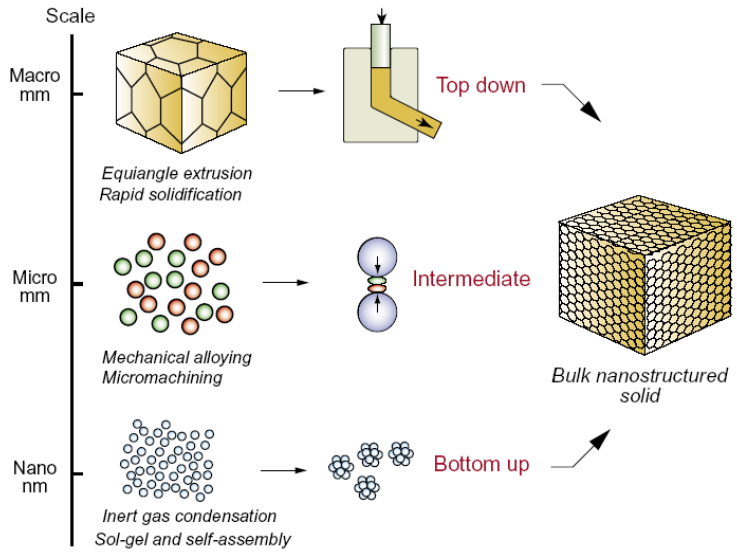

Figure 1-7. The top-down, intermediate and bottom-up approaches to fabricate bulk nanostructures. Reproduced from ref. 2.

Laser Ablation. Laser Ablation Synthesis in Solution (LASiS) is a unique method for fabrication of nanoparticles in various solvents.[2,6] The irradiation of a metal submerged in a liquid solution by a laser beam having diverse energy and pulse duration condenses a plasma plume that finally produces nanoparticles. The main advantages of the LASiS are as follows:[20] the method is clean and convenient as chemical reducing reagents are not essential; the formation of nanoparticles can be controlled facilely by adjusting laser irradiation; the method can be also conducted in diverse media such as surfactant micelles, polymer films, and glasses. LASiS technique could be used as a powerful tool for the controlled reshaping and resizing of wet-chemically produced nanoparticles via the melting, fragmentation, and vaporization of metal nanoparticles with the thermalized photon energy of surface plasmon

resonances since metallic nanoparticles exhibit depression in melting and boiling temperatures and thermal conductivity with a decrease in their sizes. Thus, the synthesis and modification of nanostructures in liquids based on laser irradiation have recently become a rapidly growing field because, compared to other chemical methods, LASiS method is a “simple” and “green” technique that normally operates in both aqueous and nonaqueous solutions under ambient conditions

Sputtering. Sputtering is the deposition of nanoparticles on a surface by ejecting particles from it via colliding between ions and substrate.[2,6] Sputtering is usually a deposition of thin layer of nanoparticles after annealing process. The thickness of the layer, temperature and duration of annealing, substrate type are important factors to affect shape and size of the nanostructures.[22] On the other hand, in the case of bottom-up process, this approach is utilized in reverse because nanoparticles are produced from relatively small molecules. Thus, its process can be also called building up approach. Examples of this process are sedimentation and reduction techniques such as sol gel, hydrothermal/sovolthermal, spinning, chemical and physical vapor deposition, and biochemical synthesis.

Sol-Gel. The sol-gel is the one of the most preferred bottom-up approach owing to its simplicity.[2,6] Furthermore, most of the nanostructures can be fabricated through this method. Ultrafine particles, nanothickness films, and nanoporous membranes are made by this process.[21] It is a wet-chemical process having a chemical solution acting as a precursor for an integrated system of

discrete particles. Especially, metal oxides and chlorides are usually used as precursors in sol-gel process. The precursor is dispersed in a host liquid either by shaking, stirring or sonication and the resultant system contains a liquid and a solid phase.

Spinning. The fabrication of nanoparticles by spinning is conducted via a spinning disc reactor (SDR).[2,6] It contains a rotating disc inside a chamber/reactor where the physical parameters such as rotation speed and temperature can be adjusted. The reactor is generally filled with N or other inert gases to remove oxygen inside not only to prevent the oxidation reaction but also retard the generation of side product.[23] The disc is rotated at different speed where the liquid precursor and water is pumped in. The spinning can influence the atoms or molecules to fuse together, which is precipitated, collected and dried to produce the nanoparticles. The various operating parameters, such as the liquid flow rate, disc rotation speed, liquid/precursor ratio, location of feed, disc surface, are key factors to affect the characteristics nanoparticles obtained from SDR technique.

Chemical Vapor Deposition (CVD). Chemical vapor deposition is the deposition of a thin film of gaseous reactants onto a substrate.[2] The deposition is carried out in a reaction chamber at ambient temperature by combining gas molecules. The deposit can be produced by a reaction between precursor gases in the vapor phase or by a reaction between a vapor and the surface of the heated substrate itself.[24] Substrate temperature is the influencing factor in CVD. Coating on the surface via CVD technique are typically amorphous and

nanocrystalline as their formation is not dependent on equilibrium thermodynamic constraints any more. The advantages of CVD are highly pure, uniform, hard and strong nanoparticles. The disadvantages of CVD are the requirement of special equipment and the gaseous by-products are highly toxic.

Solvorthermal/Hydrothermal. The solvothermal approach of synthesizing materials is the most preferred and common method for materials scientists and chemists.[2,6] Solvothermal reactions have been mainly employed for preparing micro or nanoparticles with diverse morphologies.[19] The solvothermal technique finds an increasing use in nanotechnology and offers a unique means of making highly functionalized materials, for applications such as sensors, separation and catalysis, molecular devices and spintronics due to envirnmenatal friendliness, easy upward scaling, and low production cost. The solvothermal process can be also described as following: "A chemical reaction in a closed system in the presence of a solvent such as aqueous and non-aqueous solution at a temperature higher than that of the boiling point of such a solvent". The solvothermal process contains high pressures as well. The selected temperature depends on the required reaction for producing the target material through the involved process. Meanwhile, as for an aqueous solution as a solvent, hydrothermal technology has been researched and developed with different purpose. Especially, the hydrothermal process having water as the solvent is principally appropriate to the fabrication of hydroxides, oxihydroxide or oxides versus the temperature value. The development of non-oxide metals such as nitrides and calcogenides for investigating their physical properties and

industrial applications requires the progress of a new approach with non-aqueous solvents. Consequently, solvothermal reaction is a generic synthesis for a chemical reaction in a closed system in the presence of a organic solvent while hydrothermal reactions are mostly developed with non-aqueous solvents for preparing non-oxide materials.

1.3. Applications of Nanomaterials

Multi-dimensional nanocomposites having diverse optical and electronic properties and chemical reactivities have been investigated as they exhibit high possibilities in application such as electronics, catalysis (or photocatalysis) renewable energy and environmental remediation.

Electronics. The development of high brightness displays are necessary to use in the computer monitors and television, facilitating the use of nanoparticles in the display technology.[2,6] Especially, nanosized-crystalline lead telluride, cadmium sulfide, zinc selenide and sulfide are typically employed in the light emitting diodes of modern displays.[25] The progress in portable electronics such as mobile phones and laptop computers result in the huge demand for a compact, slim, lightweight and high capacity batteries. A significant energy can be stored compared with traditional batteries because of their aerogel structure. Batteries produced from nanostructures of nickel and metal hydrides lead to less recharging and last longer owing to their large surface area. The increase in

electrical conductivity of nanoparticles are also utilized to detect gases like NO_2 and NH_3, arising from the increase in the pores of nanoparticles.

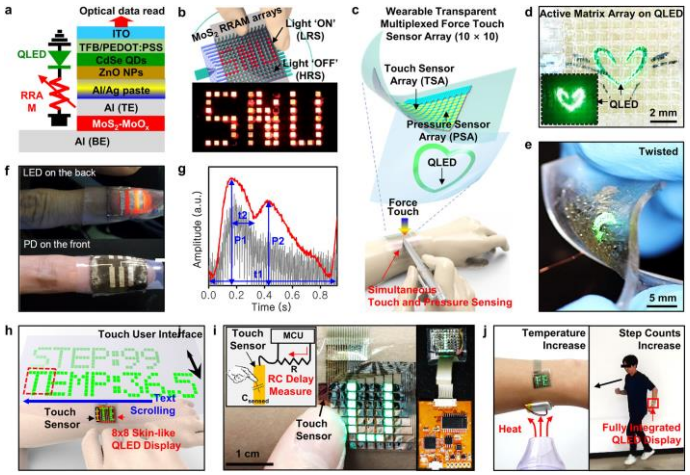

Figure 1-8. Wearable quantum dot light-emitting diodes with other electronic devices. Reproduced from ref. 25.

Catalysis and Photocatalysis. As we mentioned above, nanostructures have high surface area, providing a high catalytic performance.[2,6] Because of their extremely large surface to volume ratio, the nanoparticles can operate as efficient catalyst. For example, one of the important application is the use of platinum-based nanoparticles in the automotive catalytic converters since they decrease the amount of platinum required, thus reducing the cost significantly as well as improving performance. Nanotechnology has also developed the construction processes via making them quicker, inexpensive and safer. When nano-sized silica is mixed with the normal concrete, the nanoparticles can enhance its mechanical properties, and also improvements in durability. In addition, since TiO_2 nanoparticles has sterilizing and anti-fouling properties

and catalyze powerful chemical reaction that decompose volatile organic compound and organic pollutants.[19,20] Briefly, among the various proposed technologies and sciences, semiconductor-based photocatalysts has high potential as it directly uses solar energy both for the generation of valuable chemical fuels such as hydrogen and hydrocarbon fuels and for the decomposition of organic pollutants.[26] Because the pioneering work on photocatalysis by Honda and Fujishima in 1972, many researchers have been studied and developed for various photocatalytic applications as well as enhanced photocatalytic performances.[27] However, the practical applications of photocatalysis are still limited due to its low photocatalytic activity and durability. The photocatalytic reaction follows five main steps basically: 1) light absorption by the semiconductor, 2) generation of photogenerated electron–hole pairs, 3) migration/transportation and recombination of the photogenerated charge carriers on the surface, 4) adsorption of reactants and desorption of products, and 5) redox reactions on the semiconductor surface.[27] Among these process, the recombination of electron– hole pairs provides a negative effect on the photocatalytic efficiency. During photocatalytic reaction, the photogenerated charge carriers can either transfer to the photocatalyst surface and initiate redox reactions, or recombine and create useless heat. Thus, further development of new photocatalyst materials for the design and fabrication of photocatalysts is the important research goals. The practically employed photocatalysts contain various drawbacks such as high cost, large bandgaps, and low active surface area. It is of great significance to discover

cost-effective and advanced materials to prepare high efficient photocatalysts for practical applications. A ideal type of material for engineering a photocatalyst should accomplish several requirements, such as visible-light activity, high solar-conversion efficiency, proper bandgap structure for redox reactions, high photostability for long-term applications, and scalability for commercialization.

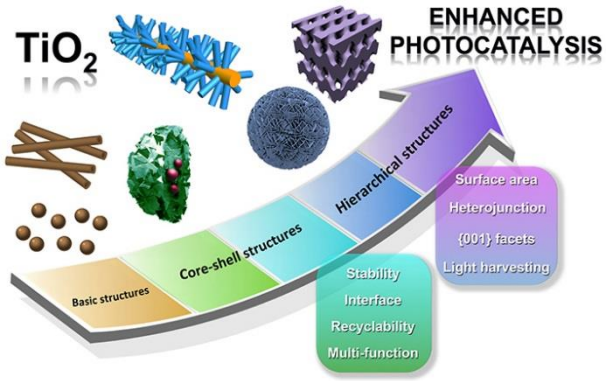

Figure 1-9. Schematic diagram of various structured photocatalysts according to their functions. Reproduced from ref. 26.

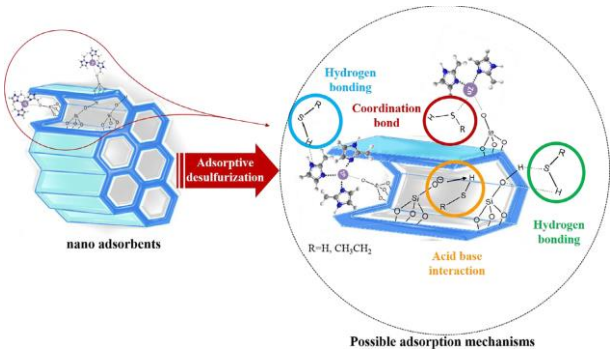

Figure 1-10. Scheme of possible adsorption mechanisms. Reproduced from ref. 30.

Adsorption. Adsorption has been commonly employed as a polishing step to remove organic and inorganic contaminants such as organic dyes and heavy metals in water and wastewater treatment. Efficiency of conventional adsorbents is usually limited by the surface area or active sites, the lack of selectivity, and the adsorption kinetics. Meanwhile, nanoadsorbents can provide significantly enhanced-adsorption performances with their extremely high specific surface area and related sorption sites, short inter/intraparticle diffusion distance, and tunable pore size and surface chemistry.[28] Most extensively used are carbon-based adsorbents, which are suitable for the elimination of traditional pollutants such as dyes, phenols, organic acids, and heavy metals. In particular, graphene-derivatives like carbon nanotubes and graphene oxides have shown considerably stronger binding affinity with organic pollutants and heavy metals via combination of van der Walls forces, electrostatic attraction, and π-π stacking interactions organic removal.[29]

Nano-adsorbents can be also readily merged into existing treatment processes in slurry reactors or adsorbers. Applied in the powder form, nano-adsorbents in slurry reactors can be highly efficient because all surfaces of the nanoadsorbents are employed and the mixing greatly facilitates the mass transfer. On the other hand, an additional separation process is necessary to recover the nanoparticles. Nano-adsorbents can be utilized as well in fixed or fluidized adsorbers in the form of pellets/beads or porous granules loaded with nano-adsorbents. Fixed-bed reactors are usually associated with mass transfer limitations and head loss; but it does not require future separation process.

Applications of nano-adsorbents for heavey metals removal such as arsenic, copper and nickel have been commercialized, and their performance and cost have been compared to other commercial adsorbents in pilot tests.[30] ArsenXnp is a commercial hybrid ion exchange medium comprising of iron oxide nanoparticles and polymers. ADSORBSIA_ is a nanocrystalline TiO_2 medium in the form of beads from 0.25 to 1.2mm in diameter. Both nano-adsorbents were highly efficient in removing arsenic and ArsenXnp required little backwash.[28]

Renewable Energy and Environmental Remediation. The unique physical and chemical features of nanoparticles can make them alternative solutions to be employed in environmental remediation for enhancing the performance in renewable energy field.[2,6] Environmental remediation using nanoparticles is successfully utilized to treat or decontaminate the air, water and soil these days. Nanoremediation is one of the effective ways because it provides *in situ* treatment eliminating organic pollutants and heavy metals. The general mechanism for waste-water treatment is the redox reactions. The nanoparticles are employed to treat the surface water by disinfection, purification and desalination. Some of the contaminants are most likely to be heavy metals, pathogens and organic contaminants. It has proven to be efficient and eliminating the need for chemicals that may sometime produce secondary reaction products. The major use of nanoparticles are to treat municipal and industrial wastewater as well as the sludge produced. The replacement of nanoparticles for conventional chemicals is due to less cost, higher efficiency

and lower quantity required for treatment. Contaminated soil is cleaned or treated using nanoparticles by injecting the nanoparticles into specific target locations for heavy metal contamination, toxic industrial waste, etc. The higher surface area of certain nanoparticles has been used as a nanocatalyst in gaseous reactions. The most widely used area is in industrial stacks to reduce the contaminant level to prescribed limits or to remove completely that reduces the air pollution. Extensive research is being carried out in the use of nanoparticles for renewable energy. Higher light and UV absorption with a very low reflection coatings in solar cells has improved their efficiency by considerable extent. The hydrophobic property of some nanoparticles has led to self-cleaning solar cells. High thermal conductivity and heat absorption capacity of certain nanoparticles are used to coat boilers and solar concentrators to improve their thermal efficiency.

1.4. References

(1) Y.-W. Jun, J.-H. Lee, J.-S. Choi, J. Cheon, *J. Phys. Chem. B,* **2005,** *109,* 14795.

(2) S. Suresh, *Nanoscience and Nanotechnology*, **2013,** *3,* 62.

(3) C. B. Murray, D. J. Norris, M. G. Bawendi, *J. Am. Chem. Soc.,* **1993,** *115,* 8706.

(4) G. Sun, The Intersubband Approach to Si-based Lasers, Advances in Lasers and Electro Optics, Nelson Costa and Adolfo Cartaxo (Ed.), **2010**, ISBN: 978-953-307-088-9

(5) H. Goesmann, C. Feldmann. *Angew. Chem. Int. Ed.,* **2012**, *49*, 1362.

(6) A. M. Ealias, M. P. Saravanakumar, *IOP Conf. Ser.: Mater. Sci. Eng.,* **2017,** *263,* 032019.

(7) N. E. Moti, A. F. Smith, C. J. DeSantis, S. E. Skrabalak, *Chem. Soc. Rev.,* **2014,** *43,* 3823.

(8) S. K. Ghosh, T. Pal, *Chem. Rev.,* **2007,** *107,* 4797.

(9) G. V. Hartland, *Chem. Rev.,* **2011,** *111,* 3858.

(10) T. Laaksonen, V. Ruiz, P. Liljerothc, B. M. Quinn, *Chem. Soc. Rev.,* **2008,** *37,* 1836.

(11) C.-Z. Ning, L. Dou, P. Yang, *Nat. Rev. Mater.,* **2017,** *2,* 17070.

(12) L. Mino, G. Agostini, E. Borfecchia, D. Gianolio, A. Piovano, E. Gallo, C. Lamberti, *J. Phys. D: Appl. Phys.,* **2013,** *46,* 423001.

(13) Y.-W. Jun, J.-S. Choi, J. Cheon, *Angew. Chem. Int. Ed.,* **2006**, *45*, 3414.

(14) S. Kumar, T. Nann, *Small,* **2006**, *2*, 316.

(15) S.-M. Lee, S.-N. Cho, J. Cheon, *Adv. Mater.,* **2003,** *15,* 441.

(16) A. Rockett, The Materials Science of Semiconductors, Springer US, **2008**, ISBN: 978-0-387-25653-5.

(17) M. Landmann, E. Rauls, W. G. Schmidt, *Phys. Rev. B,* **2017**, *95*, 155310.

(18) Y. Lee, Y. Hwang, Y.-C. Chung, *ACS Appl. Mater. Interfaces*, **2015**, *7,* 7163.

(19) J. Lee, Y. Kim, J. K. Kim, S. Kim, D.-H. Min, D.-J. Jang, *Appl. Catal. B: Environ.*, **2017**, *205*, 433.

(20) J. Lee, D.-J. Jang, *RSC Adv.*, **2015**, *5*, 64268.

(21) H. Cheraghi, M. Shahmiri, Z. Sadeghian, *Thin Solid Film*., **2012**, *522*, 289.

(22) E. Lugscheider, S. Barwulf, C. Barimani, M. Riester, H. Hilgers, *Surf. Coatings Technol*., **1998**, *108*, 398.

(23) S. Mohammadi, A. Harvey, K. V.K. Boodhoo, *Chem. Eng. J*., **2014**, *258*, 171.

(24) V. D. Santo, A. Gallo, M. M. Gatti, V. D. Grandi, R. Psaro, L. Sordellia, S. Recchia, *J. Mater. Chem.*, **2009**, *19*, 9030.

(25) M. K. Choi, J. Yang, T. Hyeon, D.-H. Kim, *npj Flexible Electronics*, **2018**, *2*, 10.

(26) M. Gao, L. Zhu, W. L. Ong, J. Wang, G. W. Ho, *Catal. Sci. Technol*., **2015**, *5*, 4703.

(27) J. Low, J. Yu, M. Jaroniec, S. Wageh, A. A. Al-Ghamdi, *Adv. Mater*. **2017**, *29*, 1601694.

(28) X. Qu, P. J.J. Alvarez, Q. Li, *Water Research*, **2013,** *47*, 3931.

(29) J. Lee, S. Ham, D.-J. Jang, *J. Environ. Chem. Eng.,* **2017,** *5*, 4431-4440.

(30) R. Saeedirad, S. T. Ganjali, M. Bazmi, A. Rashidi, *J. Taiwan Inst. Chem. Eng.*, **2018**, *82*, 10.

Chapter 2. Highly Efficient Photocatalytic Performances of SnO_2-Deposited ZnS Nanorods Based on Interfacial Charge Transfer[†]

[†]This is reproduced from Jaewon Lee, Yeonho Kim, Joon Ki Kim, Seongchan Kim, Dal-Hee Min, and Du-Jeon Jang, *Appl. Catal. B: Environ.* **2017**, *205*, 433.

2.1. Abstract

SnO_2/ZnS nanocomposites of SnO_2 quantum dots (QDs)-deposited ZnS nanorods having highly enhanced photocatalytic activity and photostability have been fabricated via a facile two-step hydrazine-assisted hydrothermal process without involving any surface treatments. The photocatalytic activity of SnO_2/ZnS nanocomposites with a Sn-to-Zn molar ratio ($R_{Sn/Zn}$) of 0.1 is 3 times higher than that of pristine ZnS nanorods and 17 times higher than that of commercial ZnS. The incorporation of SnO_2 QDs increases the photocatalytic efficiency of ZnS nanorods due to the following reasons: photogenerated charge carriers are readily separated owing to type II band configuration and direct contact at interfaces without having any linker molecules; active surface sites are increased to adsorb more dye molecules; the light absorption range is extended to the visible region, generating more charge carriers on the surfaces of heterojunction structures. The decay time, as well as the intensity, of the band-edge emission of SnO_2/ZnS nanocomposites at 325 nm decreases progressively and rapidly with the increase of $R_{Sn/Zn}$, indicating that fast electron transfer takes place from photoexcited ZnS nanorods to SnO_2 QDs. Thus, the higher photocatalytic degradation efficiencies of SnO_2/ZnS nanocomposites are considered to result mainly from the increased separation rates of photogenerated charges. The photostability of SnO_2/ZnS nanocomposites is also improved due to the protection and charge-separation effects of decorating SnO_2 QDs. Our prepared SnO_2/ZnS nanocomposites are

suggested to have great potential for photodegradation nanocatalysts in the field of waste-water treatment.

2.2. Introduction

Environmental pollution and energy shortage have emerged as serious problems with the development of technology and industry. Particularly, toxic and colored organic pollutants generated in textile and dye industry have significant negative effects on the nature of water, decreasing available clean water and destroying the ecosystem. Thus, the development of diverse advanced oxidation processes (AOPs) has been progressed by oxidation with radical species for environmental decontamination.[1] Among these AOPs, photocatalytic techniques based on semiconductors as green and efficient ways have great potential in conquering current energy and environmental issues using the inexhaustible solar energy.[2-5] In addition, the techniques do not produce toxic by-products during photocatalytic processes.

It has been reported that metal sulfide nanostructures as photocatalysts can degrade various organic pollutants efficiently under light irradiation owing to their suitable catalytic function and band gap.[6-10] In particular, ZnS nanomaterials having a wide and direct band gap (3.80 eV for hexagonal wurtzite) are promising photocatalysts because of not only the rapid generation of electron-hole pairs by photo-excitation but also the highly negative reduction potential of their conduction band.[11-14] However, there are some serious drawbacks hindering their photocatalytic activity and practical applications, such as the rapid recombination of charge carriers and the absorption of limited UV light. Even the low separation efficiency of electron-hole pairs often causes

photocorrosion problems, making ZnS very unstable and poorly recyclable as a photocatalyst.[15-21] Thus, in order to overcome these disadvantages, diverse strategies have been established such as the fabrication of porous and hollow structures, doping with nonmetals, and coupling with other noble metals and/or semiconductors.[11-21] One of the most extensively employed approaches is to combine a semiconductor with another semiconductor having different electron affinity and ionization potential.[20-25] In other words, the combination of two semiconductors having different redox potential levels provides a significant key role to attain charge separation effectively at interfacials, to extend the photoresponse range largely, and to prolong the lifetime of charge carriers considerably.[23-31]

Heterojunction nanocomposites, where one semiconductor is partially coated by the other semiconductor, have received extraordinary attention as photocatalysis systems because both electrons and holes can readily participate in the redox reaction on their surfaces.[25-31] Furthermore, one-dimensional (1D) nanostructures as photocatalyst substrates have been extensively used due to their unique structural and electronic properties and superior performances in the heterojunction systems.[23,27-29] 1D nanostructures such as nanorods and nanowires/nanobelts possess several advantages as follows: large aspect ratios which can increase the capacity of light absorption; great separation efficiencies of photo-generated charge carriers due to their high mobility and straight transport pathways.[31-34]

Tin oxide (SnO_2) having an n-type wide band gap (3.60 eV for tetragonal rutile) has been also well-known as a popular photocatalyst because of its high photocatalytic activity and stability, non toxicity, low cost, and ubiquitous availability.[27,28,35-40] Especially, its combination with ZnS nanomaterials can form excellent heterojunction photocatalysts having type II band offsets.[36,37] However, the conduction band (CB) of SnO_2 is more positive than the reduction potential of $O_2/\cdot O_2H$ (-0.05 eV vs NHE at pH 0).[30,31] Thus, although the deposition of SnO_2 nanoparticles on ZnS nanomaterials provides an enhanced charge-separation efficiency, it cannot produce strong oxidizing species such as $\cdot O_2H$ to decompose water contaminants.[30,31,40] In contrast, the band gap of SnO_2 quantum dots (QDs) gets expanded gradually owing to the quantum confinement effect, as their sizes decrease. With the increase of the band gap, the CB of SnO_2 QDS shifts to the more negative potential, reducing O_2 to generate peroxy radicals ($\cdot O_2H$).[30,41-43]

In this work, we have fabricated SnO_2/ZnS nanocomposites of SnO_2 QDs-deposited ZnS nanorods as 1D heterojunction nanostructures through a facile two-step hydrazine-assisted hydrothermal process without using any complex surface treatments to introduce new functional molecules or additional inter-connectivity.[42-44] It is noteworthy that a rational synthesis of high-quality SnO_2/ZnS heterojunction nanocomposites via a simple and friendly manner has not been reported yet.[36,37] The photocatalytic activity and photostability of SnO_2/ZnS heterojunction nanostructures are much higher than the respective ones of ZnS nanorods. The decay time, as well as the intensity, of the band-

edge emission of SnO_2/ZnS nanocomposites decreases progressively and rapidly with the increase of the SnO_2 content, indicating that the higher photocatalytic degradation efficiencies of SnO_2/ZnS nanocomposites result mainly from the increased separation rates of photogenerated charges. Our prepared SnO_2/ZnS nanocomposites are considered to have great potential for photodegradation nanocatalysts in the field of waste-water treatment.

2.3. Experimental Details

Synthesis. SnO_2/ZnS heterojunction nanostructures of SnO_2-deposited ZnS nanorods having a specific molar ratio of Sn/Zn were prepared using a simple two-step hydrazine-assisted hydrothermal method. In typical preparation of single-crystalline wurtzite ZnS nanorods,[44] 7.5 mL of water, 7.5 mL of ethylenediamine, 15 mL of $N_2H_4 \cdot H_2O$, 2.0 mmol of $ZnCl_2$, and 2.0 mmol of sulfur were stirred vigorously for 30 min. The mixture solution was then loaded into a Teflon-lined stainless-steel autoclave with a capacity of 50 mL. The sealed autoclave was put into an oven at 180 °C for 9 h and cooled to room temperature (first step). 0.08, 0.16, 0.20, 0.24, or 0.30 mmol of $SnCl_4 \cdot 5H_2O$(s) was added into the 30 mL of the mixture solution containing 195 mg ZnS nanorods and stirred for 10 min vigorously. Then, the mixture solution was poured into the autoclave. Note that $R_{Sn/Zn}$, the molar ratio of Sn to Zn in the final mixture, was varied from 0.00 to 0.15. The sealed autoclave was put again

into an oven preheated at 180 °C for another 6 h (second step). The resultant products were repeatedly centrifuged, washed with water several times, and finally dried in a vacuum at 60 °C for 5 h to obtain SnO_2/ZnS heterojunction nanostructures.

Characterization. Transmission electron microscopy (TEM) images were obtained with a Hitachi H-7600 microscope while scanning electron microscopy (SEM) images were recorded with a MERLIN Compact microscope. While high-resolution X-ray diffraction (HRXRD) patterns were taken with a Bruker D8 DISCOVER diffractometer using Cu K_α radiation (0.15418 nm), high-angle annular dark-field (HADDF) images and energy-dispersive X-ray (EDX) elemental mappings were measured utilizing a JEOL JEM-2100F scannig TEM (STEM) microscope. High-resolution TEM (HRTEM) images and selected area electron diffraction (SAED) patterns were recorded with a Tecnai F20 microscope. X-ray photoelectron spectroscopy (XPS) spectra were obtained by employing a KRATOS AXIS-HSi spectrometer having a 150 W Mg anode with a scan step of 0.1 eV, and observed binding energies were calibrated with the C 1s peak at 284.5 eV of contaminated carbon. UV-vis diffuse reflectance spectra were recorded using a StellaNet US/EPP 2000C spectrometer, and N_2 adsorption–desorption measurements were carried out using a Nova 2200e Quantachrome instrument. PL spectra were taken using an Ocean Optics USB2000+ detector with excitation of 266 nm pulses having a duration time of 6 ns from a Q-switched Quantel Brilliant Nd:YAG laser. To obtain PL decay kinetic profiles, 266 nm pulses from a mode-locked Quantel

Pizzicato Nd:YAG laser of 25 ps were utilized for excitation, and a Hamamatsu C2830 streak camera of 10 ps attached with a Princeton Instruments RTE128H CCD detector was employed for detection. PL wavelengths were selected by combining cut-off and band-pass filters. To detect the generation of $\cdot O_2^-$ radical species, electron spin resonance (ESR) measurements were carried out using a Bruker EMX-plus X-band CW electron paramagnetic resonance spectrometer with spin-trap reagent 5,5-dimethyl-1-pyrroline *N*-oxide (DMPO, s, purchased from Sigma-Aldrich). Total organic carbon (TOC) was estimated using a Sievers 5310C TOC analyzer.

Photocatalytic Experiments. The photocatalytic performances of as-prepared SnO_2/ZnS nanocomposites as nanocatalysts were evaluated by monitoring the photodegradation reaction of RhB under ambient conditions. In a typical procedure, 30 mL of an aqueous suspension containing 5.0 mg nanocatalysts and 10 μM RhB was stirred for 1 h in the dark to assure the establishment of an adsorption-desorption equilibrium of RhB on the surfaces of nanocatalysts. The entire mixture solution was covered by the light beam of a 300 W Schoeffel LPS 255 HR xenon lamp. The mixture was stirred magnetically during irraditation, and an aliquot was taken at every 10 min and centrifuged (10000 rpm, 10 min) to separate the supernatant. The concentration of remnant RhB in the aliquots was monitored by measuring UV/vis absorption spectra with a Scinco S-3100 spectrometer. The photocatalytic activity was also investigated by measuring the photodegradation of phenol; the experimental procedure was the same except that 5 mg nanocatalysts and 10 μM RhB were

replaced by 20 mg nanocatalysts and 0.43 mM phenol (s, 99+%, purchased from Alfa Aesar). Hydroxyl radicals formed on the surface of SnO_2/ZnS nanocomposites was detected by the PL technique using TA as the probing molecule.[11,29] Typically, 0.5 mg of a photocatalyst was added into 30 mL of a mixture solution containing 0.5 mM TA and 2 mM NaOH in a quartz reactor. The experimental procedure was similar to that for the measurement of photocatalytic efficiencies except that the RhB mixture solution was replaced by TA and NaOH. The PL spectra of 2-hydroxyterephthalic acid (TAOH) produced via a reaction with ·OH were measured using a JASCO FP-8300 fluorescence spectrometer with excitation at 315 nm. In order to examine the reusability of the nanocatalysts, all the experimental parameters were kept constant. After each reaction, the color of an aqueous solution containing a nanocatalyst and RhB became colorless. Then, a fresh RhB solution has added into the resultant solution, where the initial concentration of RhB was always 10 μM. The experiments were repeated for 4 times under the same conditions.

2.4. Results and Discussion

In order to examine the morphology and the structure of ZnS nanorods and SnO_2/ZnS nanocomposites, SEM and TEM images have been measured (Figure 2-1). As-obtained ZnS nanorods have 1D morphology with a typical length of 1.8 μm and an average width of 90 nm while SnO_2 QDs having an average

diameter of 3.0 nm are well dispersed on the surface of ZnS nanorods. Compared with the common base of NH_3 or NaOH, our employed base of hydrazine plays an important role in forming hybrid complexes.[43] Briefly, since the tin precursor of $SnCl_4 \cdot 5H_2O$ was added into the reaction mixture containing hydrazine, SnO_2 QDs of 3.0 nm have been produced via forming $(SnCl_4)_m(N_2H_4)_n$ complexes.[42,43] The deposition of SnO_2 QDs on ZnS nanorods has been attributed to the decreasing force of the surface free energy between ZnS nanorods and SnO_2 QDs due to the high surface energy of SnO_2 QDs resulting from their small sizes.[30,31,34] Furthermore, the hydrothermal process also plays a key role in the deposition of SnO_2 QDs onto the surface of ZnS nanorods because collision and contact between ZnS nanorods and SnO_2 QDs, promoted by high temperature and pressure, are favorable to the binding of ZnS nanorods with SnO_2 QDs.[19,25-28,34,42] Because of direct and enhanced electron transfer resulting from close contact between ZnS and SnO_2 without having linker molecules, SnO_2/ZnS heterojunction nanocomposites have highly enhanced catalytic performances compared to pristine ZnS nanorods (see below).[19] Figure 2-2 also presents the TEM images of SnO_2/ZnS heterojunction nanocomposites having different $R_{Sn/Zn}$ values. As the value of $R_{Sn/Zn}$ was increased from 0.04 up to 0.15, the surface of ZnS nanorods has been found to be more densely covered with SnO_2 QDs, suggesting the loading and the size of SnO_2 QDs can be controlled by tuning the concentration of the tin precursor.

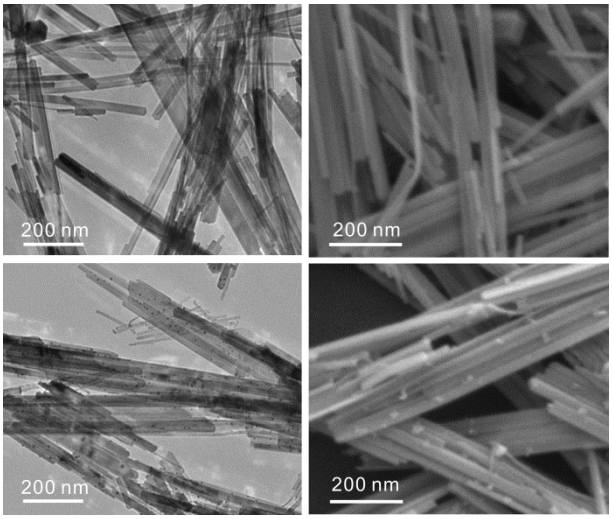

Figure 2-1. TEM (left) and SEM (right) images of ZnS nanorods (top) and SnO_2/ZnS ($R_{Sn/Zn}$ = 0.10) nanocomposites (bottom).

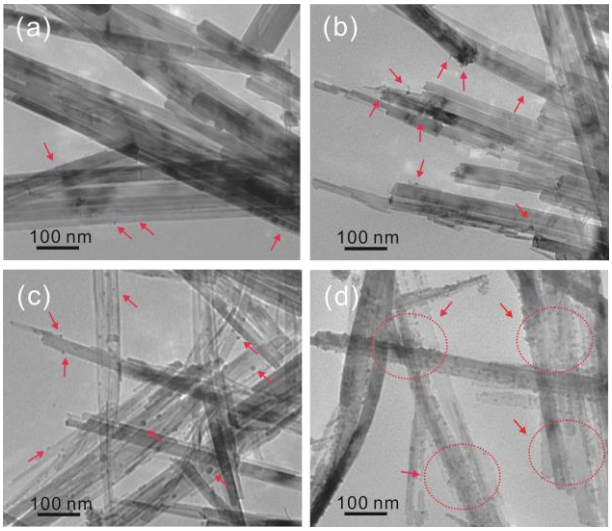

Figure 2-2. TEM images of SnO_2/ZnS nanocomposites having $R_{Sn/Zn}$ values of 0.04 (a), 0.08 (b), 0.12 (c), and 0.15 (d); the arrows indicate SnO_2 quantum dots.

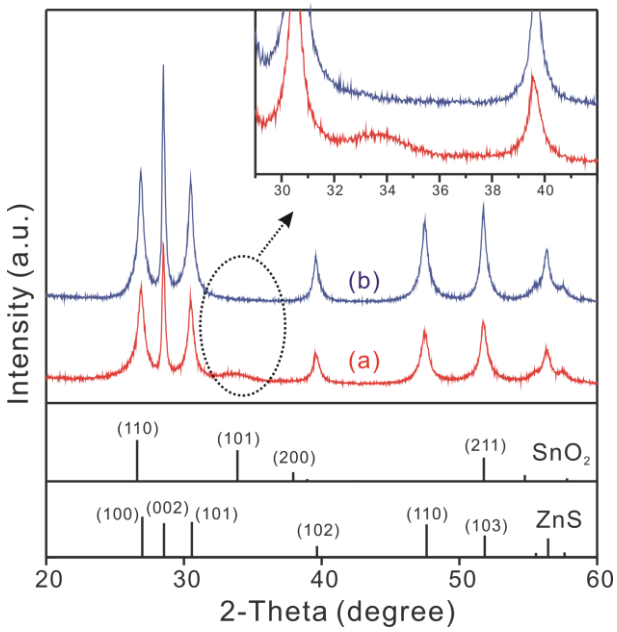

Figure 2-3. HRXRD patterns of SnO_2/ZnS ($R_{Sn/Zn}$ = 0.10) nanocomposites (a) and pristine ZnS nanorods (b). The standard diffraction lines of rutile SnO_2 and wurtzite ZnS are also shown for comparison.

The crystal structure, phase purity, and average crystallite size of as-prepared samples have been investigated by monitoring HRXRD (Figure 2-3). All the HRXRD patterns of SnO_2/ZnS samples exhibit standard diffraction peaks corresponding to hexagonal ZnS (JCPDS card no. 36-1450) or rutile SnO_2 (JCPDS card no. 41-1445); neither impurity peaks nor remarkable shifts from the diffraction peaks of pristine ZnS nanorods have been detected, suggesting that ZnS and SnO_2 exist together while no solid solution has been formed and the expansion or shrinkage of the ZnS lattice has not been observed in the nanocomposites.[27,45,46] Furthermore, the inset in Figure 2-3 presents that the weak and broad diffraction peak of rutile SnO_2 QDs at 33° describes small grain sizes in the nanocomposites, and that SnO_2 QDs have been loaded well on the

surface of ZnS nanorods.[28-31] The average crystallite sizes of ZnS and SnO_2 in the nanocomposites have been estimated from the peak widths of the (001) planes of hexagonal ZnS and the (101) planes of rutile SnO_2, respectively, using the Scherrer equation.[42,44] When the molar ratio of Sn/Zn has increased from 0.08 to 0.15 gradually, the diffraction intensity of the rutile SnO_2 (101) planes at 33°, as well as the average crystallite size of SnO_2 QDs, has steadily enlarged while the intensities of the ZnS diffraction peaks have reduced due to the hinderance of SnO_2 QDs on the X-ray transmission.[30,31] The chemical composition of all the samples has been analyzed by the EDX technique, revealing that Zn, S, Sn, and O elements exsit together. In particular, the calculated actual molar ratios of Sn to Zn are consistent approximately with the respective $R_{Sn/Zn}$ values of SnO_2/ZnS nanocomposites, suggesting that the tin precursor added in the reaction mixture containing ZnS nanorods has been transformed almost entirely into SnO_2 QDs decorated on ZnS nanorods.[25,31]

The HRTEM images of Figure 2-4a and b reveal that the observed lattice spacings of SnO_2/ZnS ($R_{Sn/Zn}$ = 0.10) heterojunction nanostructures are 0.315 and 0.335 nm which arise from the (001) planes of hexagonal ZnS and the (110) planes of rutile SnO_2, respectively. Meanwhile, the other observed lattice spacings of 0.265 and 0.176 nm in Fig. 3b are attributed to the (101) and (211) planes of rutile SnO_2, respectively. Thus, the HRTEM images of Figure 2-4a and b designate that SnO_2 QDs have been deposited onto the surfaces of ZnS nanorods via interfacial junction without having any linker molecules. The SAED pattern of the SnO_2/ZnS ($R_{Sn/Zn}$ = 0.10) nanocomposites supports that

heterojunction nanostructures have been well fabricated via a two-step hydrazine-assisted hydrothermal process (Figure 2-4c).[25] To understand the constitution and chemical compositon of the heterojunction structures further, elemental analysis has been performed with the HAADF-STEM mode of EDX; SnO_2 QDs look brighter than the ZnS nanorod in the HAADF-STEM image of Figure 2-4d because the atomic number of Sn (50) is larger than that of Zn (30). The EDX elemental mapping images of Figure 2-4e-g also suggest that SnO_2 QDs are well distributed homogeneously on the surface of a ZnS nanorod.

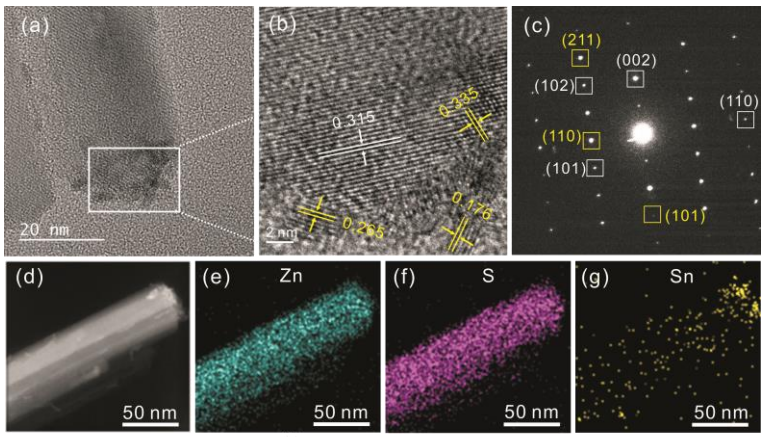

Figure 2-4. HRTEM images (a and b) and SAED pattern (c), HAADF-STEM image (d), and EDX elemental mapping images (e–g) of a SnO_2/ZnS ($R_{Sn/Zn}$ = 0.10) nanocomposite.

Figure 2-5 shows that XPS has been employed to investigate the surface chemical states of obtained SnO_2/ZnS ($R_{Sn/Zn}$ = 0.10) nanocomposites. The binding energies (BEs) of Zn $2p_{3/2}$ and Zn $2p_{1/2}$ were observed as 1044.23 and 1021.03 eV, respectively, while the BEs of S $2p_{3/2}$ and S $2p_{1/2}$ were measured as 160.83 and 162.03 eV, respectively.[12,19,44] Compared with the Zn and S XPS

spectra of pristine ZnS nanorods, the respective spectra of nanocomposites have been hardly changed in spite of the incorporation of SnO_2 QDs, demonstrating that the structure of ZnS nanorods in SnO_2/ZnS nanocomposites are almost the same as that in pristine ZnS nanorods.[27] Two sharp peaks at 486.15 and 494.48 eV in Figure 2-5c have been assigned to Sn $3d_{5/2}$ and Sn $3d_{3/2}$, respectively.[31] The spin-orbit separation of 8.3 eV between two peaks confirms that the oxidation state of Sn atoms adsorbed on the surface of the nanocomposites is +4.[31,38] The O 1s XPS spectrum has been deconvoluted into three peaks; the O_L peak at 530.19 eV is associated with the lattice oxygen of SnO_2 QDs, the O_O peak at 531.58 eV is attributed to chemisorbed oxygen, and the O_C peak at 532.92 eV is ascribed to chemically adsorbed hydroxyl groups.[27,31,40,50]

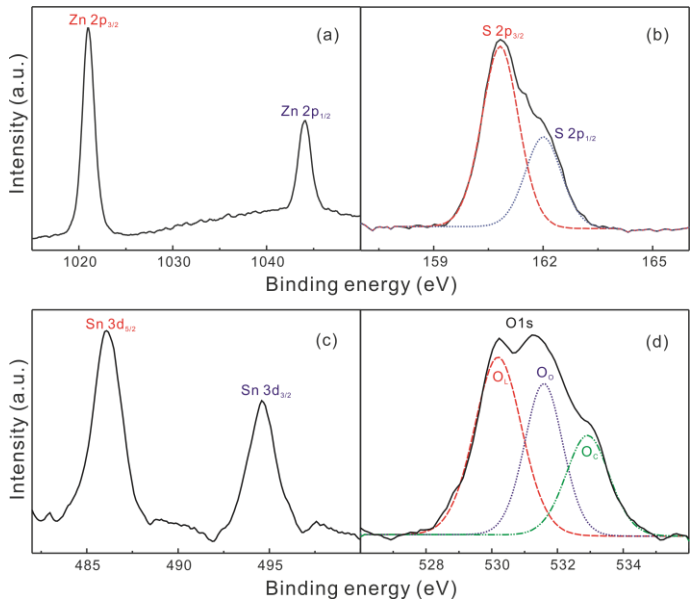

Figure 2-5. Zn 2p (a), S 2p (b), Sn 3d (c), and O 1s (d) XPS spectra of SnO_2/ZnS ($R_{Sn/Zn}$ = 0.10) nanocomposites. The O 1s spectrum has been deconvoluted into three Gaussian curves.

The UV-vis diffuse-reflectance spectra of SnO_2/ZnS nanocomposites having specifically varied Sn/Zn molar ratios have been investigated (Figure 2-6). Pristine ZnS nanorods have limited UV photoresponse below 340 nm (3.7 eV) while SnO_2/ZnS nanocomposites have extended visible absorption up to 500 nm due to the newly generated interface energy states between ZnS and SnO_2 in the heterojunction structures.[23-25,51] Indeed, a new absorption band appears at 350-500 nm for SnO_2/ZnS nanocomposites, and it has been atrributed to the new interfacial states whose energy levels are localized whithin the band gap of ZnS, reducing the band gap energy of the nanocomposites compared with that of pristine ZnS nanorods.[23,51] Figure 2-6 also indicates that light absorption in the visible range increases with the increment of SnO_2 contents in the heterojunction nanostructures. Thus, we can conclude that extended photoresponse up to 500 nm is also an important factor to enhance the photocatalytic performances of SnO_2/ZnS nanocomposites.

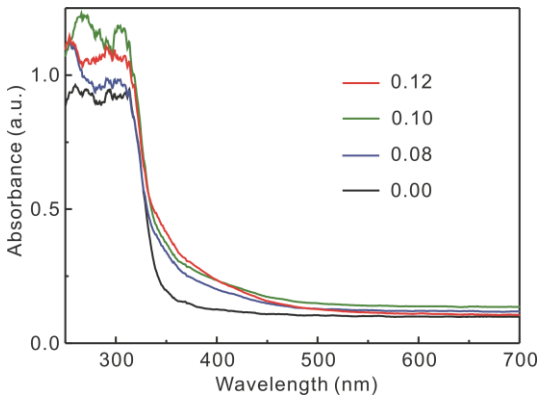

Figure 2-6. UV-vis diffuse-reflectance spectra of SnO_2/ZnS nanocomposites with indicated $R_{sn/zn}$ values.

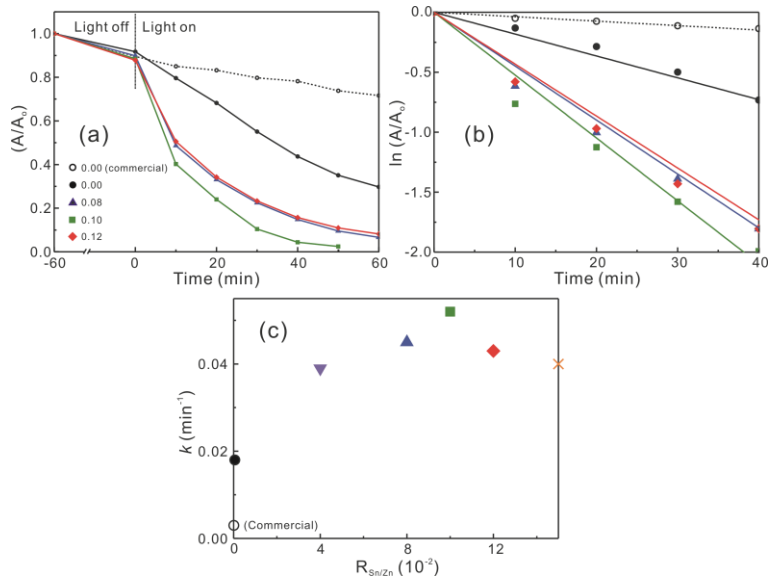

Figure 2-7. Decay kinetic profiles at 554 nm (a)**,** first-order decay profiles (b) and degradation rate constants (c) of RhB via SnO_2/ZnS nanocomposites with indicated $R_{Sn/Zn}$ values.

Table 2-1. Catalytic degradation rate constants, BET surfaces areas, and average pore sizes of nanocatalysts.

Nanocatalyst	$R_{Sn/Zn}$	k (min^{-1})	BET surface area (m^2/g)	Average pore size (nm)
No catalysts	–	0.001		
Commercial SnO_2	∞	0.020		
Commercial ZnS	0.00	0.003		
ZnS nanorods	0.00	0.018	76.0	63.7
Nanocomposites	0.04	0.039	83.3	32.5
Nanocomposites	0.08	0.045	95.2	29.9
Nanocomposites	0.10	0.052	97.1	29.7
Nanocomposites	0.12	0.043	98.8	30.9
Nanocomposites	0.15	0.040	99.8	30.9

The photocatalytic properties of SnO_2/ZnS nanocomposites having specifically varied molar ratios of Sn/Zn have been evaluated by observing the time-dependent absorbance changes of RhB under light irradiation. The characteristic absorption of RhB at 554 nm diminishes gradually with the increase of the light irradiation time.[52] Additionally, a concomitant blue shift in the absorption maximum has been observed together, implying that the photodegradation of RhB goes through two competitive processes; one is the destruction of the conjugated chromophore structure, which bring about absorption loss at 554 nm,[53] and the other is the stepwise N-deethylation reaction that removes the N-ethyl groups sequentially from the RhB molecules.[6,52] The photocatalytic efficiency of SnO_2/ZnS ($R_{Sn/Zn}$ = 0.10) nanocomposites has been found to be significantly higher than that of any other studied nanocatalytsts; the efficiency of SnO_2/ZnS ($R_{Sn/Zn}$ = 0.10) nanocomposites is 3 times higher than that of pristine ZnS nanorods and 17 times higher than that of commercial ZnS. The pseudo-first order photodegradation kinetic profiles of RhB have been exploited (Figure 2-7a) to obtain the kinetic constants of Table 2-1 using $\ln (A/A_0) = -kt$, where k is the rate constant and t is the time.[53] In addition, the photodegradation kinetic data of phenol also demonstrate that the photocatalytic activity of SnO_2/ZnS having $R_{Sn/Zn}$ = 0.10 (k = 0.0074 min^{-1}) is much higher than that of pristine ZnS (k = 0.0028 min^{-1}). Figure 2-7 indicates that the photocatalytic performances of SnO_2/ZnS hybrid nanostructures are enhanced gradually with the increase of $R_{Sn/Zn}$ until the value becomes 0.1. However, as $R_{Sn/Zn}$ increases over 0.1, the

photocatalytic efficiency of SnO_2/ZnS nanocomposites rather decreases. Thus, excess SnO_2 QDs on the surface of ZnS nanorods are considered to act as the recombination sites, rather than the separation sites, of photogenerated charges;[19,25-27] excessive SnO_2 shells not only block the transmission of light into ZnS nanorods but also diminish the accessibility of RhB molecules to the active sites of ZnS nanorods surfaces, hardly increasing the generation of charge carriers from ZnS nanorods.[26,27,30,31,49]

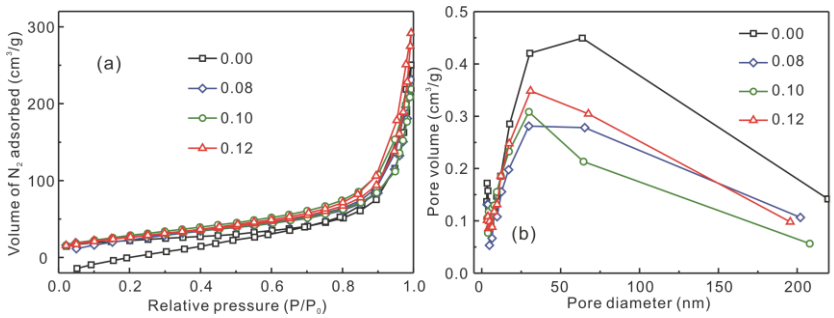

Figure 2-8. N_2 adsorption-desorption isotherms (a) and pore-size distributions (b) of SnO_2/ZnS nanocomposites with indicated $R_{Sn/Zn}$ values.

N_2 adsorption-desorption isotherms of as-prepared SnO_2/ZnS nanocomposites with different molar ratios of Sn/Zn have been evaluated to characterize the surface area and the porosity of each nanocatalyst (Figure 2-8). We have found out that our samples exhibit type-IV isotherms including typical type-H3 hysteresis loops (at $P/P_0 > 0.8$) according to the IUPAC classification, implying the formation of large mesopores and macropores.[18,21,26,31] The Brunaure-Emmett-Teller (BET) surface areas and pore sizes of SnO_2/ZnS nanocomposites with diverse $R_{Sn/Zn}$ values have been summarized in Table 2-1. The surface area of the nanocomposites gradually increases with the increase

of the SnO_2 content until the molar ratio of Sn/Zn becomes 0.1, and the enhanced surface area is suggested to offer the higher adsorption ability of the catalyst surface toward organic molecules and the higher generation ability of charge carriers from active sites.[54] Thus, these results support as well that heterojunction nanocomposites have higher photocatalytic ability than single-component photocatalysts do partly due to the increased surface area. Overall, we consider that the increased surface area is not the only factor responsible for determining the photocatalytic activity.

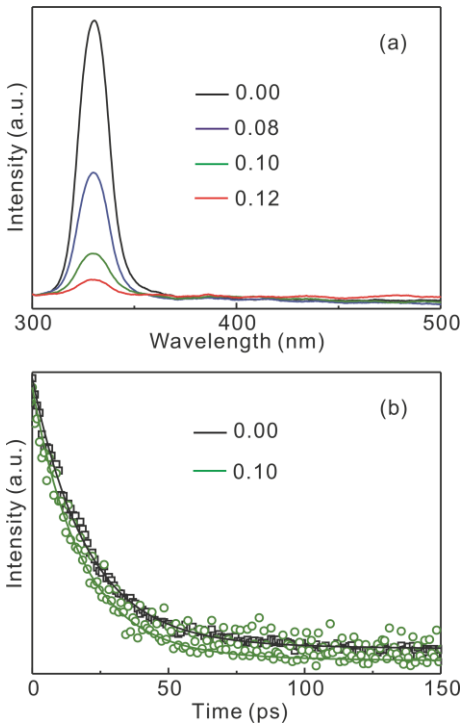

Figure 2-9. PL spectra (a) and emission decay profiles at 325±20 nm (b) of SnO_2/ZnS nanocomposites with indicated $R_{Sn/Zn}$ values. Samples were suspended in ethanol and excited with 266 nm laser pulses.

Table 2-2. PL intensities and emission decay kinetic constants of SnO_2/ZnS nanocomposites with indicated $R_{Sn/Zn}$ values suspended in ethanol.

$R_{Sn/Zn}$	I_0[a]	Decay time (ps)	τ_0[b] (ps)	k_{ET} (10^9 s^{-1})
0.00	1.00	20 (94%) + 700 (6%) [c]	60.8	–
0.08	0.45	19 (95%) + 600 (5%)	48.1	4.3
0.10	0.15	18 (97%) + 100 (3%)	20.4	33
0.12	0.05	17 (98%) + 70 (2%)	18.1	39

[a] Relative PL intensity. [b] Mean decay time. [c] Initial amplitude percentage of each component.

PL spectra have often been exploited to examine the separation, transfer, and recombination of photogenerated charge carriers.[9,10,55-58] To investigate the charge separation effect of SnO_2 QDs-deposited ZnS nanostructures, we have observed the PL spectra of SnO_2/ZnS nanocomposites having various values of $R_{Sn/Zn}$ (Figure 2-9). An intense PL peak at 325 nm arising from band-edge emission (BEE) has been discovered in pristine ZnS nanorods while defect-related emission in the visible region has not been monitored at all, demonstrating that the structure of ZnS nanorods is perfectly crystalline.[44] With the incorporation of SnO_2 QDs, the BEE of ZnS nanorods decreases drastically while no other PL peaks appear newly; the PL of SnO_2/ZnS nanocomposites decreases rapidly with the increase of $R_{Sn/Zn}$.[57,58] The quenching phenomenon is mainly associated with the efficient charge-separation effect of the type II band configuration consisting of ZnS nanorods and SnO_2 QDs.[9,10,55] This result is also consistent with the enhanced photocatalytic activity of heterojunction nanocomposites in comparison with that of pristine ZnS nanorods. To probe electron transfer dynamics across the interface further, we have also measured the time-resolved PL decay times of SnO_2/ZnS nanocomposites having

controlled $R_{Sn/Zn}$ values.[9,10,56-58] To the best of our knowledge, the decay kinetic study of BEE at 325 nm for ZnS nanoparticles has not been reported yet. Figure 2-9b indicates that the BEE of SnO_2/ZnS ($R_{Sn/Zn}$ = 0.10) nanocomposites decays much faster than that of pristine ZnS nanorods. Furthermore, the PL of SnO_2/ZnS nanocomposites decays rapidly and progressively with the increase of the $R_{Sn/Zn}$ value, suggesting that the decay time of SnO_2/ZnS nanocomposites is reduced because of electron transfer from photoexcited ZnS nanorods to SnO_2 QDs.[56-58] Each decay kinetic profile has been fitted biexponentially (Table 2-2); the fast decay component has been ascribed to the intrinsic recombination of electrons and holes in exciton states while the slow decay component has been considered to arise from the radiative decay of charge carriers in surface states.[8] Whereas the fast component remains almost invariant, the slow component decreases sharply with the increase of the $R_{Sn/Zn}$ value. Thus, this suggests that the drastic PL decrease of SnO_2/ZnS nanocomposites in Figure 2-9 with the increase of $R_{Sn/Zn}$ is due to enhanced electron transfer from the surface states of ZnS nanorods to SnO_2 QDs. The mean PL decay time (τ_0) of the nanocomposites also diminishes rapidly with the increase of $R_{Sn/Zn}$ (Table 2-2). The apparent rate constant of electron transfer (k_{ET}) from ZnS nanorods to SnO_2 QDs (Table 2-2) has been calculated as[9,10,56-58]

$$k_{ET} = [\tau_0(SnO_2/ZnS)]^{-1} - [\tau_0(ZnS)]^{-1} \quad (1)$$

Considering all the above results, we can deduce that the higher photocatalytic degradation efficiencies of SnO_2/ZnS nanocomposites result mainly from the

enhanced separation rates of photogenerated charges in SnO_2/ZnS heterojunction nanostructures, which can be tuned by adjusting $R_{Sn/Zn}$ values.

The above presented results have shown that as-prepared SnO_2/ZnS heterojunction nanocomposites have excellent photocatalytic performances in the degradation of RhB. To elucidate the photodegradation mechanism of RhB clearly, we have investigated the main reactive species of h^+, $\cdot O_2^-$, and ·OH involved in the photocatalytic reaction.[31,34] Here, EDTA, BQ, and IPA were introduced to act as the scavengers of h^+, $\cdot O_2^-$, and ·OH, respectively, in the photocatalytic process.[59,60] Figure 2-10 displays the photocatalytic efficiencies of pristine ZnS nanorods and SnO_2/ZnS ($R_{Sn/Zn}$ = 0.10) nanocomposites for the decomposition of RhB in the presence of different scavengers. While the addition of 30 μmol BQ ($\cdot O_2^-$ scavenger) or 1.0 mL IPA (·OH scavenger) into a reaction mixture solution drastically reduces the photodegradation efficiency of RhB, the addition of 30 μmol EDTA (h^+ scavenger) into a reaction mixture solution has little effect on the photocatalytic activity. These results demonstrate that $\cdot O_2^-$ and ·OH are main reactive species to decompose RhB, whereas h^+ does not play an important role in the photodegradation reaction of RhB. To further examine the generation of ·OH radicals involved in that reaction, ·OH radicals have been detected by measuring PL spectra of TA as a probe molecule, which reacts with ·OH to produce a fluorescent product, 2-hydroxyterephthalic acid (TAOH).[11,29] The PL intensity of TAOH has tendency to increase proportionally with the amount of ·OH generated on the surfaces of

photocatalysts.[59,60] The ESR technique has also been used to detect the $\cdot O_2^-$ radical species evolved during the photocatalytic reaction process.

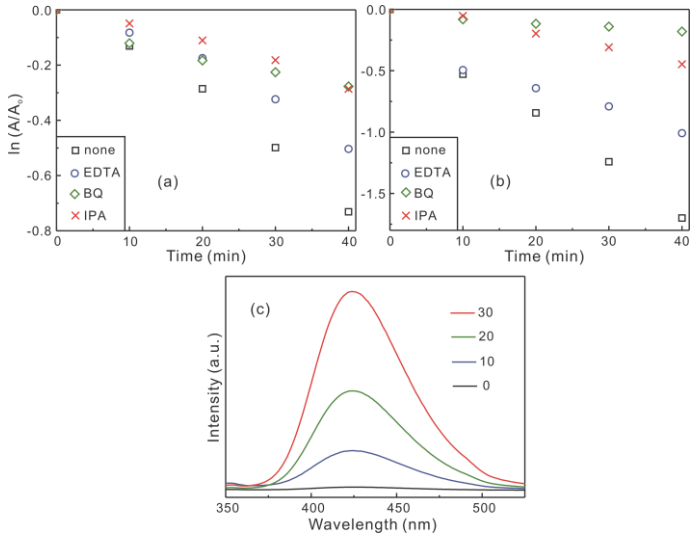

Figure 2-10. First-order decay profiles of RhB via pristine ZnS (a) and SnO_2/ZnS ($R_{Sn/Zn}$ = 0.10) nanocomposites (b) in the presence of indicated scavengers. PL spectra of TAOH generated by light irradiation in the presence of SnO_2/ZnS ($R_{Sn/Zn}$ = 0.10) nanocomposites for durations indicated in the units of min (c).

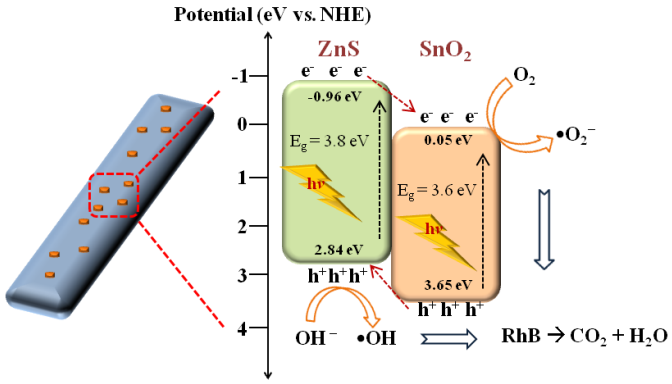

Figure 2-11. Schematic for the degradation mechanism of RhB over a SnO_2/ZnS heterojunction nanostructure under light irradiation.

Based on the above results, the photodegradation mechanism of RhB over SnO_2/ZnS nanocomposites has been schematically illustrated in Figure 2-11. Under light irradiation, charge carriers are generated on both ZnS nanorods and SnO_2 QDs, and charge transfers take place between two nanomaterials; photo-excited electrons on the CB of ZnS nanorods transfer to the CB of SnO_2 QDs while photo-generated holes in the valence band (VB) of SnO_2 migrate into the VB of ZnS through interfacial surfaces until their Fermi levels align.[40,55-58] As a consequence, the recombination of electrons and holes in the nanocomposites is suppressed, giving more chances for electrons and holes to take part in redox reactions on the surfaces. Electrons are trapped by adsorbed O_2 to prduce superoxide radicals ($\cdot O_2^-$), which is a strong oxidant capable of decomposing RhB effectively.[27-31,59,60] Meanwhile, simultaneously generated holes in ZnS can oxidize RhB molecules directly, which are bound to the surfaces of SnO_2/ZnS nanocomposites.[59,60] Moreover, if the adsorption of organic pollutants is insignificant, holes might also react with OH^- adsorbed on the surfaces of the photocatalysts to produce hydroxyl radicals ($\cdot OH$), which concurrently assist the decomposition of organic pollutants.[11,12,47,60] Hence, due to the synergistic effects of superoxide anion radicals, hydroxyl radicals and holes, SnO_2/ZnS heterojunction nanocomposites are suggested to have significantly enhanced catalytic performances for RhB photodegradation. Consequently, taking all the above facts into consideration, we assert that the extension of the photoresponse range to the visible region, the increment of the surface area, and the synergistic charge-separation effect of heterojunctions

between ZnS and SnO_2 without having any linker molecules are responsible together for the highly enhanced photocatalytic activity of SnO_2/ZnS ($R_{Sn/Zn}$ = 0.10) nanocomposites.

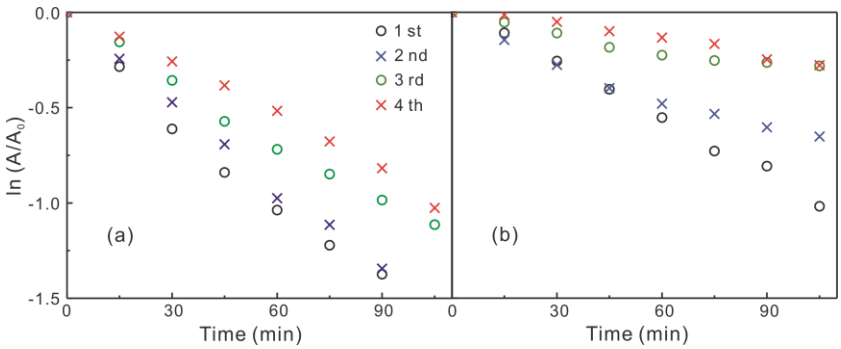

Figure 2-12. Stability test of SnO_2/ZnS ($R_{Sn/Zn}$ = 0.10) nanocomposites (a) and pristine ZnS nanorods (b) via repeated photocatalytic RhB-degradation experiments.

Although photostability during photocatalytic reactions is an important factor, it is well-known that metal sulfides have tendency to be unstable because of photocorrosion problems.[6,11-19] Thus, in order to check the stability of pristine ZnS nanorods and SnO_2/ZnS ($R_{Sn/Zn}$ = 0.10) nanocomposites, recycling tests have been carried out (Figure 2-12). From the second recycling test experiment, recycled SnO_2/ZnS ($R_{Sn/Zn}$ = 0.10) nanocomposites revealed more enhanced stability, as well as higher catalytic activity, than recycled pristine ZnS nanorods, suggesting that decorated SnO_2 QDs enhance not only the photocatalytic activity but also the stability of ZnS nanorod.[26,31,56-58] We consider that the photostability of ZnS nanorods has been enhanced substantially because decorating SnO_2 QDs facilitate the separation of photogenerated charges

extensively and they act as partial shells to inhibit photocorrosion taking place from the surface of ZnS.

2.5. Conclusion

SnO_2 QDs with a typical diameter of 3.0 nm have been deposited on the surfaces of ZnS nanorods having an average length of 1.8 μm and an average width of 90 nm via a facile two-step hydrazine-assisted hydrothermal method without involving any surface treatments to enhance photocatalytic activity and photostability. The photocatalytic activity of SnO_2/ZnS ($R_{Sn/Zn}$ = 0.10) nanocomposites is 3 times higher than that of pristine ZnS nanorods and 17 times higher than that of commercial ZnS. The incorporation of SnO_2 QDs increases the photocatalytic efficiency of ZnS nanorods based on the following reasons: photogenerated charge carriers are readily separated owing to type II band configuration and direct contact at interfaces without having any linker molecules; active surface sites are increased to adsorb more dye molecules; the light absorption range is extended to the visible region, generating more charge carriers on the surfaces of heterojunction structures. With the increase of $R_{Sn/Zn}$, the picosecond decay time, as well as the PL intensity, of the BEE of SnO_2/ZnS nanocomposites at 325 nm decreases progressively and rapidly, directly indicating that fast electron transfer takes place from photoexcited ZnS nanorods to SnO_2 QDs. Thus, we can suggest that the higher photocatalytic

degradation efficiencies of SnO_2/ZnS nanocomposites result mainly from the enhanced separation rates of photogenerated charges in SnO_2/ZnS heterojunction nanostructures. Finally, compared with pristine ZnS nanorods, the photostability of SnO_2/ZnS nanostructures is also enhanced due to the protection and charge-separation effects of decorating SnO_2 QDs.

2.6. Acknowledgements

This work has been supported by the National Research Foundation of Korea (2015-051798).

2.7. References

(1) P.V. Kamat, D. Meisel, *Curr. Opin. Colloid Interface Sci*., **2002**, *7*, 282.

(2) R. Marschall, *Adv. Funct. Mater.*, **2014**, *24*, 2421.

(3) H. Wang, L. Zhang, Z. Chen, J. Hu, S. Li, Z. Wang, J. Liu, X. Wang, *Chem. Soc. Rev*., **2014**, *43*, 5234.

(4) H.-B. Kim, H. Kim, W.I. Lee, D.-J. Jang, *J. Mater. Chem. A*, **2015**, *3*, 9714.

(5) A. Kudo, Y. Miseki, *Chem. Soc. Rev*., **2009**, *38*, 253.

(6) Y. Kim, H.-B. Kim, D.-J. Jang, *J. Mater. Chem. A*, **2014**, *2*, 5791.

(7) K. Li, R. Chen, S.-L. Li, M. Han, S.-L. Xie, J.-C. Bao, Z.-H. Dai, Y.-Q. Lan, *Chem. Sci*., **2015**, *6*, 5263.

(8) H.-B. Kim, D.-J. Jang, Nanoscale, **2016**, *8*, 403.

(9) D. Wang, H. Zhao, N. Wu, M.A. El Khakani, D. Ma, *J. Phys. Chem. Lett*., **2010**, *1*, 1030.

(10) B.-R. Hyun, Y.-W. Zhong, A.C. Bartnik, L. Sun, H.D. Abruna, F.W. Wise, J.D. Goodreau, J.R. Matthews, T.M. Leslie, N.F. Borrelli, *ACS Nano*, **2008**, *2*, 2206.

(11) X. Yu, J. Yu, B. Cheng, B. Huang, *Chem. Eur. J*., **2009**, *15*, 6731.

(12) G. Wang, B. Huang, Z. Li, Z. Lou, Z. Wang, Y. Dai, M.-H. Whangbo, *Sci. Rep*., **2015**, *5*, 8544.

(13) J.S. Hu, L.L. Ren, Y.G. Guo, H.P. Liang, A.M. Cao, L.J. Wan, C.L. Bai, *Angew. Chem. Int. Ed*., **2005**, *117*, 1295.

(14) K. Chakraborty, S. Chakrabarty, P. Das, S. Ghosh, T. Pal, *Mater. Sci. Eng. B*, **2016**, *204*, 8.

(15) J. Zhang, L. Wang, X. Liu, X.a. Li, W. Huang, *J. Mater. Chem. A*, **2015**, *3*, 535.

(16) J. Zhang, Q. Zhang, L. Wang, W. Huang, *Sci. Rep*., **2016**, *6*, 27241.

(17) J. Zhang, Q. Wang, L. Wang, X.a. Li, W. Huang, *Nanoscale*, **2015**, *7*, 10391.

(18) Q. Li, H. Meng, P. Zhou, Y. Zheng, J. Wang, J. Yu, J. Gong, *ACS Catal*., **2013**, *3*, 882.

(19) S. Ham, Y. Kim, M.J. Park, B.H. Hong, D.-J. Jang, *RSC Adv*., **2016**, *6*, 24115.

(20) X. Yang, H. Xue, J. Xu, X. Huang, J. Zhang, Y.-B. Tang, T.-W. Ng, H.-L. Kwong, X.-M. Meng, C.-S. Lee, *ACS Appl. Mater. Interfaces*, **2014**, *6*, 9078.

(21) J. Zhang, J. Yu, Y. Zhang, Q. Li, J.R. Gong, *Nano Lett*., **2011**, *11*, 4774-.

(22) P.-J. Wu, J.-W. Yu, H.-J. Chao, J.-Y. Chang, *Chem. Mater*., **2014**, *26*, 3485.

(23) M. Kwiatkowski, I. Bezverkhyy, M. Skompska, *J. Mater. Chem. A*, **2015**, *3*, 12748.

(24) J. Lahiri, M. Batzill, *J. Phys. Chem. C*, **2008**, *112*, 4304.

(25) Z. Wang, S.-W. Cao, S.C.J. Loo, C. Xue, *CrystEngComm*, **2013**, *15*, 5688.

(26) Y. Min, G. He, Q. Xu, Y. Chen, *J. Mater. Chem. A*, **2014**, *2*, 2578.

(27) C. Wang, C. Shao, X. Zhang, Y. Liu, *Inorg. Chem*., **2009**, *48*, 7261.

(28) L. Zhu, M. Hong, G.W. Ho, *Sci. Rep*., **2015**, *5*, 11609.

(29) S. Khanchandani, S. Kundu, A. Patra, A.K. Ganguli, *J. Phys. Chem. C*, **2012**, *116*, 23653.

(30) K.-T. Lee, C.-H. Lin, S.-Y. Lu, *J. Phys. Chem. C*, **2014**, *118*, 14457.

(31) Y. Liu, P. Zhang, B. Tian, J. Zhang, *ACS Appl. Mater. Interfaces*, **2015**, *7*, 13849.

(32) Z.-J. Jiang, D.F. Kelley, *J. Phys. Chem. C*, **2011**, *115*, 4594.

(33) Y. Kim, S.J. Kim, S.-P. Cho, B.H. Hong, D.-J. Jang, *Sci. Rep*., **2015**, *5*, 12345.

(34) S. Liu, N. Zhang, Z.-R. Tang, Y.-J. Xu, *ACS Appl. Mater. Interfaces,* **2012**, *4*, 6378.

(35) Y. Liu, Y. Jiao, Z. Zhang, F. Qu, A. Umar, X. Wu, *ACS Appl. Mater. Interfaces*, **2014**, *6* 2174.

(36) X. Meng, F. Wu, J. Li, *J. Phys. Chem. C,* **2011**, *115*, 7225.

(37) X. Huang, Y.-Q. Yu, J. Xia, H. Fan, L. Wang, M.-G. Willinger, X.-P. Yang, Y. Jiang, T.-R. Zhang, X.-M. Meng, *Nanoscale*, **2015**, *7*, 5311.

(38) K. Vinodgopal, I. Bedja, P.V. Kamat, *Chem. Mater*., **1996**, *8*, 2180.

(39) K.K. Akurati, A. Vital, R. Hany, B. Bommer, T. Graule, M. Winterer, *Int. J. Photoenergy*, **2005**, *7*, 153.

(40) M.T. Uddin, Y. Nicolas, C. Olivier, T. Toupance, L. Servant, M.M. Müller, H.-J. Kleebe, J.r. Ziegler, W. Jaegermann, *Inorg. Chem*. **2012**, *51*, 7764.

(41) X. Xu, J. Zhuang, X. Wang, *J. Am. Chem. Soc*., **2008**, *130*, 12527.

(42) S.-K. Park, S.-H. Yu, N. Pinna, S. Woo, B. Jang, Y.-H. Chung, Y.-H. Cho, Y.-E. Sung, Y. Piao, *J. Mater. Chem.*, **2012**, *22*, 2520.

(43) H. Zhu, D. Yang, G. Yu, H. Zhang, K. Yao, *Nanotechnology*, **2006**, *17*, 2386.

(44) Y. Kim, D.-J. Jang, *CrystEngComm*, **2014**, *16*, 6989.

(45) Z. Liu, D.D. Sun, P. Guo, J.O. Leckie, *Nano Lett*., **2007**, *7*, 1081.

(46) S. Yan, D. Hu, F. Hu, J. Wu, N. Huang, Z. Xiao, *CrystEngComm,* **2011**, *13*, 4580.

(47) Y.-P. Zhu, J. Li, T.-Y. Ma, Y.-P. Liu, G. Du, Z.-Y. Yuan, *J. Mater. Chem. A*, **2014**, *2*, 1093.

(48) X. Zhang, J. Qin, Y. Xue, P. Yu, B. Zhang, L. Wang, R. Liu, *Sci. Rep*., **2014**, *4*, 4596.

(49) P. Kundu, P.A. Deshpande, G. Madras, N. Ravishankar, *J. Mater. Chem*., **2011**, *21*, 4209.

(50) P. Guo, J. Jiang, S. Shen, L. Guo, *Int. J. Hydrogen Energy*, **2013**, *38*, 13097.

(51) S. Hernández, V. Cauda, A. Chiodoni, S. Dallorto, A. Sacco, D. Hidalgo, E. Celasco, C.F. Pirri, *ACS Appl. Mater. Interfaces*, **2014**, *6*, 12153.

(52) K. Yu, S. Yang, H. He, C. Sun, C. Gu, Y. Ju, *J. Phys. Chem. A*, **2009**, *113*, 10024.

(53) J. Lee, D.-J. Jang, *J. Phys. Chem. C*, **2016**, *120*, 4130.

(54) D. Chen, H. Zhang, S. Hu, J. Li, *J. Phys. Chem. C*, **2008**, *112*, 117.

(55) X. Huang, L. Shang, S. Chen, J. Xia, X. Qi, X. Wang, T. Zhang, X.-M. Meng, *Nanoscale*, **2013**, *5*, 3828.

(56) J. Lee, H.S. Shim, M. Lee, J.K. Song, D. Lee, *J. Phys. Chem. Lett*., **2011**, *2*, 2840.

(57) I.V. Lightcap, P.V. Kamat, *J. Am. Chem. Soc*., **2012**, *134*, 7109.

(58) J. Sun, H. Zhang, L.-H. Guo, L. Zhao, *ACS Appl. Mater. Interfaces,* **2013**, *5*, 13035.

(59) K.-I. Ishibashi, A. Fujishima, T. Watanabe, K. Hashimoto, *Electrochem. Comm*., **2000**, *2*, 207.

(60) Q. Xiang, D. Lang, T. Shen, F. Liu, *Appl. Catal. B: Environ*., **2015**, *162*, 196.

Chapter 3. Facile Fabrication of Cu-Exchanged ZnS Nanoadsorbents for Highly Efficient Removal of Contaminants[†]

[†]This is reproduced from Jaewon Lee, Sooho Ham, and Du-Jeon Jang, *J. Environ. Chem. Eng.*, **2017**, *5*, 4431.

3.1. Abstract

Cu(I)-exchanged ZnS nanoadsorbents having highly efficient adsorption performances toward cationic dyes and heavy metals have been fabricated via facile cation exchange using pristine ZnS nanostructures as templates. Their surface properties such as surface charges and areas have been controlled by adjusting the molar ratio of Cu to Zn ($R_{Cu/Zn}$). The adsorption efficiency of Cu-exchanged ZnS nanoadsorbents is highest at a $R_{Cu/Zn}$ value of 0.4 because the net surface charges of the nanocomposites resulting from the substitution of Cu(I) ions for Zn(II) ions in the ZnS lattice are electronically most negative. Both the surface areas and the total pore volumes of Cu-exchanged ZnS nanocomposites are also largest at a $R_{Cu/Zn}$ value of 0.4, supporting that Cu-exchanged ZnS ($R_{Cu/Zn}$ = 0.4) nanocomposites have the largest adsorption capacities of cationic dyes. The kinetics and isotherms of adsorption and the effects of various parameters such as concentration, pH, and time on the adsorption process have been also investigated in detail; the adsorption of Cu-exchanged ZnS nanorods shows the Langmuir isotherm model with the maximum capacities of 86.6, 57.0, and 53.1 mg g^{-1} for rhodamine B, Co(II), and Ni(II), respectively. The adsorption of cationic dyes to our nanoadsorbents is mainly driven by attractive electrostatic interactions while van der Walls forces also play a role. The composite nanorods have high stability as well in spite of successive reuse. Overall, our prepared Cu-exchanged ZnS

nanoadsorbents are suggested to have great potential applicability in the treatment of wastewater containing cationic dyes or heavy metals.

3.2. Introduction

Nanotechnology has hold enormous potential in environmental remediation and wastewater treatment because nanomaterials have substantially large surface areas to provide enhanced adsorption capability and affinity to pollutants compared to bulk-sized materials.[1-4] Especially, adsorption, membrane separation, coagulation/flocculation, photocatalysis, and disinfection have been investigated broadly using nanomaterials for the treatment of wastewater.[1,2] However, most methods mentioned above are not very successful due to many restrictions as follows: high energy and high cost in photocatalysis,[5-7] high generation of sludge in coagulation/flocculation,[1,2,8,9] and less effectiveness in disinfection.[10] In contrast, adsorption has been one of the most preferred ways to deal with pollutants owing to simplicity and cheapness as well as high efficiency and adsorbent diversity.[2-4,11-18]

Most extensively used are carbon-based adsorbents, which are suitable for the elimination of traditional pollutants such as dyes, phenols, organic acids, and heavy metals.[15-18] In particular, graphene-derivatives like carbon nanotubes and graphene oxides have shown considerably stronger binding affinity with organic pollutants and heavy metals via combination of van der Walls forces, electrostatic attraction, and π-π stacking interactions.[17-21] However, these designed and engineered carbon-based materials require high cost in the fabrication process and suffer from the low dispersibility of water.[19-20] Moreover, they are costly in regeneration and non-selective for the removal of

ionic pollutants.[20] Thus, to overcome these drawbacks, alternative materials such as organic matters, natural and synthetic polymers, and inorganic solids have been reported.[3,4,22-26]

Metal sulfides as adsorbents have been hardly studied yet.[12,27] However, micro- and nano-sized metal sulfides can be utilized adequately to manage organic contaminants because their fabrication process is cheap and simple.[27-30] Furthermore, they are abundantly available and environmentally friendly, and they can be easily modified with other materials via being doped with metals and non-metals or via being coupled with other semiconductors.[5,26-33] Among metal sulfides, wurtzite ZnS has been investigated primarily due to not only its great potential in photocatalysis and opto-electronics but also its high thermodynamical stability.[34,35] It is also easily size-controllable, highly mass-producible, relatively inexpensive, and less toxic. One-dimensional (1D) nanostructures such as nanorods and nanobelts have been employed usefully for the purpose of wastewater treatment due to their peculiar structures having nano-micrometer scales, allowing them to be easily separated from water by a simple sedimentation process.[34-37] Furthermore, 1D nanostructures consisting of micro- and mesopores also have large pore volumes and surface areas, which will be also beneficial for efficient liquid transport as well as effective contact with pollutants in water.[5,31,37-39] Moreover, theses nano-micro scaled 1D nanostructures can serve as good templates for the formation of hybrid materials that may not only inherit the advantages of their parent materials but

also possess the synergistic effect, further enhancing the water-treatment performances of their parent materials.[37-39]

In this work, we have fabricated Cu(I)-exchanged ZnS nanoadsorbents through facile cation exchange of ZnS nanorods, nanobelts, or nanosheets as templates.[12,28-30] Their surface properties such as surface charges and areas have been controlled by adjusting the molar ratio of Cu to Zn ($R_{Cu/Zn}$). The adsorption efficiency of Cu-exchanged ZnS nanoadsorbents is highest at a $R_{Cu/Zn}$ value of 0.4 because the net surface charges of the nanocomposites are electronically most negative. The kinetics and isotherms of adsorption and the effects of various parameters such as concentration, pH, and time on the adsorption process have been investigated in detail. We have found that the high removal efficiencies of cationic organic pollutants and heavy metals result from the increased negative surface charges as well as the enhanced surface areas and the total pore volumes of nanocomposites. Overall, our prepared Cu-exchanged ZnS nanoadsorbents can be applied potentially for the treatment of wastewater containing cationic organic dyes and heavy metals.

3.3. Experimental Details

Pristine ZnS Nanostructures. In typical preparation of ZnS nanostructures,[34] 2.0 mmol of $ZnCl_2$, 2.0 mmol of sulfur, 20 mL of ethylenediamine, and 10 mL of $N_2H_4 \cdot H_2O$ were mixed for 2D $ZnS \cdot (en)_{0.5}$

hybrid nanosheets (nanosheets) while 2.0 mmol of $ZnCl_2$, 2.0 mmol of sulfur, 7.5 mL of ethylenediamine, and 22.5 mL of $N_2H_4 \cdot H_2O$ were blended for 1D $ZnS \cdot (en)_{0.5}$ hybrid nanobelts (nanobelts). Meanwhile, for the preparation of 1D bare-ZnS nanorods (nanorods),[35] 2.0 mmol of $ZnCl_2$, 2.0 mmol of sulfur, 7.5 mL of ethylenediamine, 15 mL of $N_2H_4 \cdot H_2O$, and 7.5 mL of water were combined. Then, the combined solution was loaded into an autoclave of 50 mL capacity. The autoclave was placed in an oven at 180 °C for 9 h and cooled to room temperature. A produced white precipitate was centrifuged, washed with water and ethanol several times to remove impurities, and dried in a vacuum at 60 °C for 6 h.

Cu-Exchanged ZnS Nanocomposites. 40 mg of nanosheets, nanobelts, or nanorods was added into 70 mL of water and sonicated for 5 min. Then, the suspension was sealed and heated to 60 °C. A certain amount of CuCl(s) was added into the suspension and stirred for 1 h. Note that $R_{Cu/Zn}$, the molar ratio of Cu to Zn in the final mixture, was varied from 0.0 to 0.8. Resultant products were washed with water and ethanol several times and dried in a vacuum at 60 °C for 6 h to produce Cu-exchanged ZnS nanocomposites.

Characterization. Field emission scanning electron microscopy (SEM) images were obtained with a Zeiss MERLIN Compact microsocpe while transmission electron microscopy (TEM) images were taken with a Hitachi H-7600 microscope. High-angle annular dark-field (HAADF) scanning TEM (STEM) images and energy-dispersive X-ray (EDX) elemental profiles were

recorded employing a JEOL JEM-2100F microscope, whereas high-resolution X-ray diffraction (HRXRD) patterns were obtained with a Bruker D8 DISCOVER diffractometer utilizing Cu K_α radiation (0.15418 nm). High-resolution TEM (HRTEM) images and fast Fourier transformation (FFT) patterns were measured using a Tecnai F20 microscope. X-ray photoelectron spectroscopy (XPS) was conducted employing a KRATOS AXIS-HSi spectrometer having a 150 W Mg anode with a scan step of 0.1 eV, and the recorded binding energies were calibrated with the C 1s peak of contaminated carbon at 284.6 eV. UV-visible absorption spectra were obtained using a Scinco S-3100 spectrometer. N_2 adsorption–desorption measurements for the analysis of surface areas and pore volumes were performed utilizing a Micromeritics ASAP 2020 instrument while zeta potentials for the evaluation of surface charges were measured at room temperature using a Malvern Instruments Zetasizer Nano ZS apparatus. Thermo gravimetric analysis (TGA) was conducted using a TA Instruments Q-5000 IR analyzer, whereas a Varian 820-MS inductively coupled plasma mass spectrometer (ICP-MS) was employed for the concentration detection of heavy-metal ions. pH was measured with a Mettler-Toledo SevenEasy S20 instrument.

Adsorption Experiments. Batch adsorption experiments at room temperature were performed to investigate the adsorption capacities, kinetics, and isotherms using various dyes of RhB, MB, MO, and LGY. Dye removal efficiencies were measured by montoring the adsorption reactions of dyes to pristine and Cu-exchanged ZnS nanoadsorbents. In a typical experiment, 10 mg

of nanoadsorbents was suspended into 72 mL of water, and then 8.0 mL of a dye aqueous solution with a specific dye concentration was transferred into the suspension, which was then stirred for a given period. The amount of a dye adsorbed on pristine or Cu-exchanged ZnS nanoadsorbents at equilibrium, q_e (mg/g), was calculated by the following equation;[15-21,40]

$$q_e = (C_0 - C_e)V/M \quad (1)$$

where C_0 and C_e (mg/L) are the initial and equilibrium concentrations of the dye, respectively, V (L) is the volume of the dye solution, and M (g) is the mass of the suspended nanoadsorbents. Meanwhile, for adsorption kinetic experiments, the adsorption capacity at time t (min) was calculated by the following equation;[21,40]

$$q_t = (C_0 - C_t)V/M \quad (2)$$

where C_t is the concentration of the dye at a scheduled time t (min). The dye-removal efficiency was calculated by the following equation:[20,40]

$$\text{removal efficiency (\%)} = (1 - C_t / C_0)\ 100 \quad (3)$$

To investigate the reusability of Cu-exchanged ZnS nanoadsorbents, used nanoadsorbents were separated from the reaction mixture by centrifugation at 13000 rpm for 10 min. The collected nanoadsorbents were added into 50 mL of ethanol, stirred for 10 min, and then centrifuged again at 13000 rpm for 10 min.[12,19] Then, the recovered nanoadsorbents was added into a mixture solution containing new RhB molecules to initiate another reaction cycle. Adsorption experiments were repeated for 5 times under the same conditions. For the adsorption experiments of heavy metals, 40 mg of Cu-exchanged ZnS nanorods

($R_{Cu/Zn}$ = 0.4) was suspended in 50 mL of an aqueous solution containing 63 μmol of Ni^{2+} or 77 μmol of Co^{2+} and stirred at 800 rpm for 24 h. After adsorption, the concentrations of heavy metals in respective solutions were measured by using ICP-MS.

3.4. Results and Discussion

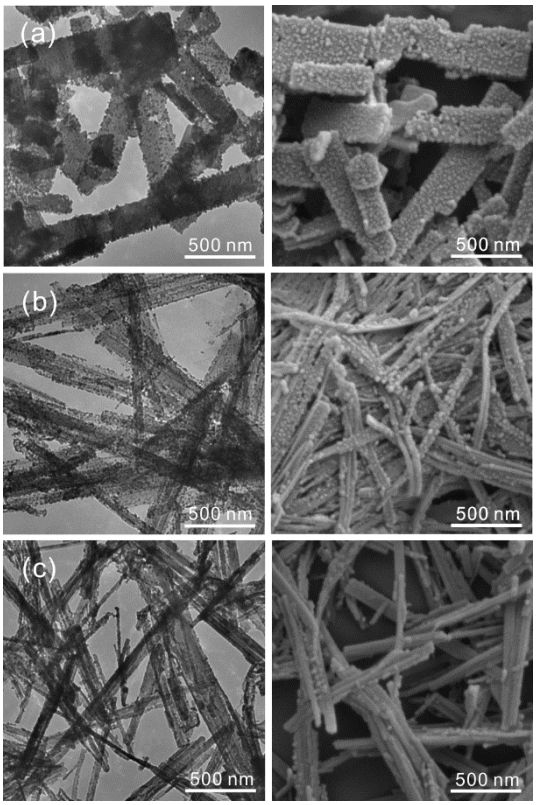

Figure 3-1. TEM (left) and SEM (right) images of Cu-exchanged ZnS ($R_{Cu/Zn}$ = 0.4) nanosheets (a), nanobelts (b), and nanorods (c).

In order to investigate the morphologies and structures of Cu-exchanged ZnS ($R_{Cu/Zn}$ = 0.4) nanosheets, nanobelts, and nanorods, SEM and TEM images have been measured. As-prepared nanosheets have two dimensional (2D) morphologies with an average width of 500±150 nm and an average length of 1.1±0.3 μm (Figure 3-1a) while nanobelts have 1D morphologies with an average width of 130±40 nm and average length of 4.6±1.3 μm (Figure 3-1b). In the case of nanorods having 1D morphologies (Figure 3-1c), their typical length is as short as 2.1±0.4 μm and their average width is as narrow as 70±19 nm because en molecules, acting as solvent-coordinating molecular templates, have been removed with water during their synthetic process.[34,35] We have used CuCl as a Cu(I) precursor to exchange some Zn^{2+} ions of pristine ZnS nanostructures with Cu^{+} ions. The cation-exchange reaction (CER) of ZnS nanostructures by Cu^{+} is favorable because the solubility products (K_{sp}) of ZnS and Cu_2S at room temperature are 1 x 10^{-24} and 2 x 10^{-48}, respectively;[41] the standard Gibbs free energy of $ZnS_{(s)} + 2Cu^{+}_{(aq)} \rightarrow Cu_2S_{(s)} + Zn^{2+}_{(aq)}$ at room temperature is calculated as -135 kJ mol^{-1}.[31] As the thermodynamically favorable CER occurs initially from the outer surfaces of ZnS nanostructures, exchanged Cu atoms are distributed more abundantly on the outer shells of ZnS nanocomposites. All the Cu-exchanged ZnS nanocomposites have rough surfaces and large pores compared with respective pristine ZnS nanostructures having smooth surfaces because the ionic radius of Zn^{2+} (74 pm) is smaller than the ionic radius of Cu^{+} (77 pm).[28] However, because the radius difference is insignificant, the overall structures of initial pristine ZnS nanostructures

including widths and lengths have been preserved to some extent during CER, indicating that CER has induced merely the substitution of Zn^{2+} with Cu^{+} in ZnS nanostructures.

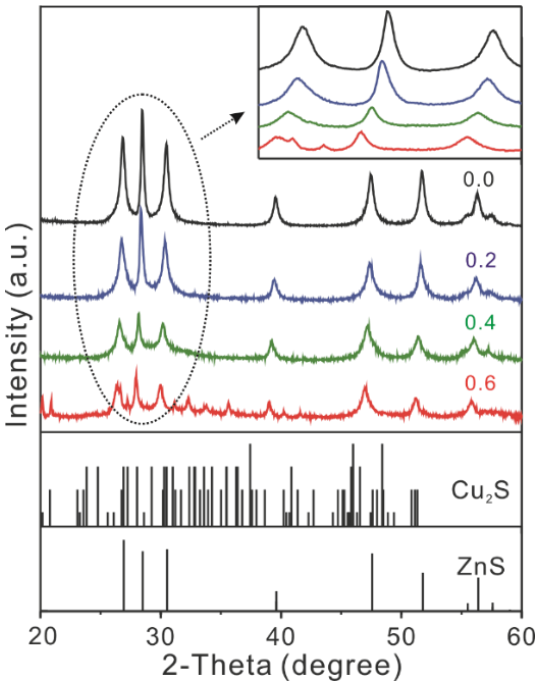

Figure 3-2. HRXRD patterns of Cu-exchanged ZnS nanorods with indicated $R_{Cu/Zn}$ values. The standard diffraction lines of orthorombic Cu_2S and wurtzite ZnS are also shown for comparison.

The crystal structure, phase purity, and average crystallite size of as-prepared samples have been examined by measuring the HRXRD patterns of Figure 3-2. All the HRXRD patterns of pristine and Cu-exchanged ZnS nanorods coincide with the standard diffraction peaks of hexagonal ZnS (JCPDS card no. 36-1450); neither impurity peaks nor Cu-related peaks are observed when $R_{Cu/Zn}$ is 0.2 or 0.4. We consider that when $R_{Cu/Zn}$ is low, the exchange of Zn^{2+} by Cu^{+} not only hardly affects the wurtzite ZnS phase

sturcture but also makes Cu^{+} ions effectively diffuse into the lattices of ZnS nanostructures to form solid solutions, producing negative surface charges.[12] However, above the critical $R_{Cu/Zn}$ value of 0.6, secondary phases corresponding to orthorombic Cu_2S have been produced, inducing the phase segragation to decrease negative surface charges. The inset of Figure 3-2 shows that the peak positions of ZnS shift toward lower angles with the increase of $R_{Cu/Zn}$, implying an expansion of the lattice constants which can be attributed to the substitution of Zn^{2+} having the smaller diameter with Cu^{+} having the larger diameter.[28,38,42-44] The average crystallite sizes of ZnS in Cu-exchanged ZnS nanocomposties have been estimated from the (110) diffraction-peak widths of hexagonal ZnS using the Scherrer's equation;[5-7,15] the average crystallite size (9.0 nm) of Cu-exchagned ZnS nanorods ($R_{Cu/Zn}$ = 0.4) is substantially smaller than that (12.8 nm) of pristine ZnS nanorods as Cu exchange reduces the crystallinity of the ZnS lattice.[42] Nevertheless, the diffraction peaks of ZnS in nanocomposites are still very sharp, confirming that the crystallinity of ZnS remains high even after the formation of Cu-exchanged ZnS nanorods.[5]

The HRTEM images of Figure 3-3a and b display that the lattice spacings 0.317 and 0.333 nm of a Cu-exchanged ZnS ($R_{Cu/Zn}$ = 0.4) nanorod agree reasonably well with the standard spacings 0.313 and 0.331 nm of the (002) and (100) planes of hexagonal ZnS, respectively, indicating that our fabricated nanorod has good crystallinity with some noticeable defects such as stacking faults or twin boundaries.[38,39,45] Defective regions, viewed as stacking faults throughout the crystal lattice of the nanorod, are considered to arise from lattice

mismatches and consequent lattice deformation,[29,45] because Zn^{2+} ions with a smaller radius have been substituted by Cu^{+} ions with a larger radius via CER. Furthermore, the stacking faults are side by side and perpendicular to the growth direction of the nanostructure, suggesting that the incorporation of Cu^{+} into the Zn^{2+} site has taken place in a layer-by-layer fashion without changing parent morphologies.[6]

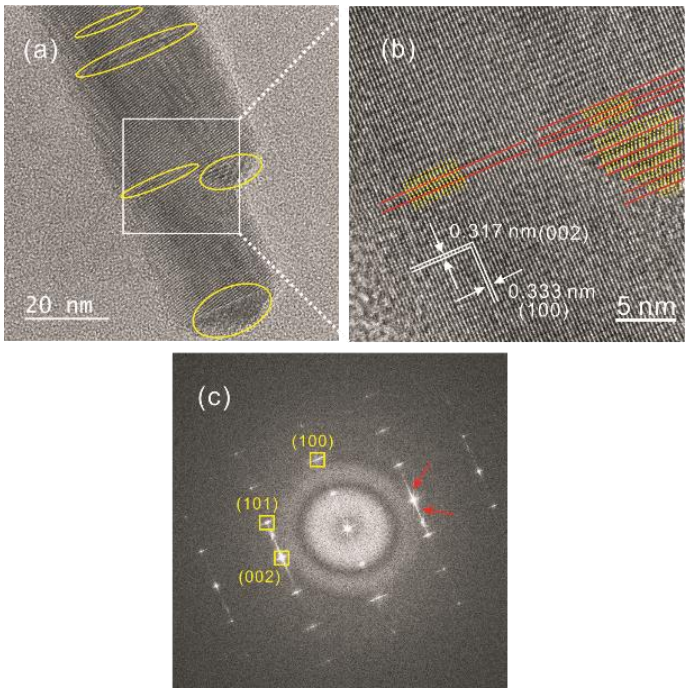

Figure 3-3. HRTEM images (a and b) and FFT pattern (c) of a Cu-exchanged ZnS ($R_{Cu/Zn}$ = 0.4) nanorod. The yellow marks of the panel a and the yellow lines of the panel b indicate stacking faults and planar defects, respectively, while the red lines of the panel b and the red arrows of the panel c designate lattice alignments and defect sites, respectively.

The FFT pattern of the nanorod supports as well that Zn^{2+} ions have been successfully replaced by Cu^{+} ions via CER because the lattice fringes of 0.334,

0.317, and 0.295 nm calculated from the FFT pattern of Figure 3-3c match adequately with the standard spacings of the (100), (002), and (101) planes, respectively, of hexagonal ZnS. In addition, the existence of some streaky spots within the FFT pattern demonstrates that defect sites have been generated in Cu-exchanged ZnS nanocomposites.[30,39,44]

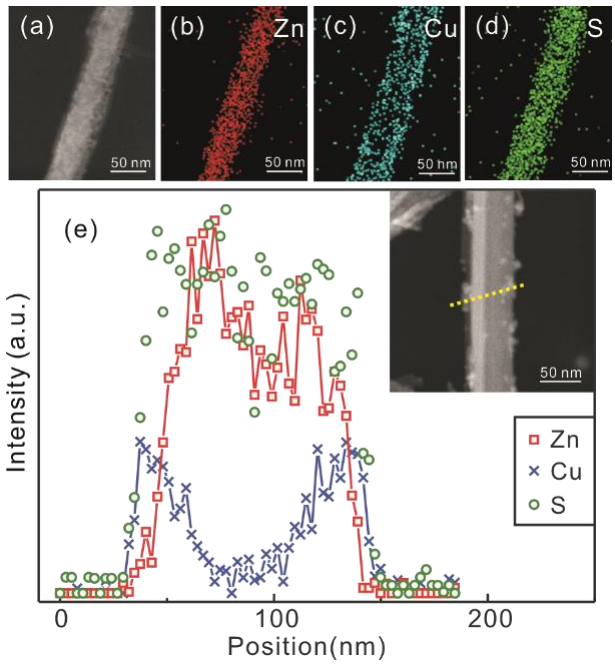

Figure 3-4. HAADF STEM image (a), EDX elemental mapping images (b-d), and area-normalized line-scanned elemental intensity profiles (e) of a Cu-exchanged ZnS ($R_{Cu/Zn}$ = 0.4) nanorod for Zn, Cu, and S along the indicated line of the insetted HAADF STEM image.

To further verify the chemical composition and distribution of a Cu-exchanged ZnS nanorod, elemental analysis has been carried out by monitoring the HAADF STEM mode of EDX; the HAADF STEM image of Figure 3-4a indicates that the surface of the composite nanorod is rough in comparison with

the smooth surface of a pristine ZnS nanorod. Furthermore, the EDX elemental mapping images of Figure 3-4b-d support that Cu atoms are well distributed homogeneously on the surface of the composite nanorod. Especially, the distribution of Cu atoms has a tubular structure because CER has started from the outer surface of a ZnS nanorod and diffused into the central part of ZnS to exchange Zn atoms with Cu atoms.[29,31] The line-scanned EDX elemental profiles, as well as the insetted STEM image, of Figure 3-4e indicate more clearly that the CER of Zn^{2+} ions with Cu^{+} ions has started from the outer surface of a ZnS nanorod. In particular, the calculated molar ratios of Cu to Zn in Cu-exchanged ZnS nanocomposites are nearly the same as $R_{Cu/Zn}$, suggesting that almost every Cu^{+} ion added in the mixture solution has substituted for Zn^{2+}. Based on our results, it can be concluded that as the morphologies of Cu-exchanged ZnS nanocomposites resemble those of pristine ZnS nanostructures regardless of CER, all the added Cu^{+} ions have been incorporated in the Zn^{2+} lattice.

XPS has been utilized to study the surface chemical states of obtained Cu-exchanged ZnS ($R_{Cu/Zn}$ = 0.4) nanorods. The binding energies (BEs) of Zn $2p_{3/2}$ and Zn $2p_{1/2}$ were measured as 1044.91 and 1021.71 eV, respectively, (Figure 3-5a) while the BEs of S $2p_{3/2}$ and S $2p_{1/2}$ were observed as 161.41 and 162.70 eV, respectively (Figure 3-5b).[5,34,35] Compared with the Zn and S XPS spectra of pristine ZnS nanorods, the Zn and S spectra of Cu-exchanged ZnS nanorods have been shifted to higher BEs by 0.75 and 0.65 eV, respectively. This supports that Zn with a lower electronegativity of 1.6 has been replaced by Cu with a

higher electronegativity of 1.9 via CER. Two sharp peaks at 932.11 and 952.04 eV, assigned to Cu $2p_{3/2}$ and Cu $2p_{1/2}$ respectively, appear in the Cu 2p spectrum, representing that exchanged Cu atoms exist in the form of Cu^{+} in our Cu-exchanged ZnS nanocomposites because satellite peaks arising from electron shake up of the Cu^{2+} $3d^9$ configuration around 940 and 960 eV are not observable.[28,32,46,47] Thus, the XPS data also reveal well that Cu^{+} has been successfully incorporated in the lattice of ZnS nanorods in substitution for Zn^{2+} via CER.

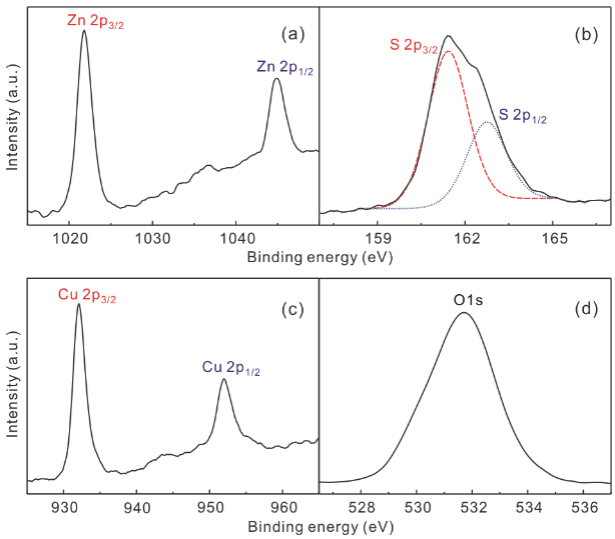

Figure 3-5. Zn 2p (a), S 2p (b), Cu 2p (c), and O 1s (d) XPS spectra of Cu-exchanged ZnS ($R_{Cu/Zn}$ = 0.4) nanorods. The S 2p spectrum has been deconvoluted into two Gaussian curves.

In order to optimize $R_{Cu/Zn}$ values, batch adsorption experiments of Cu-exchanged ZnS nanocomposites having different $R_{Cu/Zn}$ values were carried out for the removal of RhB from water.[25,48] As shown in Figure 3-6, briefly, with the increase of $R_{Cu/Zn}$ from 0.0 to 0.4, the removal efficiency of RhB increases

for all the nanocomposites involving nanorods, nanobelts, and nanosheets. However, the efficiency decreases gradually with the increase of $R_{Cu/Zn}$ at high $R_{Cu/Zn}$ values because negative surface charges of nanocomposites decrease with the generation of Cu_2S nanocrystals. Meanwhile, composite nanorods have higher adsorption performances than any other composite adsorbents because nanorods have less en molecules which not only reduce active surface sites and pore volumes to adsorb dye molecules but also interrupt interactions between dye molecules and active sites (see below). Thus, it can be summarized that the optimal $R_{Cu/Zn}$ value is 0.4 while the nanorods are the optimal morphology for the removal of RhB from water.

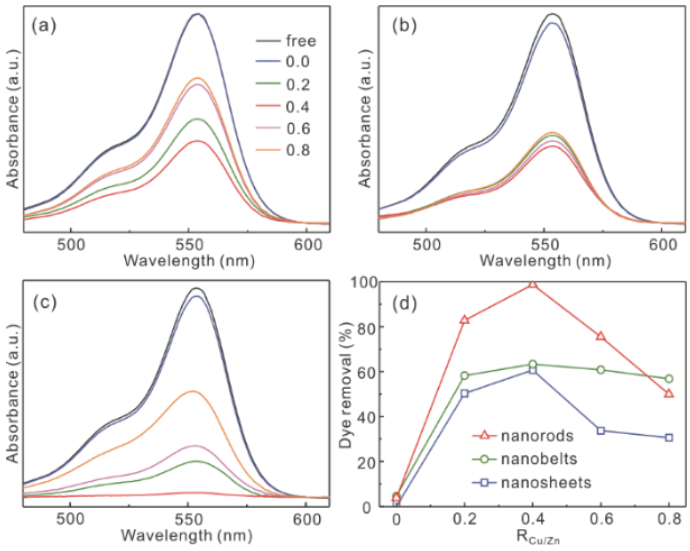

Figure 3-6. Absorption spectra of RhB after adsorption on Cu-exchanged ZnS nanosheets (a), nanobelts (b), and nanorods (c) with indicated $R_{Cu/Zn}$, where 'free' indicates nanocomposites-free. Removal percentages of RhB depending on the $R_{Cu/Zn}$ values of indicated nanocomposites (d). (RhB concentration, 10 μM; adsorbent dosage, 0.125 g/L; contact time, 180 min)

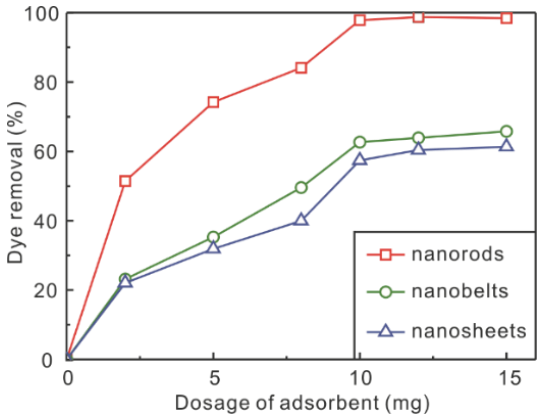

Figure 3-7. Dosage effect of indicated Cu-exchanged ZnS nanoadsorbents with a $R_{Cu/Zn}$ value of 0.4 on the removal percentage of RhB.

The adsorbent dosage is one of the important parameters for the evaluation of the adsorption efficiency because it can determine the adsorption capacity of nanoadsorbents for a given initial RhB concentration.[24,26,49] Thus, we have studied the dosage effect of dye removal (Figure 3-7); the removal efficiency increases gradually as the amount of adsorbent increases from 0 to 10 mg owing to the increase of available surface adsorption sites. However, the efficiency increases hardly with a further increment of the dosage above 10 mg. A dosage of 10 mg will be chosen hereafter for batch adsorption experiments of dyes such as RhB, MB, MO, and LGY.

The equilibrium time is also a critical point in the design of an economical wastewater treatment system.[49-51] The adsorption capacities of Cu-exchanged ZnS nanocomposites for RhB at various initial concentrations have been investigated as a function of the contact time to discover the adsorption equilibrium time (Figure 3-8).

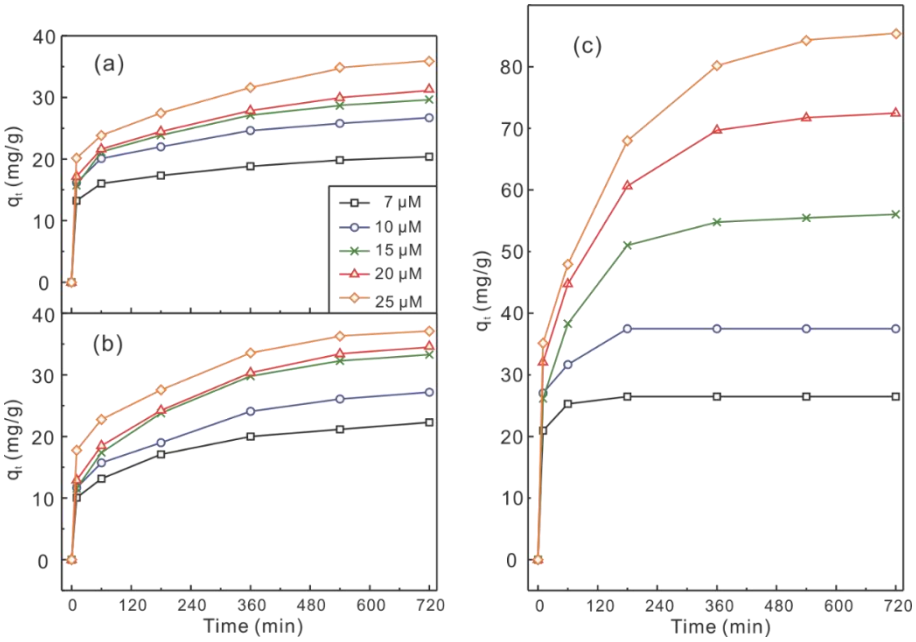

Figure 3-8. Time-dependent q_t of RhB having indicated various initial concentrations in the presence of Cu-exchanged ZnS ($R_{Cu/Zn}$ = 0.4) nanosheets (a), nanobelts (b), and nanorods (c).

The adsorption capacity increases quickly at the initial stage and then slowly to reach the equilibrium value at a contact time of 720 min. Rapid adsorption at the initial contact time is attributed to the negatively charged active sites of nanoadsorbents having large specific surface areas, whereas delayed adsorption arises from the slow diffusion of RhB molecules into the pores of nanoadsorbents.[11] In addition, as displayed in Figure 3-8a-c, the nanorods have a higher adsorption capacity as well as a faster adsorption rate than any other composite adsorbents, also indicating that nanorods having residual en molecules hardly are the best nanoadsorbents among our studied Cu-exchanged ZnS nanocomposites.

The adsorption kinetics of a dye is an important characteristic of nanoadsorbents, giving information with respect to the adsorption efficiency and a possible rate-controlling step. The adsorption kinetic data were obtained from the pseudo-first-order kinetic, the pseudo-second-order kinetic, and the intra-particle diffusion models by using the respective following equations:[14-22]

$$\ln (q_e - q_t) = \ln q_e - k_1 t \quad (4)$$

$$t/q_t = 1/(k_2 q_e^2) + t / q_e \quad (5)$$

$$q_t = k_i t^{1/2} + C \quad (6)$$

where k_1, k_2 and k_i are the pseudo-first-order (min^{-1}), the pseudo-second-order ($g\ mg^{-1}\ min^{-1}$), and the intra-particle diffusion rate constants ($mg\ g^{-1}\ min^{-1/2}$), respectively. q_e and q_t are the adsorption capacities ($mg\ g^{-1}$) of RhB onto Cu-exchanged ZnS ($R_{Cu/Zn} = 0.4$) nanocomposites at equilibrium and time t (min), respectively, and C ($mg\ g^{-1}$) is a constant. Table 3-1 lists the fitted kinetic and diffusion parameters; all the correlation coefficient R^2 values of the pseudo-second-order kinetic model are larger than 0.99, demonstrating that this model describes the adsorption kinetics more accurately than any other calculated models. Furthermore, the theoretically evaluated q_e values of the pseudo-second-order kinetics are very close to the respective experimental q_e values for Cu-exchanged ZnS ($R_{Cu/Zn}$ = 0.4) nanorods. Meanwhile, the intra-particle diffusion model has been introduced to describe the adsorption process of RhB onto our prepared nanoadsorbents.[22] The intra-particle diffusion plot should be linear if the intra-particle diffusion is involved in the adsorption process. If the linear lines pass through the origin, the intra-particle diffusion is the rate-

controlling step.[22,23] Otherwise, the intra-particle diffusion is not the only rate-controlling step; other diffusion mechanism such as outer diffusion (boundary layer diffusion) can simultaneously control the rate of RhB adsorption.[21,22] Although the linear plot has been observed for RhB adsorption onto our nanoadsorbents, the plots do not pass through the origin, manifesting that the intra-particle diffusion is not the sole rate-controlling step. From this result, it can be suggested that both intra-particle diffusion and outer diffusion may play roles in the overall adsorption processes of our composite nanoadsorbents.

Table 3-1. Kinetic and intra-particle diffusion parameters for adsorption of RhB on Cu-exchanged ZnS ($R_{Cu/Zn}$ = 0.4) nanorods at different initial RhB concentrations.

		Pseudo-second-order kinetics			Intraparticle diffusion		
C_0 (μM)	$q_{e,exp}$ (mg/g)	k_2 (10^{-4} /min)	$q_{e,calc}$ (mg/g)	R^2	k_i (mg/ g $min^{1/2}$)	C (mg/g)	R^2
7	26.48	178	26.58	0.9999	0.5273	19.96	0.7233
10	37.49	4.66	37.86	0.9998	1.0194	23.80	0.9999
15	56.04	8.17	57.67	0.9994	1.8426	22.61	0.9156
20	72.68	4.17	75.64	0.9981	2.4179	25.61	0.9794
25	86.56	2.59	90.83	0.9961	2.9196	26.21	0.9880

Adsorption isotherms are necessary to investigate the adsorption capacities of Cu-exchanged ZnS ($R_{Cu/Zn}$ = 0.4) nanocomposites for RhB. Langmuir and Freundlich isotherm models have been fitted with experimental data by employing equation (7) and (8), respectively:[14-20]

$$C_e/q_e = 1/(q_m K_L) + C_e \quad (7)$$

$$\ln q_e = (\ln C_e)/n + \ln K_F \quad (8)$$

where C_e (mg L^{-1}) is the equilibrium concentration of the solution, q_m (mg g^{-1}) is the monolayer adsorption capacity of adsorbents, and K_L (L mg^{-1}) is the Langmuir adsorption constant. In addition, K_F ($mg^{1-(1/n)}$ $L^{1/n}$ g^{-1}) is the Freundlich adsorption constant and n is related to adsorption intensity. Table 3-2 lists all the obtained isotherm parameters. Since the R^2 values of the Langmuir isotherms are closer to1, the Langmuir adsorption model describes the adsorption process of RhB well, suggesting the monolayer adsorption of RhB onto homogeneous surfaces of composite nanoadsorbents with an equal adsorption activation energy.[14,23] We consider that the monolayer adsorption results from the electrostatic attraction of cationic RhB molecules with negative charge surfaces of nanoadsorbents. The dimensionless R_L values of the Langmuir isotherm suggest the adsorption nature, which can be either unfavorable ($R_L > 1$), linear ($R_L = 1$), favorable ($0 < R_L < 1$), or irreversible ($R_L = 0$).[14,23] Every R_L value for RhB with Cu-exchanged ZnS ($R_{Cu/Zn} = 0.4$) nanocomposites is in the range of 0.920-0.996, confirming that the adsorption is favorable for all nanoadsorbents. Furthermore, Table 3-3 shows that Cu-exchanged ZnS ($R_{Cu/Zn}$ =0.4) nanorods have a significantly high adsorption efficiency compared with previously reported inorganic solid adsorbents.[11-14] Their efficiency is even comparable to the efficiencies of well-known graphene-based adsorbents,[9,17-19] implying that our prepared nanorods can be applied to the removal of organic dyes in real life.

Table 3-2. Langmuir and Freundlich isotherm parameters for adsorption of RhB onto Cu-exchanged ZnS ($R_{Cu/Zn}$ = 0.4) nanoadsorbents.

Adsorbents	Langmuir model				Freundlich model		
	Q_m (mg/g)	K_L (L/mg)	R_L	R^2	K_F	*n*	R^2
Rods	96.25	7.215	0.920-0.976	0.9969	89.780	2.737	0.9425
Belts	40.39	1.716	0.979-0.994	0.9964	25.77	4.813	0.9175
Sheets	38.53	1.133	0.986-0.996	0.9671	22.52	4.269	0.8855

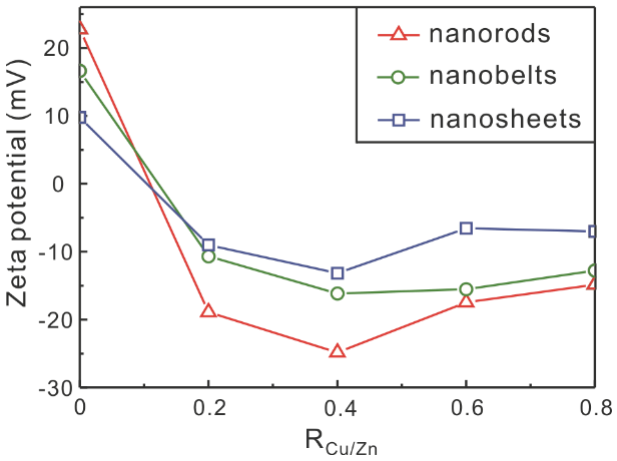

Figure 3-9. $R_{Cu/Zn}$-dependent zeta potentials of indicated Cu-exchanged ZnS nanoadsorbents.

The surface charges of Cu-exchanged ZnS nanoadsorbents with different $R_{Cu/Zn}$ values have been displayed in Figure 3-9, revealing that the zeta potential of composite nanoadsorbents decreases with the increase of $R_{Cu/Zn}$ to increase the adsorption efficiency of RhB until $R_{Cu/Zn}$ reaches 0.4. However, at high $R_{Cu/Zn}$ values, the zeta potential increases with $R_{Cu/Zn}$ gradually due to the formation of Cu_2S nanocrystals. The variation of zeta potential with $R_{Cu/Zn}$ of

composite nanoadsorbents verifies that the Zn^{2+} ions have been substituted well by Cu^{+} ions via CER and that Cu-exchanged ZnS nanocomposites have negative surface charges owing to deficient positive charges.

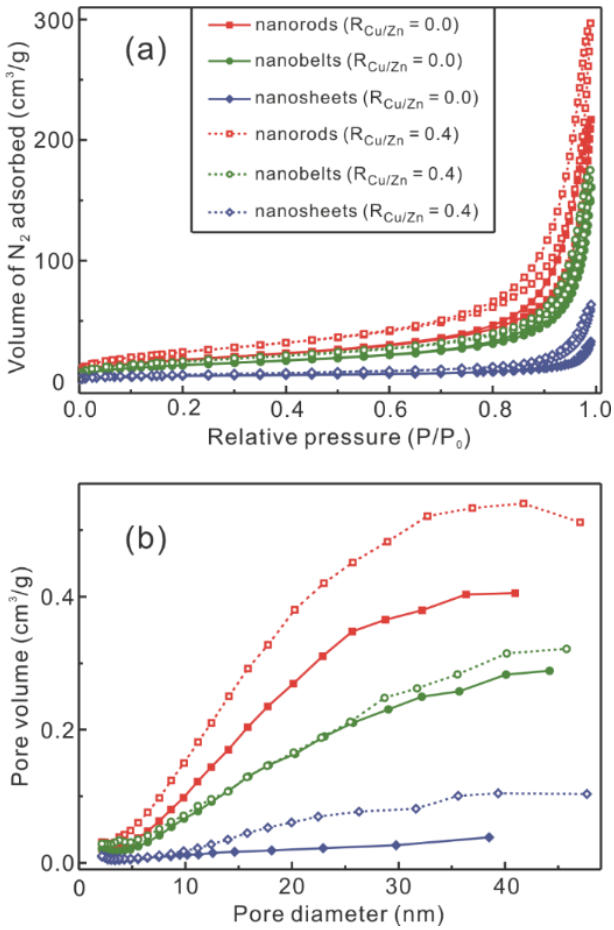

Figure 3-10. N_2 adsorption-desorption isotherms (a) and pore-size distributions (b) of indicated Cu-exchanged ZnS nanoadsorbents.

The high adsorption capacities of nanoadsorbents for dyes can be also related with high specific surface areas, porous structures, and large pore volumes, which offer active sites for dye adsorption.[19,21,23] Thus, we have investigated N_2

adsorption-desorption analysis and the corresponding results are presented in Figure 3-10. Our prepared nanocomposites exhibit type-IV isotherms involving typical type-H3 hysteresis loops (at $P/P_0 > 0.8$) according to the IUPAC classification, suggesting the presence of nanopores.[5,6,40] The Brunauer–Emmett–Teller (BET) surface areas, pore sizes, and total pore volumes of Cu-exchanged ZnS nanocomposites with $R_{Cu/Zn} = 0.0$ or 0.4 are listed. The surface areas and total pore volumes of Cu-exchanged ZnS ($R_{Cu/Zn} = 0.4$) nanocomposites are higher than the respective ones of pristine ZnS nanocomposites. Thus, Cu-exchanged ZnS nanocomposites have higher adsorption ability than respective pristine ZnS nanostructures.[16,17,21] Furthermore, among Cu-exchanged ZnS nanocomposites, nanorods have the highest surface area and the largest total pore volume to have the highest adsorption efficiency because nanorods hardly contain residual en molecules.

Based on the above results, we suggest that the adsorption of RhB to Cu-exchanged ZnS nanocomposites is mainly driven by attractive electrostatic interactions while van der Walls interactions also play a role in the adsorption of the dye. Cationic dyes such as RhB and MB adsorb more strongly to nanocomposites than anionic dyes such as MO and LGY do. This supports that the major driving forces of dye adsorption are coulombic interactions, also indicating that the net surface charges of Cu-exchanged ZnS nanocomposites are electronically negative.

From the view point of application, the regeneration of nanoadsorbents is very important because the nanoadsorbents should be reused for successive

adsorption applications to reduce the whole cost of wastewater treatment. Thus, we have conducted the recycle performances of Cu-exchanged ZnS ($R_{Cu/Zn}$ = 0.4) nanorods for the removal of RhB. Ethanol was employed to desorb RhB molecules completely from the nanoadsorbents to regenerate the nanocomposites for reusage.[12,19,21] Figure 3-11 indicates that the removal efficiency has hardly been reduced even after 5 repeated cycles. The TEM images of Figure 3-11 reveal that the original morphologies and structures of the Cu-exchanged ZnS nanorods have been preserved well after successive repeated processes of adsorption and desorption, suggesting that the composite nanorods can be advantageously employed as eco-friendly, fast, and recyclable adsorbents for wastewater treatment.

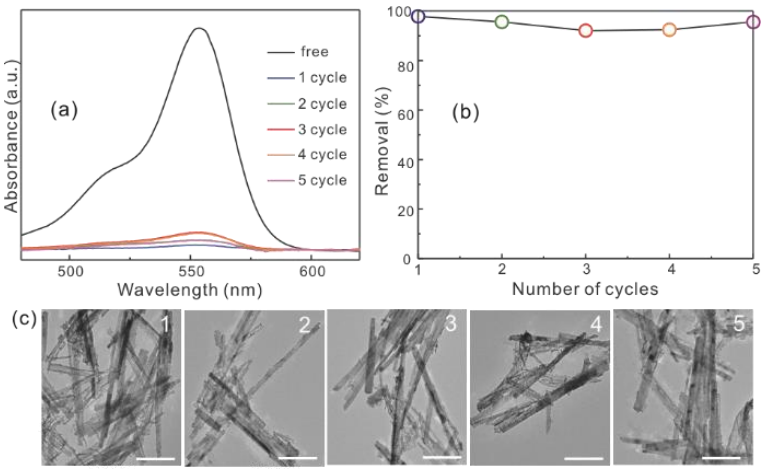

Figure 3-11. Absorption spectra (a) and removal percentages (b) of RhB after indicated different cycles. TEM images of Cu-exchanged ZnS ($R_{Cu/Zn}$ = 0.4) nanoadsorbents reused for indicated cycle times (c), where each scale bar indicates 300 nm. (RhB concentration, 10 μM; adsorbed dosage, 0.125 g/L; contact time, 180 min)

3.5. Conclusion

Cu(I)-exchanged ZnS nanoadsorbents have been fabricated through facile cation exchange of ZnS nanorods, nanobelts, or nanosheets as templates. Their surface properties such as surface areas and charges have been controlled by adjusting the value of $R_{Cu/Zn}$. The adsorption efficiencies of Cu-exchanged ZnS nanoadsorbents have been found to be highest at a $R_{Cu/Zn}$ value of 0.4 because the net surface charges of Cu-exchanged ZnS nanocomposites resulting from the substitution of Cu(I) ions for Zn(II) ions in the ZnS lattice are electronically most negative. In addition, both the surface areas and the total pore volumes of Cu-exchanged ZnS nanocomposites have been found to be largest at an $R_{Cu/Zn}$ value of 0.4. This also explains the reason why Cu-exchanged ZnS ($R_{Cu/Zn} = 0.4$) nanocomposites have the largest adsorption capacities of cationic dyes. The adsorption efficiency of Cu-exchanged ZnS nanorods is much higher than that of Cu-exchanged ZnS nanobelts or nanosheets as nanorods hardly contain residual ethylenediamine molecules. Our results suggest that the adsorption of cationic dyes to our nanoadsorbents is mainly driven by attractive electrostatic interactions while van der Walls forces also play a role. The composite nanorods have been found to have high stability as well in spite of successive reuse. Thus, we suggest that our prepared Cu-exchanged ZnS nanorods can be served as nanoadsorbents in the treatment of wastewater containing cationic organic dyes or heavy metals.

3.6. Acknowledgements

This work was supported by research grants through the National Research Foundation (NRF) of Korea funded by the Korean government (2017-006153 and 2015-051798).

3.7. References

(1) X. Qu, P. J. Alvarez, Q. Li, *Water Res.*, **2013**, *47*, 3931.

(2) X. Qu, J. Brame, Q. Li, P. J. J. Alvarez, *Acc. Chem. Res.*, **2013**, *46*, 834.

(3) M. Khajeh, S. Laurent, K. Dastafkan, *Chem. Rev.*, **2013**, *113*, 7728.

(4) P. Z. Ray, H. J. Shipley, *RSC Adv.*, **2015**, *5*, 29885.

(5) J. Lee, Y. Kim, J. K. Kim, S. Kim, D.-H. Min, D.-J. Jang, *Appl. Catal. B: Environ.*, **2017**, *205*, 433.

(6) H.-B. Kim, H. Kim, W. I. Lee, D.-J. Jang, *J. Mater. Chem. A*, **2015**, *3*, 9714.

(7) Y. Kim, H.-B. Kim, D.-J. Jang, *J. Mater. Chem. A*, **2014**, *2*, 5791.

(8) C. Y. Teh, P. M. Budiman, K. P. Y. Shak, T. Y. Wu, *Ind. Eng. Chem. Res.*, **2016**, *55*, 4363.

(9) J. Ding, B. Li, Y. Liu, X. Yan, S. Zeng, X. Zhang, L. Hou, Q. Cai, J. Zhang, *J. Mater. Chem. A*, **2015**, *3*, 832.

(10) Q. Li, S. Mahendra, D. Y. Lyon, L. Brunet, M. V. Liga, D. Li, P. J. J. Alvarez, *Water Res.*, **2008**, *42*, 4591.

(11) J. Han, G. Zhu, M. Hojamberdiev, J. Peng, X. Zhang, Y. Liu, B. Ge, P. Liu, *New J. Chem.*, **2015**, *39*, 1874.

(12) Y. Wang, D. Chen, Y. Wang, F. Huang, Q. Hu, Z. Lin, *Nanoscale*, **2012**, *4*, 3665.

(13) Y. Yu, M. Zhu, W. Liang, S. Rhodes, J. Fang, *RSC Adv.*, **2015**, *5*, 72437.

(14) D. P. Dutta, A. Singh, A. Ballal, A. K. Tyagi, *Eur. J. Inorg. Chem.*, **2014**, *2014*, 5724.

(15) H. Gu, H. Lou, J. Tian, S. Liu, Y. Tang, *J. Mater. Chem. A*, **2016**, *4*, 10174.

(16) S. Venkateswarlu, D. Lee, M. Yoon, *ACS Appl. Mater. Interfaces*, **2016**, *8*, 23876.

(17) Y. Liu, X. Jiang, B. Li, X. Zhang, T. Liu, X. Yan, J. Ding, Q. Cai, J. Zhang, *J. Mater. Chem. A*, **2014**, *2*, 4264.

(18) Z. Sui, Q. Meng, X. Zhang, R. Ma, B. Cao, *J. Mater. Chem.*, **2012**, *22*, 8767.

(19) J. Zhao, W. Ren, H.-M. Cheng, *J. Mater. Chem.*, **2012**, *22*, 20197.

(20) J. Xiao, W. Lv, Z. Xie, Y. Tan, Y. Song, Q. Zheng, *J. Mater. Chem. A*, **2016**, *4*, 12126.

(21) F. Yu, J. Ma, S. Han, *Sci. Rep.*, **2014**, *4*, 5326.

(22) I. Kiran, T. Akar, A. S. Ozcan, A. Ozcan, S. Tunali, *Biochem. Eng. J.*, **2006**, *31*, 197.

(23) B. Cheng, Y. Le, W. Cai, J. Yu, *J. Hazard. Mater.*, **2011**, *185*, 889.

(24) R. K. Sharma, A. Puri, Y. Monga, A. Adholeya, *J. Mater. Chem. A*, **2014**, *2*, 12888.

(25) A. Meng, J. Xing, Z. Li, Q. Li, *ACS Appl. Mater. Interfaces*, **2015**, *7*, 27449.

(26) T. Zhu, J. S. Chen, X. W. Lou, *J. Phys. Chem. C*, **2012**, *116*, 6873.

(27) O. Amiri, H. Emadi, S. S. M. Hosseinpour-Mashkani, M. Sabet M. M. Rad, *RSC Adv.*, **2014**, *4*, 10990.

(28) V. Lesnyak, C. George, A. Genovese, M. Prato, A. Casu, S. Ayyappan, A. Scarpellini, L. Manna, *ACS Nano*, **2014**, *8*, 8407.

(29) D.-H. Ha, A. H. Caldwell, M. J. Ward, S. Honrao, K. Mathew, R. Hovden, M. K. A. Koker, D. A. Muller, R. G. Hennig, R. D. Robinson, *Nano Lett.*, **2014**, *14*, 7090.

(30) A. Datta, S. K. Panda, S. Chaudhuri, *J. Solid State Chem.*, **2008**, *181*, 2332.

(31) J. Han, Z. Liu, B. Yadian, Y. Huang, K. Guo, Z. Liu, B. Wang, Y. Li, T. Cui, *J. Power Sources*, **2014**, *268*, 388.

(32) G.-J. Lee, S. Anandan, S. J. Masten, J. J. Wu, *Ind. Eng. Chem. Res.*, **2014**, *53*, 8766.

(33) D. Choi, J.-Y. Pyo, Y. Kim, D.-J. Jang, *J. Mater. Chem. C*, **2015**, *3*, 3286.

(34) Y. Kim, J.-Y. Kim, D.-J. Jang, *J. Phys. Chem. C*, **2012**, *116*, 10296.

(35) Y. Kim, D.-J. Jang, *CrystEngComm*, **2014**, *16*, 6989.

(36) X.-H. Lu, D.-Z. Zheng, J.-Y. Gan, Z.-Q. Liu, C.-L. Liang, P. Liu, Y.-X. Tong, *J. Mater. Chem.*, **2010**, *20*, 7118.

(37) S. Guo, W. Sun, W. Yang, Z. Xu, Q. Li, J. K. Shang, *ACS Appl. Mater. Interfaces*, **2015**, *7*, 26291.

(38) M. Shuai, L. Liao, H. Lu, L. Zhang, J. C. Li, D. Fu, *J. Phys. D: Appl. Phys.*, **2008**, *41*, 135010.

(39) J. M. Wu, *J. Mater. Chem.*, **2011**, *21*, 14048.

(40) M. Ge, H. Liu, *J. Mater. Chem. A*, **2016**, *4*, 16714.

(41) L. De Trizio, L. Manna, *Chem. Rev.*, **2016**, *116*, 10852.

(42) L. Aswaghosh, D. Manoharan, N. V. Jaya, *Phys. Chem. Chem. Phys.*, **2016**, *18*, 5995.

(43) J. Xu, X. Yang, Q.-D. Yang, X. Huang, Y. Tang, W. Zhang, C.-S. Lee, *Chem. Asian J.*, **2015**, *10*, 1490.

(44) Y. Dong, H. Xie, J. Song, M. Xu, Y. Zhao, J. B. Goodenough, *J. Electrochem. Soc.*, **2012**, *159*, A995.

(45) M. Behrens, G. Lolli, N. Muratova, I. Kasatkin, M. Hävecker, R. N. d'Alnoncourt, O. Storcheva, K. Köhler, M. Muhler, R. Schlögl, *Phys. Chem. Chem. Phys.*, **2013**, *15*, 1374.

(46) H. Ye, A. Tang, L. Huang, Y. Wang, C. Yang, Y. Hou, H. Peng, F. Zhang, F. Teng, *Langmuir*, **2013**, *29*, 8728.

(47) G.-J. Lee, S. Anandan, S. J. Masten, J. J. Wu, *Renew. Energy*, **2016**, *89*, 18.

(48) X. Zhao, W. Wang, Y. Zhang, S. Wu, F. Li, J. P. Liu, *Chem. Eng. J.*, **2014**, *250*, 164.

(49) B. N. Patra, D. Majhi, *J. Phys. Chem. B*, **2015**, *119*, 8154.

(50) J. Wu, J. Wang, H. Li, Y. Du, K. Huang, B. Liu, *J. Mater. Chem. A*, **2013**, *1*, 9837.

(51) S. Chen, J. Zhang, C. Zhang, Q. Yue, Y. Li, C. Li, *Desalination*, **2010**, *252*, 149.

(52) K. Shakir, A. F. Elkafrawy, H. F. Ghoneimy, S. G. E. Beheir, M. Refaat, *Water Res.*, **2010**, *44*, 1449.

(53) Y. Guo, J. Zhao, H. Zhang, S. Yang, J. Qi, Z. Wang, H. Xu, *Dyes Pigm.*, **2005**, *66*, 123.

Chapter 4. Highly Efficient Catalytic Performances of Eco-Friendly Grown Silver Nanoshells[†]

[†] This is reproduced from Jaewon Lee and Du-Jeon Jang, *J. Phys. Chem. C*, **2016**, *120*, 4130. © 2016 American Chemical Society.

4.1. Abstract

The catalytic performances, as well as the thickness and the morphologies, of silver nanoshells have been tuned facilely and eco-friendly via laser irradiation. The irradiation of nanosecond laser pulses has transformed silver seeds or nanoparticles adsorbed to the silica surfaces of $Ag@SiO_2$ nanostructures into silver nanoshells, producing $Ag@SiO_2@Ag$ nanostructures having highly enhanced catalytic performances. The catalytic degradation of rhodamine B has been found to occur on silver nanoshells (k_1 process) or on core silver nanospheres (k_2 process); whereas the k_2 value changes hardly, the k_1 value increases largely by chemical reduction and/or laser treatment. Although the k_1 value of a nanocatalyst is smaller than the k_2 value, dye molecules are degraded mostly by the k_1 process because it takes a long induction time for the k_2 reaction to occur. Laser irradiation enhances the catalytic performances of silver-based sandwich nanostructures by lowering the energy barrier (E_a) of the k_1 process, and E_a is reduced by the energetically favorable formation of the activated complex. The increment of catalytic performances resulting from the decrease of E_a has been considered to arise from the surface restructuring process, as well as the coverage increase, of silver nanoshells during laser irradiation.

4.2. Introduction

The design and controlled fabrication of nanostructured materials having functional properties have been extensively investigated.[1-3] In particular, substantial efforts have been devoted to the preparation of noble metallic shells on silica or polystyrene cores because of potential applications in various fields such as catalysis, surface enhanced Raman spectroscopy (SERS), biochemistry, and photonics.[4-11] Of note is that the degree of the surface coverage as well as the metallic coating should be high and uniform for applications in the above fields. Traditionally, surface modification has been explored widely not only to increase the degree of the surface coverage with metals but also to form uniform nanoshells.[4-9] However, this method has some disadvantages as well; metals or compounds such as gold and $SnCl_2$ exploited to activate the core surface can be present as impurities in the final core-shell nanostructure. This process requires additional chemical reagents or a complex experimental apparatus, and diverse toxic reagents are often used and discarded during the synthesis of nanostructures. Therefore, the development of a facile and feasible approach to prepare nanoparticles coated with uniform and complete metal nanoshells still remains to be a great challenge to material scientists. In addition, an environment-friendly manner is highly desired because general synthetic methods often cause substantial environmental problems. A possible approach to develop new metal-based nanostructures is the use of laser pulses to induce the controlled shape transformation of metal nanostructures.[12-18]

Interactions between pulsed laser light and noble metal nanoparticles have been investigated, and possible mechanisms have been also proposed.[19-22] The laser-induced size reduction, as well as the generation and morphology change, of silver or gold nanoparticles in an aqueous solution has been found to take place by irradiation of pulsed laser light, whose power and wavelength can be adjusted readily.[23] It has been reported[20,24] that laser light induces the fragmentation, melting and vaporization of silver nanoparticles having low melting and boiling points compared with bulk metals. It has been also suggested that not only the transformation of small and isolated metal nanoparticles into larger nanostructures but also the production of stable colloidal silver nanoparticles can be experienced by pulsed laser light.[24,25]

Diverse strategies have been established to enhance the catalytic performances of noble metal based-nanocatalysts. Particularly, numerous researchers have investigated the dependence of their catalytic efficiencies on the change of their morphologies, structures, and sizes.[26-29] As an example, El-Sayed et al. have compared the stability and catalytic efficiency of not only various Pt morphologies involving the tetrahedral, spherical, trigonal, cubic nanocatalysts but also diverse structures including the different kinds of Pt/Pd alloy nanostructures in the reduction reaction of 4-nitrophenol to form 4-aminophenol in the presence of $NaBH_4$.[30-31]

Among the various nanostructures, core/shell/shell sandwich nanostructures have received great attention recently as catalysts for the degradation of organic pollutants such as rhodamine B (RhB) and methyl

orange due to their substantially high surface area and enhanced stability.[32] In other words, since the catalytic reaction can take place at both external shell surfaces and inner core surfaces of nanocatalysts, the decomposition of organic pollutants via catalytic oxidation or reduction using sandwich nanostructures is considered to be a highly efficient, green, and low-cost method.

In this report, we present a new and eco-friendly approach for obtaining silver nanoparticles-adsorbed and laser-treated Ag-core/SiO_2-shell ($Ag@SiO_2@Ag_{NPs}$-L) well-defined sandwich nanostructures having highly efficient catalytic performances (Figure 4-1). Silver seeds-adsorbed Ag-core/SiO_2-shell ($Ag@SiO_2@Ag_{seeds}$) nanoparticles have been prepared facilely using a polyol process and the StÖber method.[25,32] As unreacted $Ag(NH_3)^+$ ions are still present in the colloidal solution of $Ag@SiO_2@Ag_{seeds}$ nanoparticles, chemical reduction and laser irradiation have been applied to reduce existing silver ions in the solution, producing silver nanoparticles-adsorbed Ag-core/SiO_2-shell ($Ag@SiO_2@Ag_{NPs}$) or silver seeds-adsorbed and laser-treated Ag-core/SiO_2-shell ($Ag@SiO_2@Ag_{seeds}$-L) nanoparticles, respectively.[25,33] In addition, we have compared the catalytic activity of silver-based sandwich nanostructures fabricated via diverse synthetic methods by monitoring the catalytic reduction rate of RhB in the presence of KBH_4. Laser-treated sandwich nanostructures of $Ag@SiO_2@Ag_{seeds}$-L and $Ag@SiO_2@Ag_{NPs}$-L have exhibited significantly higher catalytic performances than respective pristine nanostructures of $Ag@SiO_2@Ag_{seeds}$ and $Ag@SiO_2@Ag_{NPs}$. It has been found that laser irradiation enhances the catalytic activities of silver-based sandwich

nanocatalyts by lowering the energy barrier via the surface restructuring and the coverage increase of silver nanoshells.[12,13,25,34] It is noteworthy that we have expanded our previous communication work[25] extensively to have a deep insight on the catalytic reaction mechanism of RhB taking place on the surfaces of silver nanoshells by additionally observing activation energies and frequency factors from Arrhenius plots, activation enthalpies and activation entropies from Eyring plots, and isokinetic temperatures from compensation law plots, in particular.

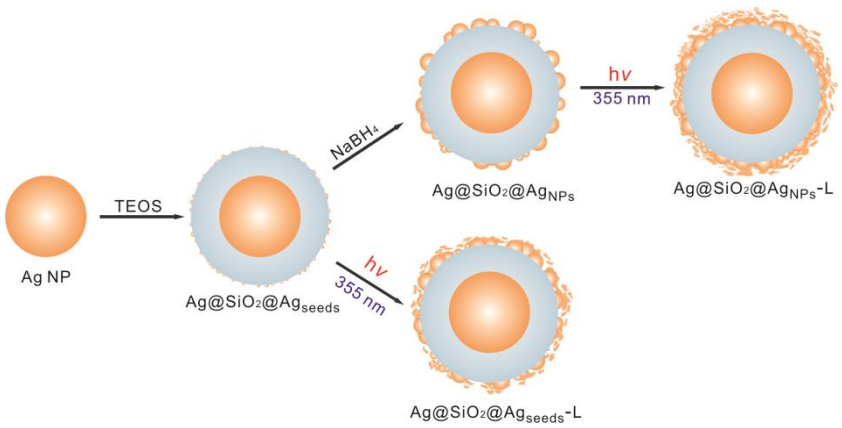

Figure 4-1. Schematic illustration of processes to produce Ag@SiO_2@Ag sandwich nanostructures. The orange indicates silver while the blue indicates silica.

4.3. Experimental Details

Ag@SiO_2@Ag Nanostructures. The detailed synthetic procedures of Ag@SiO_2@Ag_{seeds} nanoparticles have already been reported.[25] For the fabrication of Ag@SiO_2@Ag_{NPs} nanoparticles, 9.4 mL of the colloidal solution of silver nanoparticles was added into a mixture containing 25 mL of ethanol, 4.0 mL of deionized water, 70 μL of TEOS, and 4.0 mL of ammonia water under vigorous stirring. After being stirred for 1 h, the reaction mixture was added with 1.0 mL of 20 mM $NaBH_4$(aq) and stirred vigorously for 1 h to produce Ag@SiO_2@Ag_{NPs} nanoparticles. Then, the resulting product was centrifuged, washed with ethanol several times, and dispersed in 40 mL of ethanol to produce the ethanol colloidal solution of Ag@SiO_2@Ag_{NPs} nanoparticles.[33] For the preparation of Ag@SiO_2@Ag_{seeds}-L and Ag@SiO_2@Ag_{NPs}-L nanoparticles, nanosecond laser pulses of 355 nm having an average energy of 5.0 mJ from a Q-switched Quantel Brilliant Nd:YAG laser of 6 ns were irradiated at fluence of 5.3 mJ/cm^2 with a spot diameter of 11 mm to 3.0 mL of the colloidal solutions of Ag@SiO_2@Ag_{seeds} and Ag@SiO_2@Ag_{NPs} nanoparticles contained in quartz cells having a path length of 10 mm and stirred vigorously for 30 min to produce Ag@SiO_2@Ag_{seeds}-L and Ag@SiO_2@Ag_{NPs}-L nanoparticles, respectively. Then, the resulting colloids were centrifuged, washed with ethanol several times, and dispersed in 3.0 mL of ethanol to produce the ethanol colloidal solutions of Ag@SiO_2@Ag_{seeds}-L and Ag@SiO_2@Ag_{NPs}-L nanoparticles, respectively.[13]

Catalytic Performances. The catalytic performances of nanoparticles were tested for the degradation reaction of rhodamine B (RhB) in the presence of 1.1 mM KBH_4. 0.10 mL of an ethanol colloidal solution was added into 2.0 mL of 20 μM RhB(aq) and 1.0 mL of water contained in a cell, and then 0.40 mL of 10 mM KBH_4(aq) was added rapidly. The absorption spectral changes of RhB were measured at scheduled intervals, and the catalytic activity of nanoparticles was evaluated by monitoring the optical density of RhB. To study the reusability of $Ag@SiO_2@Ag_{NPs}$-L nanocatalysts, used nanoparticles were separated from the reaction mixture by centrifugation at 13000 rpm for 10 min, rinsed with water, and dispersed into 1.1 mL of water. The colloidal solution of recovered nanocatalysts was then added into a mixture containing new reactant molecules to initiate another reaction cycle.

Characterization. Transmission electron microscopy (TEM) images were taken with a Hitachi H-7600 microscope, while scanning transmission electron microscopy (STEM) images and Energy-dispersive X-ray (EDX) elemental profiles were measured using a JEOL JEM-2100F microscope. UV-visible absorption spectra were recorded by using a Scinco S-3000 spectrophotometer.

4.4. Results and Discussion

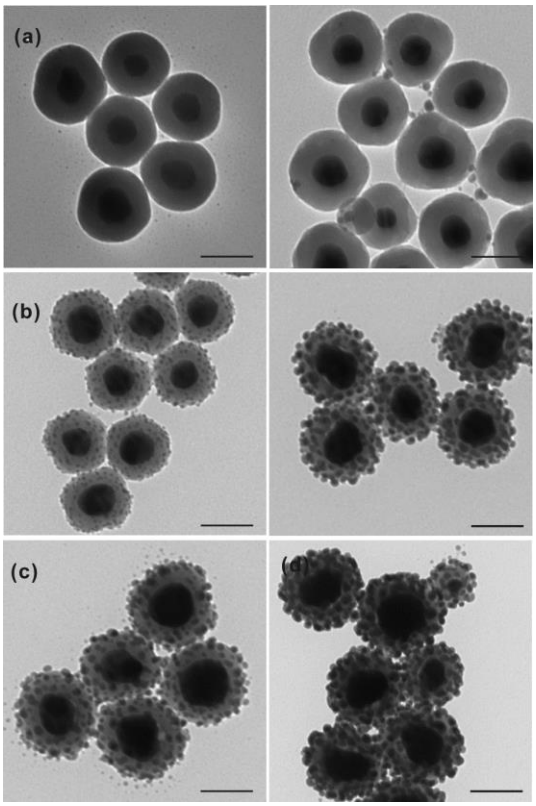

Figure 4-2. TEM images of (a) $Ag@SiO_2$, (b) $Ag@SiO_2@Ag_{seeds}$, and (c) $Ag@SiO_2@Ag_{NPs}$ nanostructures (left) before and (right) after irradiation with 355 nm pulses of 6 ns for 30 min. Each scale bar indicates 100 nm.

Figure 4-2 shows that the average diameter of core silver nanospheres (70 nm) and the average thickness of silica shells (34 nm) for $Ag@SiO_2$, $Ag@SiO_2@Ag_{seeds}$, and $Ag@SiO_2@Ag_{NPs}$ nanostructures have remained almost invariant during irradiation of laser pulses for 30 min. Although silver nanoshells have not grown at all on the silica surfaces of $Ag@SiO_2$ nanostructures by irradiation of laser pulses for 30 min (Figure 4-2a), the

average diameter of the silver seeds (4 nm) of $Ag@SiO_2@Ag_{seeds}$ nanostructures has become as long as 15 nm (Figure 4-2b) and the average diameter of the silver nanoparticles (15 nm) of $Ag@SiO_2@Ag_{NPs}$ nanostructures has increased as 20 nm (Figure 4-2c).[33-37] Thus, considering the TEM images, the growth of silver nanoparticles on silica shells upon laser irradiation to an aqueous colloidal solution containing silver ions has been attributed to the photolysis of water and the subsequent reduction of silver ions. Silver atoms generated by the photolysis of water can grow through the addition of either silver atoms or silver ions followed by reduction. Silver atoms are attached to colloidal silver clusters or silver seeds on the silica surfaces under stirring vigorously, resulting in the growth of silver nanoshells.[10,25] It is suggested that the colloidal silver clusters adsorb finally to silver nanoparticles on silver nanoshells, transforming $Ag@SiO_2@Ag_{seeds}$, and $Ag@SiO_2@Ag_{NPs}$ nanostructures into $Ag@SiO_2@Ag_{seeds}$, and $Ag@SiO_2@Ag_{NPs}$ nanostructures, respectively, via laser irradiation for 30 min. Additionally, the EDX analysis spectra indicate that the molar percentage of silver has considerably increased from 55.6% in $Ag@SiO_2@Ag_{NPs}$ to 68.3% in $Ag@SiO_2@Ag_{NPs}$-L, also supporting that silver nanoshells can grow eco-friendly via irradiating laser pulses only in the absence of any reducing agents.

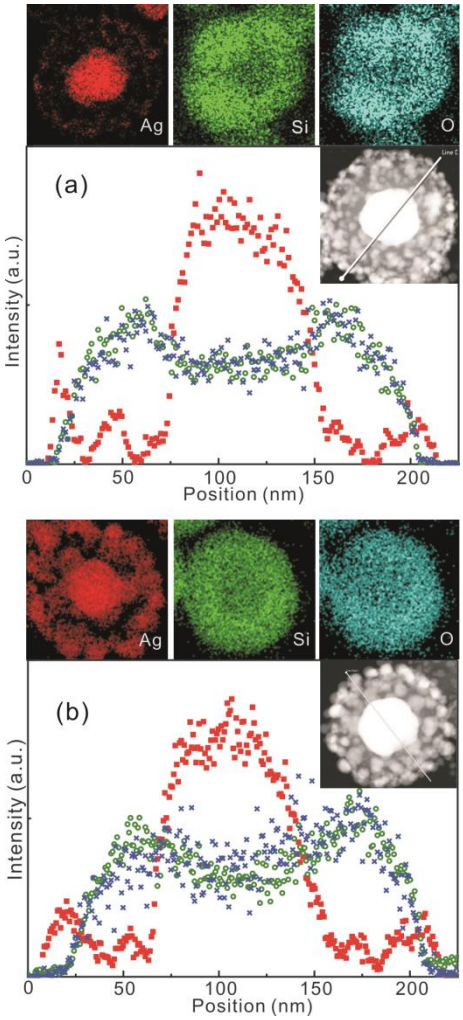

Figure 4-3. EDX elemental maps and area-normalized line-scanned elemental intensity profiles of a $Ag@SiO_2@Ag_{NPs}$ nanostructure (a) before and (b) after irradiation with 355 nm for 30 min for (red) Ag, (green) Si, and (blue) O along the indicated lines of the insetted STEM images. Note that the actual particle transformed into the particle in (b) is different from the particle in (a).

Line-scanned EDX elemental profiles have been measured to confirm the exact structures and compositions of $Ag@SiO_2@Ag_{NPs}$ (Figure 4-3a) and $Ag@SiO_2@Ag_{NPs}$-L nanostructures (Figure 4-3b), revealing that both sandwich

nanostructures consisting of silver and silica compositely are passivated well with largely grown silver nanoparticles. Furthermore, Figure 4-3 displays that silver nanoparticles adsorbed on the silica shell of a $Ag@SiO_2@Ag_{NPs}$ nanostructure have grown up to larger silver nanoparticles in 30 min of laser irradiation, forming the silver shell of a $Ag@SiO_2@Ag_{NPs}$-L sandwich nanostructure without deteriorating the silica shell. The insetted STEM images also support the above descriptions well. In particular, the elemental maps of silver present that silver density is much higher on the silica surface of the $Ag@SiO_2@Ag_{NPs}$-L nanostructure than on the silica surface of the pristine $Ag@SiO_2@Ag_{NPs}$ nanostructure, suggesting as well that well-defined $Ag@SiO_2@Ag_{NPs}$-L sandwich nanostructures having high catalytic activity and reusability (see below) can be fabricated readily by irradiating laser pulses to $Ag@SiO_2@Ag_{NPs}$ nanosturctures.

The surface-plasmon resonance spectra of $Ag@SiO_2@Ag_{seeds}$ (Figure 4-4a) and $Ag@SiO_2@Ag_{NPs}$ (Figure 4-4b) shift largely to the red with extensive broadening via laser irradiation for 30 min, indicating that the irradiation of 355 nm pulses to an aqueous colloidal solution containing silver ions has grown silver nanoshells eco-friendly in the absence of any reducing agents, as already described. However, the surface-plasmon absorption band of $Ag@SiO_2$ nanostructures at 460±129 nm has been blue-shifted by 5 nm and narrowed by 10 nm, suggesting that the irradiation of laser pulses to an aqueous colloidal solution containing no silver ions has transformed core silver nanoparticles into more spherical silver nanoparticles owing to the photothermal annealing effect

of excitation laser pulses without producing silver nanoparticles on silica surfaces.[19-22]

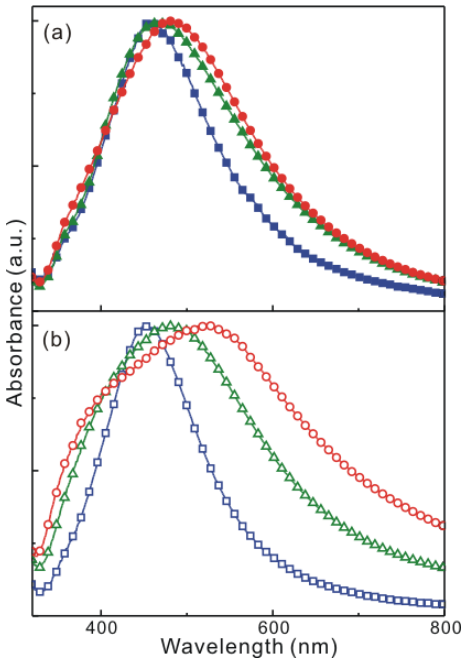

Figure 4-4. Maximum-normalized surface-plasmon resonance spectra of (blue) $Ag@SiO_2$, (green) $Ag@SiO_2@Ag_{seeds}$, and (red) $Ag@SiO_2@Ag_{NPs}$ nanostructures (a) before and (b) after irradiation with 355 nm pulses of 6 ns for 30 min.

During the irradiation of laser pulses to $Ag@SiO_2@Ag_{seeds}$ nanostructures, the surface-plasmon resonance spectrum of silver nanoparticles at 473±167 nm has shifted to the red by 12 nm and its full width at the half maximum has increased by 29 nm. The sizes and coverages of silver seeds on silica surfaces have increased by laser irradiation to give rise to the red shift and broadening of the surface-plasmon resonances of silver. Furthermore, laser irradiation has made the surface-plasmon absorption spectrum of $Ag@SiO_2@Ag_{NPs}$ nanostructures

at 486±183 nm red-shifted by 30 nm and broadened by 72 nm.[9] We consider that enhanced coupling plasmon interactions among silver nanoparticles grown largely on silica shells during laser irradiation have resulted in the extensive widening and red shift of the absorption spectrum.[25,38-43] Thus, Figure 4-4 indicates that laser irradiation to a colloidal solution containing silver ions has grown silver nanoshells on silica surfaces facilely in the absence of any reducing agents.

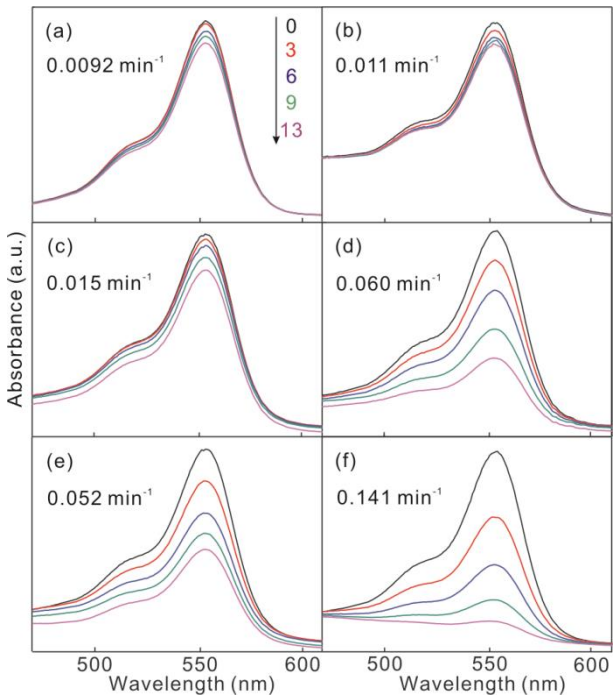

Figure 4-5. Absorption spectra at 30 ºC of KBH_4-added aqueous RhB solutions, measured at elapsed times indicated in the units of min after adding aqueous colloidal solutions of (a) $Ag@SiO_2$, (b) $Ag@SiO_2$-L, (c) $Ag@SiO_2@Ag_{seeds}$, (d) $Ag@SiO_2@Ag_{seeds}$-L (e) $Ag@SiO_2@Ag_{NPs}$, and (f) $Ag@SiO_2@Ag_{NPs}$-L nanoparticles.

We have evaluated the catalytic properties of the prepared silver-based nanocatalysts by monitoring the time-dependent absorbance changes of RhB solutions containing KBH_4 (Figure 4-5), revealing that the catalytic performances of $Ag@SiO_2@Ag_{NPs}$-L nanostructures are much more efficient than those of any other silver-based nanocatalysts at the same concentration of precursor $AgNO_3$ owing to the largest sizes and the highest coverages of silver nanoparticles on silica surfaces.[12,13,25,44] Note that although KBH_4 is a strong reducing agent, RhB hardly decomposes in the absence of silver-based nanocatalysts.[4,12] Upon irradiation with laser pulses for 30 min, although the catalytic rate constant of $Ag@SiO_2$ nanosturctures has remained almost invariant, the catalytic rate constants of $Ag@SiO_2@Ag_{seeds}$ and $Ag@SiO_2@Ag_{NPs}$ have increased largely by factors of 4.0 and 2.7, respectively.

The temperature-dependent first-order degradation kinetic profiles of RhB catalyzed via silver-based nanocatalysts in the presence of KBH_4 in Figure 4-6 have been exploited to extract the degradation rate constants (k_1 and k_2) and the induction times (t_0) of Table 1; $\ln(A/A_0) = -k_1 t$ {when $t \leq t_0/(k_2 - k_1)$} or $-k_2(t - t_0)$ {when $t > t_0/(k_2 - k_1)$}, where t is the reaction time and A (A_0) is the optical density at 554 nm of RhB at the time t (0). Whereas k_1 is the degradation rate constant of RhB catalyzed by the outer surfaces of silver-based nanocatalysts, k_2 is the rate constant catalyzed by their core silver nanospheres and t_o is the induction time, a certain period required before the k_2 catalytic reaction is initiated. As observed in a number of systems,[12,34] the induction time is ascribed

to the diffusion time required for reactants to be adsorbed onto the surfaces of core silver nanospheres before the catalytic reaction starts.

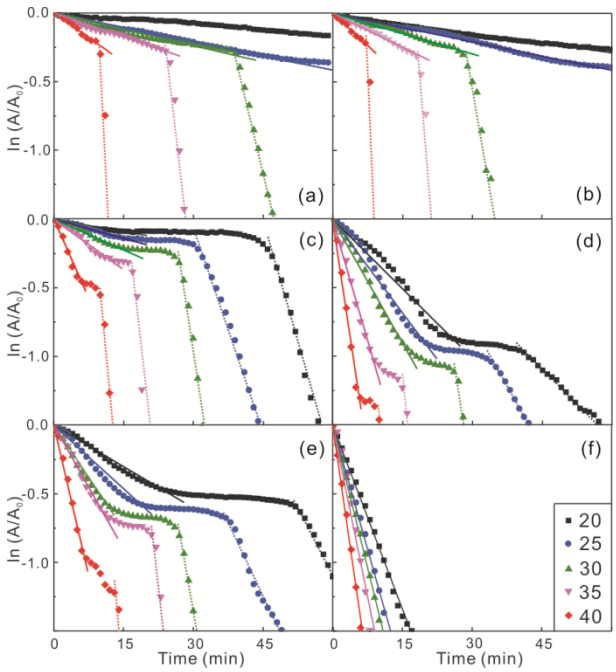

Figure 4-6. ln(A/A_0) vs. t for the catalytic degradation of 11 μM RhB(aq) in the presence of 1.1 mM KBH_4 at temperatures indicated in the units of ^oC via nanocatalysts of (a) $Ag@SiO_2$, (b) $Ag@SiO_2$-L, (c) $Ag@SiO_2@Ag_{seeds}$, (d) $Ag@SiO_2@Ag_{seeds}$-L, (e) $Ag@SiO_2@Ag_{NPs}$, and (f) $Ag@SiO_2@Ag_{NPs}$-L.

Table 4-1 indicates that the k_1 values of $Ag@SiO_2@Ag_{seeds}$ and $Ag@SiO_2@Ag_{NPs}$ nanocatalysts have increased largely by laser irradiation. Table 4-1 also suggests that the k_2 values, the rate constants catalyzed by core silver nanospheres, have changed scarcely by chemical reduction or laser irradiation. This indicates that the structures of the core silver nanospheres of silver-based nanocatalysts have been hardly affected by the chemical or laser

reduction of silver ions present in colloidal solutions. It is noteworthy that although the k_1 value of a nanocatalyst is much smaller than the k_2 value of the same nanocatalyst, RhB has been degraded mostly by the k_1 catalytic reaction for sandwich nanocatalysts having well-grown silver nanoshells on silica surfaces because it has taken the induction time of t_0 for the k_2 reaction to occur. In particular, the k_2 value of $Ag@SiO_2@Ag_{NPs}$-L could not be observed at all as the degradation of RhB was already completed within the induction time of the k_2 reaction. Thus, Figure 4-6 and Table 4-1 have shown that the major catalytic degradation mechanism of RhB switches from the k_2 process to the k_1 process as silver nanoshells grow well on silica surfaces via chemical reduction and/or laser irradiation.

Table 4-1. Rate Constants (k) and Induction Times (t_o) at 30 °C, Activation Energies (E_a), Frequency Factors (A), Activation Enthalpies ($\Delta H^{\ddagger}$), and Activation Entropies ($\Delta S^{\ddagger}$) for the Catalytic Degradation of Rhodamine B via Silver-Based Nanocatalysts in the Presence of KBH_4.

Catalysts	k_1[a] (k_2[b]) [min^{-1}]	(t_o) [min]	E_{a1} (E_{a2}) [kcal mol^{-1}]	A_1 (A_2) [min^{-1}]	$\Delta H_1^{\ddagger}$ ($\Delta H_2^{\ddagger}$) [kcal mol^{-1}]	$\Delta S_1^{\ddagger}$ ($\Delta S_2^{\ddagger}$) [cal mol^{-1} K^{-1}]
$Ag@SiO_2$	0.0149	(25.6)	20.5	6.59×10^{12}	17.3	-10.5
$@Ag_{seeds}$	(0.216)		(11.7)	(5.00×10^{7})	(11.1)	(-25.3)
$Ag@SiO_2$	0.0602	(21.2)	15.5	9.70×10^{9}	14.1	-17.3
$@Ag_{seeds}$-L	(0.222)		(22.8)	(3.79×10^{15})	(16.7)	(-7.6)
$Ag@SiO_2$	0.0496	(23.0)	16.9	6.38×10^{10}	15.6	-13.2
$@Ag_{NPs}$	(0.186)		(18.1)	(1.76×10^{12})	(15.0)	(-12.9)
$Ag@SiO_2$	0.141	(–)	9.0 (–)	6.16×10^{5}	9.0	-31.5
$@Ag_{NPs}$-L	(–[c])			(–)	(–)	(–)

[a] 0.0080 min^{-1} for $Ag@SiO_2$ and 0.0099 min^{-1} for $Ag@SiO_2$-L. [b] 0.147 min^{-1} for $Ag@SiO_2$ and 0.199 min^{-1} for $Ag@SiO_2$-L. [c] Not observed.

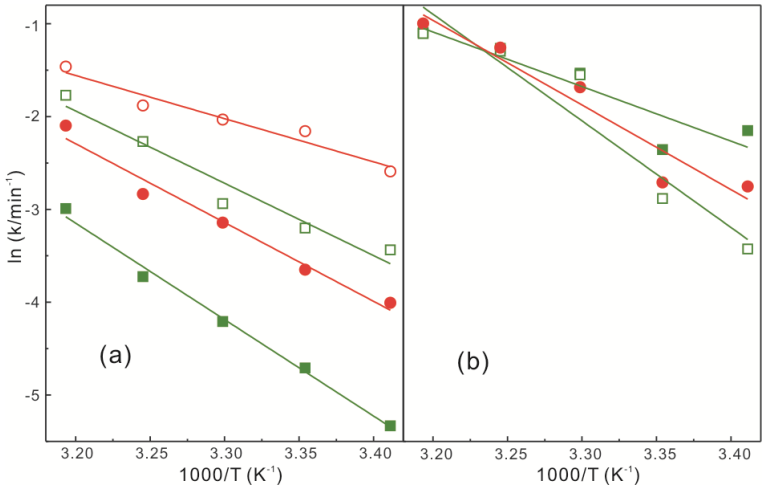

Figure 4-7. Arrhenius plots for (a) the k_1 and (b) the k_2 catalytic-degradation rate constants of 11 μM RhB(aq) in the presence of 1.1 mM KBH_4 via nanocatalysts of (closed squares) $Ag@SiO_2@Ag_{seeds}$, (open squares) $Ag@SiO_2@Ag_{seeds}$-L, (closed circles) $Ag@SiO_2@Ag_{NPs}$, and (open circles) $Ag@SiO_2@Ag_{NPs}$-L.

Figure 4-7a and Table 4-1 present that the activation energy (E_{a1}) and the frequency factor (A_1) of the k_1 process via $Ag@SiO_2@Ag_{seeds}$-L are substantially smaller than the respective ones via $Ag@SiO_2@Ag_{seeds}$. Table 4-1 also indicates that the E_{a1} and A_1 values of the k_1 process via $Ag@SiO_2@Ag_{NPs}$-L are much smaller than the respective ones via $Ag@SiO_2@Ag_{NPs}$, suggesting that laser irradiation to a colloidal solution containing silver ions enhances the catalytic performances of silver-based nanostructures largely by lowering the energy barrier of the k_1 degradation reaction of RhB catalyzed by the outer surfaces of silver-based nanocatalyts, rather than by increasing the frequency factor (A_1) of the reaction. As discussed with Figure 4-2-4, laser irradiation grows silver shells on silica surfaces to adsorb reactants facilely and to promote

rapid electron relays from BH_4^- to RhB, lowering the energy barrier of the catalytic reaction. The E_{a1} and A_1 values via $Ag@SiO_2@Ag_{NPs}$ are also smaller than the respective ones via $Ag@SiO_2@Ag_{seeds}$, suggesting that the growth of silver shells on silica surfaces by chemical reduction increases the catalytic performances of silver-based sandwich nanostructures by decreasing the activation energy (E_{a1}) of the k_1 process as well. It is noteworthy that the catalytic performances of silver-based nanocatalysts have been enhanced more efficiently by laser irradiation than by chemical reduction. This suggests that laser irradiation induces not only the growth but also the surface restructuring of silver shells. It has been reported[12,34] that surface atom restructuring by photothermal annealing during laser irradiation renders metallic surfaces to adsorb reactants facilely and to lower the energy barrier of the catalytic reaction. Nevertheless, Figure 4-7 and Table 4-1 have shown that the catalytic performances of $Ag@SiO_2@Ag_{seeds}$ nanostructures have been enhanced most efficiently by lowering the energy barrier of the k_1 process most effectively via chemical reduction and subsequent laser treatment. On the other hand, Figure 4-7b and Table 4-1 display that both the activation energy (E_{a2}) and the frequency factor (A_2) of the k_2 process occurring on the core silver nanospheres increase largely by laser irradiation or chemical reduction.

Figure 4-8 shows plots of frequency factors versus activation energies for the degradation of RhB catalyzed with different silver-based nanocatalysts; good linear compensation relations are found to exist for both k_1 and k_2 processes. The following empirical relationship has been known to hold between the

frequency factor (A) and the activation energy (E_a): $\ln A = \alpha + E_a/(RT_\theta)$ where α is a constant and T_θ is called the fictitious isokinetic temperature, where the catalytic rates of all the nanocatalyts become equal.[46,47] In our experiments, T_θ has been found to be 346 K for the k_1 process and 309 K for the k_2 process, suggesting that the isokinetic temperature of the k_2 process is lower by 37 K than that of the k_1 process because the k_2 process takes place on the surfaces of well-defined core silver nanospheres. Figure 4-8a also suggests that for the k_1 reaction of RhB catalyzed by the outer surfaces of silver-based nanocatalyts, laser-treated nanostructures have smaller concentrations of active sites where the reaction requires smaller E_a. On the other hand, Figure C-8b indicates that for the k_2 process occurring on core silver nanospheres, laser irradiation increases the concentration of active sites where the reaction requires larger E_a.[12,27,34] Nonetheless, Figure 4-8 implies that laser treatment has reduced the activation energy of RhB degradation catalyzed by silver nanoshells extensively, enhancing the catalytic performances of Ag@SiO_2@Ag nanocatalysts on large scales.

The enthalpy ($\Delta H^\ddagger$) and the entropy ($\Delta S^\ddagger$) of activation can be obtained from the slope and the intercept, respectively, of the Eyring plot: $\ln (k/T) = -(\Delta H^\ddagger/R)(1/T) + \Delta S^\ddagger/R + \ln (k_B/h)$.[4,12,34] Table 4-1 indicate that laser irradiation has significantly decreased not only $\Delta H_1^\ddagger$ but also $\Delta S_1^\ddagger$, suggesting that the laser treatment of silver-based nanocatalysts makes the formation of the activated complex for the k_1 catalytic degradation reaction of RhB favorable in energy but unfavorable in degree of freedom. On the other hand, Table 4-1 reveals that

$\Delta H_2^{\ddagger}$, as well as $\Delta S_2^{\ddagger}$, has been increased largely by laser irradiation. This also supports that laser treatment makes the formation of the activated complex for the k_2 catalytic degradation of RhB energetically highly unfavorable because reactant molecules have to diffuse through silver nanoshells grown well by laser irradiation.

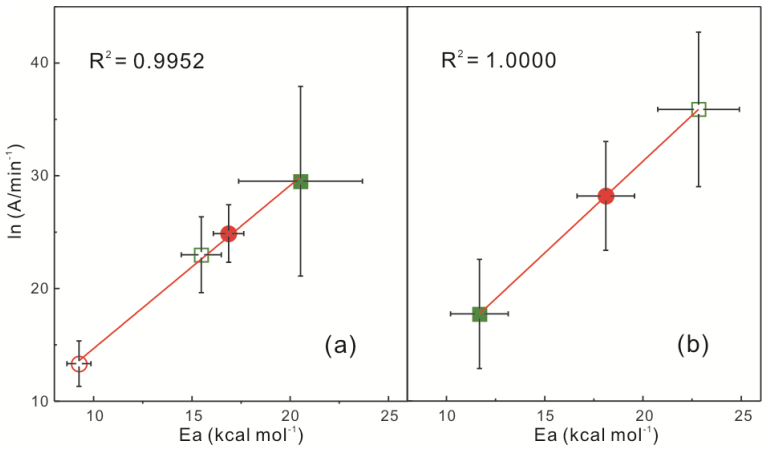

Figure 4-8. Compensation law plots for (a) the k_1 and (b) the k_2 catalytic-degradation rate constants of (closed squares) Ag@SiO_2@Ag_{seeds}, (open squares) Ag@SiO_2@Ag_{seeds}-L, (closed circles) Ag@SiO_2@Ag_{NPs}, and (open circles) Ag@SiO_2@Ag_{NPs}-L.

We have measured the reusability of Ag@SiO_2@Ag_{NPs}-L nanocatalysts by repeating catalytic experiments, where experimental conditions were held constant.[26,34] Catalysis recycle experiments have been performed five times, and nanocatalysts were separated by centrifugation and reused for consecutive catalysis reactions. The reusability of nanocatalysts shown in Figure 4-9 indicates that Ag@SiO_2@Ag_{NPs}-L nanostructures maintain similar catalytic performances even after five successive cycles of the degradation reaction.

These results demonstrate well that silver nanoshells can efficiently protect silver-based sandwich nanostructures from aggregation and dissolution during catalytic reactions.

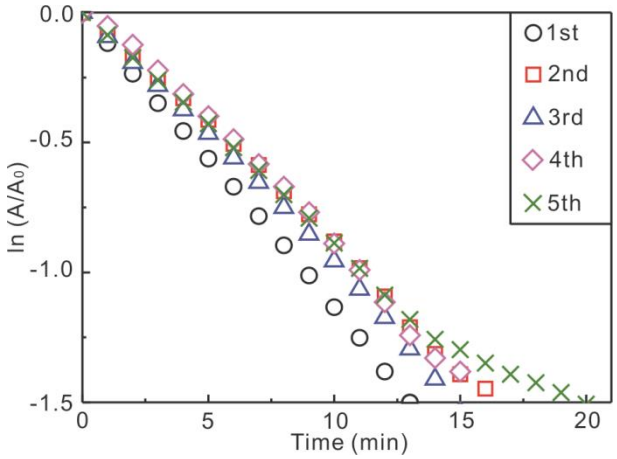

Figure 4-9. First-order kinetics, ln(A/A_0) vs. t, for the catalytic degradation of 11 μM RhB(aq) via Ag@SiO_2@Ag_{NPs}-L nanostructures in the presence of 1.1 mM KBH_4 at 30 ˚C, for five indicated recycles.

The catalytic reduction mechanism of RhB via silver-based nanocatalysts in the presence of BH_4^- has already been reported.[48-52] Briefly, the silver-based nanocatalysts facilitate electron transfer from BH_4^- to RhB through their catalytic surfaces. Thus, the silver-based nanocatalysts serve as electron relays for the degradation reaction of RhB in the presence of KBH_4. With Figure 4-5-7, we have verified that laser irradiation increases the catalytic activity of silver-based nanocatalysts largely by lowering E_{a1} substantially. In addition, we have shown that the formation enthalpy ($\Delta H_1^{\ddagger}$) of the activated complex for the catalytic degradation reaction of RhB has larger negative values on laser-treated Ag@SiO_2@Ag nanostructures than on pristine ones. Because heterogeneous

catalysis is primarily associated with the chemisorption of reactant molecules that depends on the structure of nanocatalysts, to understand the increment of the catalytic activity of $Ag@SiO_2@Ag$ nanostructures by laser treatment, we should consider the surface restructuring process and the coverage increase of silver nanoshells on silica surfaces during laser irradiation. The thermally induced melting of silver nanoshells has been known to begin at their surfaces, enabling surfaces atoms to get mobility.[48] Furthermore, the diffusion of atoms on the surfaces becomes much faster above $0.3T_{melting}$.[48] Thus, we suggest that a restructuring of surface atoms by laser irradiation enhances the metallic surfaces of $Ag@SiO_2@Ag$ nanostructures to chemisorb reactant molecules readily and to facilitate electron relays from BH_4^- to RhB highly, promoting the catalytic performances of silver-based sandwich nanocatalyts enormously.[12,25,34]

4.5. Conclusion

The irradiation of 355 nm nanosecond laser pulses for 30 min has transformed silver seeds or nanoparticles adsorbed to the silica surfaces of $Ag@SiO_2$ nanostructures into silver nanoshells, producing $Ag@SiO_2@Ag$ nanostructures having highly enhanced catalytic performances. The catalytic activity of the sandwich nanostructures on the degradation reaction of rhodamine B (RhB) in the presence of KBH_4 has been tuned readily by

adjusting the silver-shell thickness, morphology, and composition of the silver-based nanocatalysts via chemical reduction and/or laser irradiation. The catalytic reaction has been found to occur on silver nanoshells (k_1 process) or on core silver nanospheres (k_2 process); whereas the k_2 value changes hardly, the k_1 value increases largely by chemical reduction and/or laser treatment. Although the k_1 value of a nanocatalyst is much smaller than the k_2 value, RhB is degraded mostly by the k_1 process when the nanocatalyst has a well-grown silver nanoshell because it takes a long induction time of ~20 min for the k_2 reaction to occur. Laser irradiation enhances the catalytic performances of silver-based sandwich nanostructures by lowering the energy barrier (E_a) of the k_1 process occurring on the silver nanoshells. The energetically favorable formation of the activated complex (that is $\Delta H^{\ddagger}$ decrease) has been attributed to reduce the activation energy. The increment of catalytic performances resulting from the decrease of E_a and $\Delta H^{\ddagger}$ has been considered to arise from the surface restructuring process, as well as the coverage increase, of silver nanoshells on silica surfaces during laser irradiation. The laser-induced growth of well-defined silver nanoshells also increases the reusability of silver-based nanocatalysts by preventing aggregation and dissolution. Overall, laser treatment can be considered to be a new, facile, and eco-friendly approach to enhance the catalytic performances of silver-based sandwich nanostructures highly.

4.6. Acknowledgements

This work was supported by research grants through the National Research Foundation (NRF) of Korea funded by the Korean government (2014-057382 and 2015-5051798).

4.7. References

(1) Y. Kim, S. J. Kim, S.-P. Cho, B. H. Hong, D.-J. Jang, *Sci. Rep.*, **2015**, *5*, 12345.

(2) H.-B. Kim, H.-J. Kim, W. I. Lee, D.-J. Jang, *J. Mater. Chem. A*, **2015**, *3*, 9714.

(3) Y. Kim, H.-B. Kim, D.-J. Jang, *J. Mater. Chem. A*, **2014**, *2*, 5791.

(4) J.-A. Kwak, D. K. Lee, D.-J. Jang, *Appl. Catal. B: Environ.*, **2013**, *142*, 323.

(5) H. H. Park, K. Woo, J.-P. Ahn, *Sci. Rep.*, **2013**, *3*, 1497.

(6) K. Wang, X. Zhang, C. Niu, Y. Wang, *ACS Appl. Mater. Interfaces*, **2014**, *6*, 1272.

(7) J. Zhang, J. Liu, S. Wang, P. Zhan, Z. Wang, N. Ming, *Adv. Funct. Mater.*, **2004**, *14*, 1089.

(8) Z. Deng, H. Zhu, B. Peng, H. Chen, Y. Sun, X. Gang, P. Jin, J. Wang, *ACS Appl. Mater. Interfaces*, **2012**, *4*, 5625.

(9) A. M. Brito-Silva, R. G. Sobral-Filho, R. Babosa-Silva, C. B. de Araujo, A. Galembeck, A. G. Brolo, *Langmuir*, **2013**, *29*, 4366.

(10) W. Wang, S. A. Asher, *J. Am. Chem. Soc*., **2001**, *123*, 12528.

(11) W. Shi, Y. Sahoo, M. T. Swihart, P. N. Prasad, *Langmuir*, **2005**, *21*, 1610.

(12) H. Lee, J.-A. Kwak, D.-J. Jang, *J. Phys. Chem. C*, **2015**, *118*, 22792.

(13) M. R. Kim, J.-Y. Kim, S. J. Kim, D.-J. Jang, *Appl. Catal. A: General*, **2011**, *393*, 317.

(14) D. Werner, S. Hashimoto, T. Uwada, *Langmuir*, **2010**, *26*, 9956.

(15) R. Jin, Y. C. Cao, E. Hao, G. S. Metraux, G. C. Schatz, C. A. Mirkin, *Nature*, **2003**, *425*, 487.

(16) R. Jin, Y. Cao, C. A. Mirkin, K. L. Kelly, G. C. Schatz, J. G. Zheng, *Science*, **2001**, *294*, 1901.

(17) S. Inasawa, M. Sugiyama, Y. Yamaguchi, *J. Phys. Chem. B*, **2005**, *109*, 3104.

(18) H. Zeng, X.-W. Du, S. C. Singh, S. A. Kulinich, S. Yang, J. He, W. Cai, *Adv. Funct. Mater.*, **2012**, *22*, 1333.

(19) C. M. Aguirre, C. E. Moran, J. F. Young, N. J. Halas, *J. Phys. Chem. B*, **2004**, *108*, 7040.

(20) P. V. Kamat, M. Flumiani, G. V. Hartland, *J. Phys. Chem. B*, **1998**, *102*, 3123.

(21) A. Takami, H. Kurita, S. Koda, *J. Phys. Chem. B*, **1999**, *103*, 1226.

(22) D. Werner, S. Hashimoto, *Langmuir*, **2013**, *29*, 1295.

(23) A. Callegari, D. Tonti, M. Chergui, *Nano Lett.*, **2003**, *3*, 1565.

(24) P. V. Kamat, *J. Phys. Chem. B*, **2002**, *106*, 7729.

(25) J. Lee, D.-J. Jang, *RSC Adv.*, **2015**, *5*, 64268.

(26) J. Lee, K. Han, D.-J. Jang, *Appl. Catal. A: General*, **2014**, *469*, 380.

(27) J. Zeng, Q. Zhang, J. Chen, Y. Xia, *Nano Lett.*, **2010**, *10*, 30.

(28) H. Wei, C. Gomez, J. Liu, N. Guo, T. Wu, R. Lobo-Lapidus, C. L. Marshall, J. T. Miller, R. J. Meyer, *J. Catal.*, **2013**, *298*, 18.

(29) N. R. Jana, T. K. Sau, T. Pal, *J. Phys. Chem. B*, **1999**, *103*, 115.

(30) M. A. Mahmoud, F. Saira, M. A. El-Sayed, *Nano Lett.*, **2010**, *10*, 3764.

(31) R. Narayanan, M. A. El-Sayed, *Nano Lett.*, **2004**, *4*, 1343.

(32) C. Li, J. Mei, S. Li, N. Lu, L. Wang, B. Chen, W. Dong, *Nanotechnology*, **2010**, *21*, 245602

(33) Y. Li, Y. Wu, Y. Gao, S. Sha, J. Hao, G. Cao, C. Yang, *RSC Adv*., **2013**, *3*, 26361.

(34) M. Son, J. Lee, D.-J. Jang, *J. Mol. Catal. A: Chem.*, **2014**, *385*, 38.

(35) G. Guisbiers, G. Abudukelimu, D. Hourlier, *Nanoscale Res. Lett.*, **2011**, *6*, 396.

(36) K. Dick, T. Dhanasekaran, Z. Zhang, D. Meisel, *J. Am. Chem. Soc.*, **2002**, *124*, 2312.

(37) D. L. Van Hyning, C. F. Zukoski, *Langmuir*, **1998**, *14*, 7034.

(38) P. K. Jain, M. A. El-Sayed, *J. Phys, Chem. Lett.*, **2007**, *111*, 17451.

(39) G. Rong, H. Wang, L. R. Skewis, B. M. Reinhard, *Nano Lett.*, **2008**, *8*, 3386.

(40) P. K. Jain, M. A. El-Sayed, *Nano Lett.*, **2008**, *8*, 4347.

(41) K. E. Peceros, X. Xu, S. R. Bulock, M. B. Cortie, *J. Phys. Chem. B*, **2005**, *109*, 21516.

(42) E. Prodan, C. Radloff, N. J. Halas, P. Nordlander, *Science*, **2003**, *302*, 419.

(43) S. Yun, S. Hong, J. I. Acapulco, H. Y. Jang, S. Ham, K. Lee, S. K. Kim, S. Park, *Chem. Eur. J.*, **2015**, *21*, 6165.

(44) S. Panigrahi, S. Basu, S. Praharaj, S. Pande, S. Jana, A. Pal, S. K. Ghosh, T. Pal, *J. Phys. Chem. C*, **2007**, *111*, 4596.

(45) Z.-J. Jiang, C.-Y. Liu, L.-W. Sun, *J. Phys. Chem. B*, **2005**, *109*, 1730.

(46) G. A. Somorjai, Introduction to Surface Chemistry and Catalysis; John Wiley & Sonc Inc: New York, **1994**.

(47) T. Bligaard, K. Honkala, A. Logadottir, J. K. Norkov, *J. Phys. Chem. B*, **2003**, *107*, 9325.

(48) S. Wunder, F. Polzer, Y. Lu, Y. Mei, M. Ballauff, *J. Phys. Chem. C*, **2010**, *114*, 8814.

(49) S. Wunder, Y. Lu, M. Albrecht, M. Ballauff, *ACS Catal*., **2011**, *1*, 908.

(50) P. Herves, M. Perez-Lorenzo, L. M. Liz-Marzan, J. Dzubiella, Y. Lu, M. Ballauff, *Chem. Soc. Rev.*, **2012**, *41*, 5577.

(51) J. A. Moulijin, A. E. van Diepen, F. Kapteijn, *Appl. Catal. A: General*, **2001**, *212*, 3.

(52) Z. Deng, M. Chen, L. Wu, *J. Phys. Chem. C*, **2007**, *111*, 11692.

Chapter 5. Silica-Coated Silver/Gold Composite Nanoboxes Having Enhanced Catalytic Performances and Reusability[†]

[†] This is reproduced from Jaewon Lee, Kyusik Han, and Du-Jeon Jang, *Appl. Catal. A: General*, **2014**, *469*, 380.

5.1. Abstract

SiO_2-coated Ag/Au composite hollow nanoboxes, $Ag_{0.7}Au_{0.3}@SiO_2$ core-shell nanocomposites, having high catalytic performances and enhanced catalytic reusability have been fabricated via a galvanic replacement reaction of SiO_2-coated silver nanocubes. Compared with SiO_2-coated Ag nanocubes, SiO_2-coated Ag/Au composite nanoboxes have been found to catalyze the degradation of 4-nitrophenol more rapidly in the presence of $NaBH_4$ due to fast diffusion. In contrast to bare Ag/Au composite nanoboxes, SiO_2-coated Ag/Au composite nanoboxes can be recycled continuously for the catalytic degradation of 4-nitrophenol in the presence of $NaBH_4$. We consider that silica coating enhances the stability of Ag/Au composite nanoboxes enormously by blocking the dissolution and aggregation of nanoparticles thoroughly.

5.2. Introduction

The design and controlled fabrication of nanostructured materials having functional properties have been extensively studied.[1-5] In particular, nanoscale noble metals have attracted considerable attention from researchers scientifically as well as industrially, due to their novel characteristic optical, physical, and chemical properties, which are substantially different from the respective properties of bulkscale noble metals.[6-7] In the case of silver and gold nanoparticles, they have been well known to show strong UV/vis absorption bands depending on sizes and shapes on account of their surface-plasmon oscillation modes of conduction electrons.[8-13] Among a variety of metallic nanostructures, core-shell or alloy bimetallic composite nanostructures of gold and silver in colloidal solutions have been broadly investigated, because they can exhibit unusual electronic, optical, and catalytic properties that are absent in the corresponding monometallic nanostructures.[13-16] Moreover, bimetallic hollow nanopartcles possess structurally tunable features such as shell thickness, chemical composition, and interior cavity size, leading to relatively high surface-to-volume ratios and low densities compared to their solid nanomaterials.[11-18] Due to the above outstanding properties, hollow bimetallic nanostructures have been utilized widely in biological and chemical sensing and catalysis.[14-18] Generally, hollow nanostructures have been fabricated via novel approaches such as the Kirkendall effect, the Ostwald ripening, and the galvanic replacement. Among them, the galvanic replacement reaction

exploiting the different reduction potentials of two metals requires a simple apparatus and causes little waste. Thus, this method has been often used to form hollow-structured nanocatalysts.[19-21]

Considerable studies have been developed to improve catalytic activities depending on the types and structures of nanomaterials.[15,18,23-30] Especially, diverse catalytic studies using noble-metal nanocatalysts have been reported. As an example, Xia et al. have compared the catalytic activities of Au-based nanocages, nanoboxes, and nanoparticles by decomposing 4-nitrophenol in the presence of $NaBH_4$, suggesting that nanocages having a high surface area have enhanced catalytic efficiency.[18] However, the reusability of nanocatalysts decomposing organic dyes has been hardly reported yet. Indeed, as nanocatalysts decompose organic dyes such as rhodamine B, methylene blue, and 4-nitrophenol, their catalytic activity has been known to decrease steadily because decomposed organic products absorbed on the nanocatalysts hinder interactions between the nanocatalysts and the organic dyes. Moreover, nanocatalysts can aggregate mutually during the catalytic reaction, implying that they can be scarcely reused.[7,8] Therefore, some ways to extend the limited usability of nanocatalysts should be found to lower the overall price of noble-metal nanocatalysts.

SiO_2, known as a porous material, has been reported to coat metallic nanoparticles, forming core-shell nanostructures.[30-38,51] Silica coating to improve the durability of precious-metal nanocatalysts has been studied by many research groups.[31-33,36,37,49] However, SiO_2 coating consisting of small

pores makes it difficult for outside organic molecules and inside metal ions to diffuse in and out, limiting galvanic replacement and catalytic activity.[35] However, as temperature is increased and $NaBH_4$(s) is added into a colloidal solution of SiO_2-coated silver nanoparticles, the amount and the sizes of pores in the coated SiO_2 increase, enabling metallic ions and organic molecules to penetrate through the SiO_2 shells more efficiently.[34] Thus, the coating of core metallic nanomaterials with SiO_2 has been utilized usefully in the field of catalysis as the coating blocks the dissolution and aggregation of nanoparticles to sustain the catalytic activity of metallic nanomaterials.

In this report, we have synthesized silver nanocubes and coated them with SiO_2 via the modifided Stöber method to enhance the stability of metallic nanocatalysts.[39] Then, SiO_2-coated silver nanocubes have been transformed into SiO_2-coated Ag/Au composite nanoboxes via a galavanic replacement reaction to increase the catalytic efficiency of the core metallic nanostructures.[18] Finally produced nanostructures having high catalytic performances can be recycled consecutively as aggregation and dissolution that tend to decrease catalytic activity hardly take place during the decomposion of an organic dye. The catalytic activity of SiO_2-coated Ag/Au composite nanoboxes has been measured by monitoring the absorption spectral changes of 4-nitrophenol in the presence of $NaBH_4$, revealing that hollow-morphological nanoparticles have highly enhanced catalytic activities and that catalytic activity of the SiO_2-coated nanocatalysts can remain almost invariable in spite of consecutive reuse.

5.3. Experimental Details

Silver Nanocubes. Silver nanocubes were prepared using a polyol process; 0.40 mL of 3.0 mM Na_2S(EG), 7.5 mL of 0.36 mM PVP(EG), and 2.5 mL of 280 mM $AgNO_3$(EG) was injected into 30 mL of EG, which had been already heated in an oil bath at 150 °C under magnetic stirring. The resultant product was rinsed with acetone and centrifuged at 3,000 rpm for 30 min. Then, the product was rinsed with water and centrifuged at 9,300 rpm for 10 min. The above processes were repeated three times and the product was redispersed in 40.0 mL of deionized water.

Ag/Au Composite Nanoboxes. The above prepared silver nanocubes were converted into Ag/Au composite nanoboxes via a galvanic replacement reaction. 20 mL of 18 μM PVP(EG) was heated at 100 ℃ under magnetic stirring and 0.60 mL of the prepared aqueous colloidal solution of silver nanocubes was added. 0.50 mL of 0.50 mM $HAuCl_4$(aq) was injected into the reaction flask. Then, produced Ag/Au composite nanoboxes were washed by centrifugation at 12,000 rpm for 20 min and were redispersed in 4 mL of deionized water.

Silica Coating of Silver Nanocubes. Silver nanocubes were coated with SiO_2 following the Stöber method;[39] 1.0 mL of the aqueous colloid of silver nanocubes was added to a mixture containing 25 mL of ethanol, 4.0 mL of deionized water, 20 μL of TEOS, and 2.0 mL of ammonia water under vigorous

magnetic stirring. After being stirred for 1 h, the resulting mixture was separated by centrifugation at 8000 rpm and washed with ethanol three times. The product was dispersed in 10 mL of 18 μM PVP(aq). 16 mmol of $NaBH_4$(s) was added to the mixture, which was then heated at 95 °C for 30 min. The resulting colloid was centrifuged, washed with water several times, and dispersed in 50 mL of deionized water to produce an aqueous colloidal solution of SiO_2-coated silver nanocubes.

SiO_2-Coated Ag/Au Composite Nanoboxes. To fabricate SiO_2-coated Ag/Au composite nanoboxes via a galvanic replacement reation of SiO_2-coated silver nanocubes with $HAuCl_4$, 10 mL of the as-stored colloidal solution of SiO_2-coated silver nanocubes was heated to 90 °C and 0.50 mL of 1.0 mM $HAuCl_4$(aq) was added drop by drop under vigorous magnetic stirring. The mixture was refluxed for 20 min to generate SiO_2-coated Ag/Au composite nanoboxes.[34,35]

Characterization. While transmission electron microscopic (TEM) images were obtained with a microscope (Carl Zeiss, LIBRA 120), scanning transmission electron microscopy (STEM) images, and energy-dispersive X-ray (EDX) line-scanned elemental intensity profiles, and EDX elemental maps were measured using a high-resolution microscope (FEI, Tecnai F20). Absorption spectra were measured using a temperature-controllable spectrophotometer (Scinco, S-3000).

Catalytic Performances. Catalysis experiments were carried out in a polyphenyl cell having a path length of 10 mm. 0.10 mL of 2.0 mM 4-nitrophenol(aq) was diluted with 1.0 mL deionized water, which was then added with 0.10 mL of a colloid solution containing SiO_2-coated silver nanocubes or SiO_2-coated Ag/Au composite nanoboxes. The resulting solution was shaken gently and 1.5 mL of ice-cold 0.10 M $NaBH_4$(aq) was added rapidly. The absorption spectral changes of the solution at a given temperature were measured at scheduled intervals using a spectrophotometer to monitor the catalytic performances of nanocatalysts. Catalysis experiments were carried out repeatedly to test the stability of the nanocatalysts.

5.4. Results and Discussion

As-prepared silver nanocubes have an average edge length of 47±2 nm (Figure 5-1a) while Ag/Au composite hollow nanoboxes, fabricated via a galvanic replacement reaction of silver nanocubes with $HAuCl_4$, have rough surfaces with a typical outside edge length of 52±3 nm (Figure 5-1b). Ag/Au composite nanoboxes have partially empty interiors because the central portions of nanoboxes are brighter than the edge portions. Figure A-1c shows that silver nanocubes have been coated with SiO_2 with a typical thickness of 38±2 nm following the Stöber method to produce SiO_2-coated silver nanocubes. On the other hand, SiO_2-coated Ag/Au composite hollow nanoboxes with rough

surfaces, fabricated via a galvanic replacement reation of SiO_2-coated silver nanocubes with $HAuCl_4$, have been found to have an average shell thickness of 25±3 nm (Figure 5-1d). The size of the empty interiors and the thickness of the SiO_2 shells in SiO_2-coated Ag/Au composite nanoboxes have been controlled by adjusting the amounts of $HAuCl_4$ and TEOS, respectively.

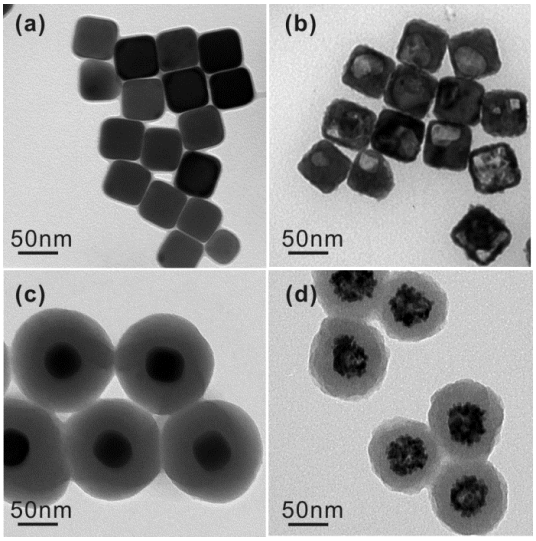

Figure 5-1. TEM images of (a) Ag nanocubes, (b) Ag/Au alloy nanoboxes, (c) SiO_2-coated Ag nanocubes, and (d) SiO_2-coated Ag/Au composite nanoboxes.

The EDX elemental profiles of a SiO_2-coated Ag/Au composite nanobox, scanned along the indicated dashed line of the insetted STEM image in Figure 5-2a, show that a nanobox consisting of silver and gold atoms compositely is covered with a shell consisting of silicon and oxygen atoms compositely. The full width at the half maximum (FWHM) of silver atoms is 45.6 nm while that of gold atoms is 49.0 nm. This suggests that Ag and Au form the core nanobox compositely although Ag and Au are enriched in the inner and the outer surfaces

of the core nanobox, respectively. The EDX elemental maps of Figure A-2b also support the above description of the SiO_2-coated Ag/Au composite nanobox. On the other hand, the surfaces of the core and the shell of a SiO_2-coated Ag nanocube are much smoother than those of the SiO_2-coated Ag/Au composite nanobox. The FWHM of silver atoms in the SiO_2-coated Ag nanocube has been found to be 24.8 nm, which is much smaller than that of silver atoms (45.6 nm) in the SiO_2-coated Ag/Au composite nanobox of Figure 5-2a.

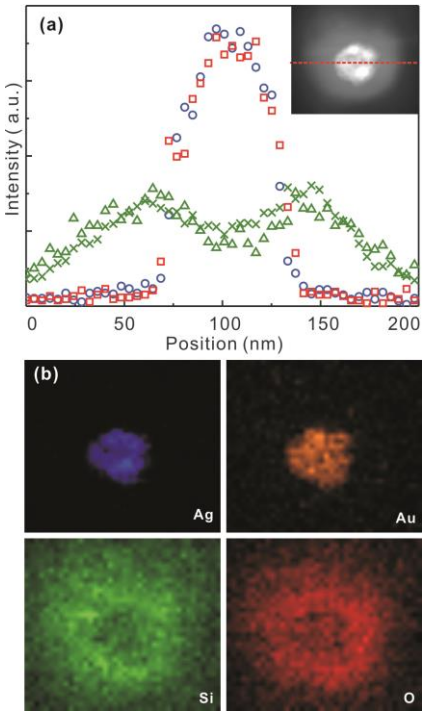

Figure 5-2. (a) Area-normalized EDX line-scanned elemental intensity profiles of a SiO_2-coated Ag/Au composite nanobox for (squares) Au, (circles) Ag, (triangles) Si, and (crosses) O along the indicated dashed line of the insetted STEM image. (b) EDX elemental maps of the above STEM image.

Figure 5-3 shows the absorption spectra of silver nanocubes, Ag/Au composite nanoboxes, SiO_2-coated Ag nanocubes, and SiO_2-coated Ag/Au composite nanoboxes, which were centrifuged and redispersed in water. The surface-plasmon absorption band of the silver nanocubes is observed at 440±45 nm due to the Mie plasmon resonances. As the silver nanocubes were coated with SiO_2, their surface-plasmon resonance band was slightly shifted to 460±53 nm due to the change of the refractive index of the surrounding medium.[41] In other words, because the refractive index of SiO_2 (1.54) is a little higher than that of water (1.31), the surface-plasmon resonance peak of SiO_2-coated Ag nanocubes was red-shifted by 20 nm.[42,43] The transformation of silver nanocubes into Ag/Au composite nanoboxes through a galvanic replacement reaction with $HAuCl_4$ causes severe spectral changes in surface-plasmon resonances. As silver nanocubes were converted to Ag/Au composite hollow nanoboxes, surface-plasmon resonances were red-shifted on a large scale to 640 nm while their half width at the half maximum (HWHM) became as broad as 165 nm. In other words, the increase of the hollow interiors has resulted in the extensive red shift and broadening of surface-plasmon resonances.[41] Furthermore, because hollow structures have very strong plasmonic fields on account of coupling between their interior and exterior surface fields,[41] the surface-plasmon resonances of Ag/Au composite nanoboxes are observed at a much longer wavelength of 700±148 nm as they are coated with SiO_2.

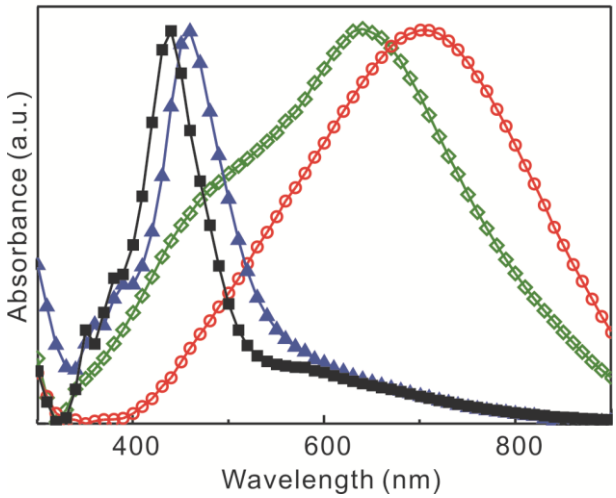

Figure 5-3. Peak-normalized absorption spectra of (squares) Ag nanocubes, (triangles) SiO_2-coated Ag nanocubes, (diamonds) Ag/Au composite nanoboxes, and (circles) SiO_2-coated Ag/Au composite nanoboxes suspended in water.

SiO_2-coated Ag/Au composite nanoboxes have been fabricated via a two-step process. First, silver nanocube structures, chosen as templates owing to their higher surface areas than those of silver nanospheres, were synthesized using a polyol process and coated with SiO_2 via the Stöber method. In order to maintain the as-prepared sizes and shapes of silver nanocubes, we added PVP(aq) as a surfactant into the colloidal solution of silver nanocubes prior to coating the nanocubes with SiO_2.[8] Second, a galvanic replacement reaction between silver nanocubes and $HAuCl_4$ to form Ag/Au composite nanoboxes took place within SiO_2 nanoshells.[35] As $AuCl_4^-$ ions were added into a hot aqueous colloidal solution of SiO_2-coated silver nanocubes, they diffused through the pores of coated SiO_2 to contact with silver nanocubes. Then, Ag

atoms were oxidized into Ag^+ ions and $AuCl_4^-$ ions were reduced into Au atoms at the same time, as shown in the following equation:

$$3\,Ag(s) + AuCl_4^-(aq) \rightarrow Au(s) + 3\,Ag^+(aq) + 4\,Cl^-(aq) \qquad (1)$$

Galvanically reduced Au atoms underwent nucleation to generate shells on the surfaces of silver nanocubes, whereas oxidized Ag^+ ions diffused out continuously across the boundaries of the porous SiO_2 shells to form Ag/Au composite nanoboxes having empty interiors. However, we have found experimentally that the galvanic replacement of silver nanocubes with $AuCl_4^-$ to form Ag/Au composite nanoboxes did not take place easily within SiO_2 shells because Au ions could not penetrate into the SiO_2 shells due to their small pore sizes. Thus, by adding $NaBH_4$(s) into the colloidal solution and increasing the temperature of the solution up to 95 °C,[34] we have increased the sizes and the amount of pores in the SiO_2 shells largely, as indicated in Figure 5-1. The increment of pore sizes enabled Au and Ag ions to diffuse in and out of SiO_2 shells readily, leading a galvanic replacement reaction to occur within the SiO_2 shells easily. Thus, the galvanic replacement reaction of silver nanocubes with $AuCl_4^-$ ions within SiO_2 shells has produced SiO_2-coated Ag/Au composite nanoboxes facilely.

We have investigated the catalytic properties of SiO_2-coated Ag/Au composite nanoboxes by monitoring time-dependent absorbance changes of 4-nitrophenol solutions containing $NaBH_4$. For the sake of the comparison of catalytic performances, catalytic properties of SiO_2-coated Ag nanocubes have also been measured at the same conditions, revealing that the catalytic activity

of SiO_2-coated Ag/Au composite nanoboxes is more efficient than that of SiO_2-coated Ag nanocubes. In other words, the absorbance of 4-nitrophenol at 400 nm has been found to decrease much more rapidly in the presence of SiO_2-coated Ag/Au composite nanoboxes (Figure 5-4a) than in the presence of SiO_2-coated Ag nanocubes (Figure 5-4b). A neutral or acidic aqueous solution of 4-nitrophenol shows an absorption peak at 317 nm, whereas 4-nitrophenol is transformed to 4-nitrophenolate in an alkaline aqueous solution to exhibit an absorption peak at 400 nm. During the measurement of catalytic performances, the addition of $NaBH_4$(aq) as a reducing agent induces the solution to be alkaline, making 4-nitrophenolate be dominant species. After nanocatalysts were added, the absorption peak at 400 nm decreased gradually through the reduction reaction of 4-nitrophenol to form 4-aminophenol showing a new absorption peak at 296 nm.[44,47] The clear appearance of an isosbestic point at 324 nm suggests that 4-nitrophenol molecules have been transformed quantitatively into 4-aminophenol molecules. Figure 5-4c demonstrates that a certain period of time, called the induction period, was required for 4-nirtophenol to adsorb onto the metallic surfaces of SiO_2-coated nanocatalysts before the catalytic reaction was initiated. As shown in Figure 5-4c, the induction period of SiO_2-coated Ag/Au composite nanoboxes was shorter than that of SiO_2-coated Ag nanocubes because the pore size and thickness of the SiO_2 shells of SiO_2-coated Ag/Au composite nanoboxes are bigger and thinner than the respective ones of SiO_2-coated silver nanocubes.[23,45]

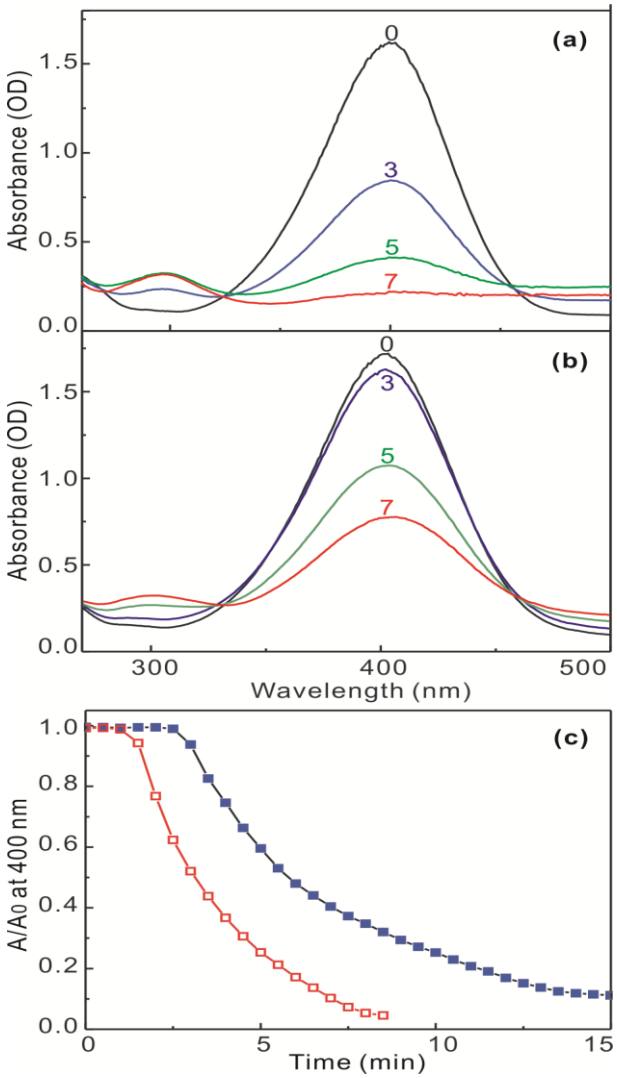

Figure 5-4. Absorption spectra of $NaBH_4$-added aqueous 4-nitrophenol solutions, measured at elapsed times indicated in the units of min after adding aqueous colloidal solutions of (a) SiO_2-coated Ag/Au composite nanoboxes and (b) SiO_2-coated Ag nanocubes at 25 ºC. (c) Decay kinetic profiles at 400 nm of the above described absorption spectra of (closed) SiO_2-coated Ag nanocubes and (open) SiO_2-coated Ag/Au composite nanoboxes.

In our experiment, because the concentration of $NaBH_4$ was substantially higher than that of 4-nirtophenol during the catalytic reaction, the pseudo-first-order kinetics could be applied to obtain reaction rate constants.[46] Furthermore, as seen in Figure 5-5, the linear relationship between $\ln(A/A_0)$ and time supports the pseudo-first-order assumption, manifesting that the slope of a straight line is a reaction rate constant. The decrease of absorbance in the absence of nanocatalysts was not observed at all because of the kinetic barrier arising from large potential difference between the donor and the acceptor species, which reduces the feasibility of this reaction despite the thermodynamically stability of the reduction of 4-nitrophenol to 4-aminophenol (E_0 for 4-nitrophenol/4-aminophenol = -0.76 V and E_0 for H_3BO_3/BH_4^- = -1.33 V).[47] Thus, the catalytic rate constants of nanocatalysts at diverse temperatures have been calculated directly from the plots of Figure 5-5a and b, revealing that as the temperature was increased, the catalytic efficiency of nanocatalysts was enhanced enormously (Table 5-1) because the movement of ions became fast gradually with the increment of temperature. In addition, the frequency factor and the activation energy of the catalytic degradation have been obtained from the Arrhenius plots of Figure 5-5c and summarized in Table 5-1.

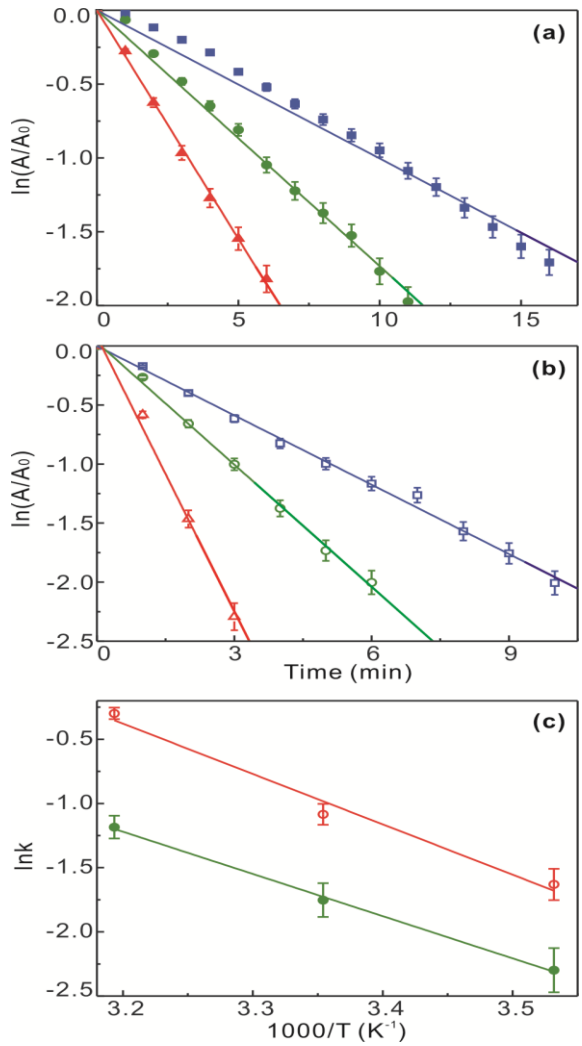

Figure 5-5. First-order kinetics, $\ln(A/A_0)$ vs. time, for 4-nitrophenol catalyzed by using (a) SiO_2-coated Ag nanocubes and (b) SiO_2-coated Ag/Au composite nanoboxes at different temperatures of (squares) 10, (circles) 25, and (triangles) 40 °C. (c) Arrhenius plots for the reduction reaction of 4-nitrophenol catalyzed by (open) SiO_2-coated Ag/Au composite nanoboxes and (closed) SiO_2-coated Ag nanocubes in the presence of $NaBH_4$.

As seen in Table 5-1, the catalytic rate constant of SiO_2-coated Ag/Au composite nanoboxes (box@SiO_2) is faster by 2 times at 25 °C than that of

SiO_2-coated Ag nanocubes (cube@SiO_2) in spite of a little higher activation energy (E_a) because the frequency factor of box@SiO_2 is larger by 65 times than that of cube@SiO_2, describing well that the nanoboxes have more active sites than the nanocubes. The activation energies listed in Table 5-1 are much smaller than reported values,[15,51] suggesting that the catalytic rate is mainly determined by the diffusion rate of 4-nitrophenol to an active site of a nanocatalyst. It has been reported[23,52] that catalytic activation energies with shell-shell or alloy nanostructures are somewhat higher than those with pure nanostructures. This agrees with our observation that the activation energy of box@SiO_2 is slightly higher than that of cube@SiO_2. The catalytic acitivity of nanoparticles has been found to be related to the fraction of atoms located at corners, edges, and defects.[48] Moreover, it is known that atoms at these locations are catalytically active.[49] In the case of SiO_2-coated Ag/Au composite nanoboxes, they have large amounts of defect sites, sharp edges, and corners to make these nanoparticles catalycally very active. In the end, because the catalysis occurs on a defect site,[48] Ag/Au composite nanoboxes having large amounts of defect sites exhibit better catalytic performances. Additionally, gold has been known well to have better catalytic activity than silver, also demonstrating that the composite nanoboxes including gold atoms perform catalytic reactions more efficiently compared with the nanocubes having only silver atoms.

Table 5-1. Comparison of rate constants, frequency factors, and activation energies for the reduction of 4-nitrophenol via SiO_2-coated nanocatalysts in the presence of $NaBH_4$.

Nanocatalyst	Rate constant at 25 °C (min^{-1})	Frequency factor (min^{-1})	Activation energy (kJ mol^{-1})
cube@SiO_2[a]	0.173±0.003	1.7 x 10^4	27.3
box@SiO_2[b]	0.338±0.004	1.1 x 10^6	32.6

[a] SiO_2-coated Ag nanocubes. [b] SiO_2-coated Ag/Au composite nanoboxes.

Since the catalytic reaction by metallic atoms is a surface phenomenon, the reduction process of 4-nitrophenol to form 4-aminophenol could be explained as follows.[47] BH_4^- as a nucleophile can donate electrons to metal nanocatalysts, and 4-nitrophenol as an electrophile can capture electrons from the metal nanocatalysts. Thus, metal nanocatalyts play an important role as electron relays for the reduction reaction of 4-nitrophenol with $NaBH_4$.[50] Consequently, in the case of nanostructures having empty interiors like nanoboxes, because catalytic electron relays take place on the inner and the outer surfaces of the hollow nanostructures, their catalytic efficiency has been enhanced compared to the corresponding solid nanostructures having only outer surfaces.

The reusable ability of SiO_2-coated Ag/Au composite nanoboxes and Ag/Au composite nanoboxes has been measured by repeating catalytic experiments. Catalysis recycle experiments were performed five times to prove the catalytic stability of nanocatalyts. Both nanocatalysts were separated by centrifugation and reused for consecutive catalysis reactions. As shown in Figure 5-6, the catalytic efficiency of bare Ag/Au composite nanoboxes has been decreased

drastically after several cycles of catalysis due to the absence of protecting SiO_2 shells, whereas SiO_2-coated Ag/Au composite nanoboxes maintain similar catalytic performances even after five successive cycles of reactions. These results demonstrate well that SiO_2 shells can efficiently protect the Ag/Au composite nanoboxes from the aggregation and dissolution of metallic nanocatalysts during catalytic reactions. Furthermore, the TEM images of Figure 5-7 indicate that SiO_2-coated Ag/Au composite nanoboxes have preserved their as-prepared structures well despite five successive cycles of catalytic reactions. Thus, SiO_2-coated Ag/Au composite nanoboxes have been proven to have an excellent stability of nanocatalysts and they can be utilized well in the catalytic industry.

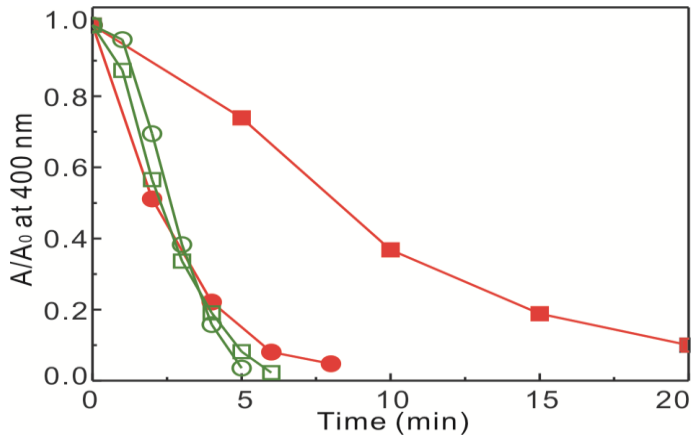

Figure 5-6. Absorption-decay kinetic profiles of 4-nitrophenol catalyzed by (open) SiO_2-coated Ag/Au composite nanoboxes and (closed) bare Ag/Au composite nanoboxes, recycled at (circles) the third time and (squares) the fourth time, in the presence of $NaBH_4$ at 25 ^oC.

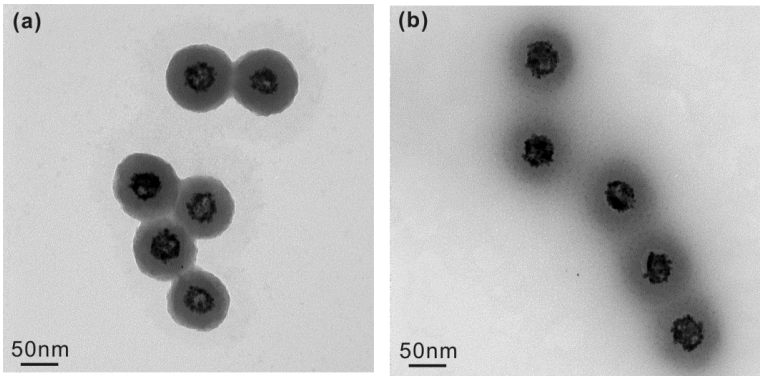

Figure 5-7. TEM images of (a) SiO_2-coated Ag/Au composite nanoboxes before a catalysis experiment, and (b) SiO_2-coated composite Ag/Au nanoboxes after running catalysis experiments 5 times

5.5. Conclusion

SiO_2-coated Ag/Au composite hollow nanoboxes, $\underline{Ag_{0.7}Au_{0.3}@SiO_2}$ core-shell nanocomposites, have been fabricated via a galvanic replacement reaction of SiO_2-coated silver nanocubes with $HAuCl_4$. Silver nanocubes within SiO_2 shells were readily oxidized by Au^{3+} ions to generate Ag^+ ions, which diffused out of SiO_2 shells subsequently. Simultaneously, Au^{3+} ions were reduced to Au atoms, adsorbing on the surfaces of silver nanocubes to form SiO_2-coated Ag/Au composite hollow nanoboxes finally. Compared with SiO_2-coated Ag nanocubes, SiO_2-coated Ag/Au composite nanoboxes have been found to catalyze the degradation of 4-nitrophenol more rapidly in the presence of $NaBH_4$, suggesting that fast diffusion in nanoboxes results in efficient catalytic

performances. In addition, we have obtained various kinetic data such as rate constants, frequency factors, and activation energies to reveal the detailed catalytic mechanism of SiO_2-coated Ag/Au composite nanoboxes. Furthermore, owing to the protection of the SiO_2 shells, SiO_2-coated Ag/Au composite nanoboxes have sustained catalytic activity continuously after being recycled repeatedly.

5.6. Acknowledgements

This work was supported by research grants through the National Research Foundation (NRF) of Korea funded by the Korea government (2012-006345 and 2011-0028981). D.J.J. is also thankful to the SRC program of NRF (2007-0056095).

5.7. References

(1) J. –Y. Kim, S.J. Kim, D. –J. Jang, *J. Phys. Chem. C*, **2011**, *115*, 672.

(2) H. Yoo, J. Sharma, H. –C. Yeh, J.S. Martinez, *Chem. Commun*., **2010**, *46*, 6813.

(3) H.-B. Kim, D. –J. Jang, *Cryst. Eng. Comm*., **2012**, *14*, 6946.

(4) Y.H. Kim, J.–Y. Kim, D.–J. Jang, *J. Phys. Chem. C*, **2012**, *116*, 10296.

(5) J.-Y. Kim, H. Jeong, D. –J. Jang, *J. Nanopart. Res*., **2011**, *13*, 6699.

(6) S.J. Kim, C.S. Ah, D.–J. Jang, *Adv. Mater*., **2007**, *19*, 1064.

(7) M.R. Kim, J.–Y. Kim, S.J. Kim, D.–J. Jang, *Appl. Catal. A: General,* **2011**, *393*, 317.

(8) M.R. Kim, D.K. Lee, D.–J. Jang, *Appl. Catal. B: Environ*., **2011**, *103*, 253.

(9) C. Noguez, *J. Phys. Chem. C*, **2007**, *111*, 3806.

(10) S.J. Kim, D. –J. Jang, *Mater. Lett*., **2008**, *62*, 4500.

(11) M.A. Mahmoud, M.A. El–Sayed, *Langmuir*, **2012**, *28*, 4051.

(12) P.K. Jain, X.H. Huang, I.H. El–Sayed, M.A. El–Sayed, *Acc. Chem. Res*., **2008**, *41*, 1578.

(13) J. Gao, X. Ren, D. Chen, F. Tang, *J. Ren, Scripta Mater*., **2007**, *57*, 687.

(14) X. Lu, L. Au, J. McLellan, Z.–Y. Li, M. Marquez, Y. Xia, *Nano Lett*., **2007**, *7*, 1764.

(15) M.A. Mahmoud, F. Saira, M.A. El–Sayed, *Nano Lett*., **2010**, *10*, 3764.

(16) H. Petrova, C.H. Lin, M. Hu, J. Chen, A.R. Siekkinen, Y. Xia, *Nano Lett*., **2007**, *7*, 1059.

(17) U. Jeong, J.–U. Kim, Y. Xia, *Nano Lett*., **2005**, *5*, 937.

(18) J. Zeng, Q. Zhang, J. Chen, Y. Xia, *Nano Lett*., **2010**, *10*, 30.

(19) X.W. Lou, L.A. Archer, Z. Yang, *Adv. Mater*., **2008**, *20*, 3987.

(20) Y. Yin, R.M. Rioux, C.K. Erdonmez, S. Hughes, G.A. Somorjai, A.P. Alivisatos, *Science*, **2004**, *304*, 711.

(21) H.G. Yang, H.C. Zeng, *J. Phys. Chem. B*, **2004**, *108*, 3492.

(22) F. Caruso, *Chem. Eur. J*., **2000**, *6*, 413.

(23) M.A. Mahmoud, M.A. El–Sayed, *Nano Lett*., **2011**, *11*, 946.

(24) T. Herricks, J. Chen, Y. Xia, *Nano Lett*., **2004**, *4*, 2367.

(25) R. Krishnaswamy, H. Remita, M. Inpéror–Clerc, C. Even, P. Cavidson, B. Pansu, *Chem. Phys. Chem*., **2006**, *7*, 1510.

(26) Y. –J. Han, J.M. Kim, G.D. Stucky, *Chem. Mater*., **2000**, *12*, 2068.

(27) Y. Luo, S.K. Lee, H.Hofmeister, M. Steinhart, U. Gösele, *Nano Lett*., **2004**, *4*, 143.

(28) Y. Song, Y. Yang, C.J. Medforth, E. Pereira, A.K. Singh, H. Xu, Y. Jiang, C.J. Brinker, F.V. Swol, J.A. Shelnutt, *J. Am. Chem. Soc*., **2004**, *126*, 635.

(29) K.Y. Lee, Y.W. Lee, J. –H. Lee, S.W. Han, *Colloid Surface A*, **2010**, *372*, 146.

(30) Y.S. Kim, D. –J. Jang, *Chem. Commun*., **2013**, *49*, 8940.

(31) Y. Chen, C. Wang, H. Liu, J. Qiu, X. Bao, *Chem. Commun*., **2005**, *42*, 5298.

(32) J. Ge, Q. Zhang, T. Zhang, Y. Yin, *Angew. Chem. Int. Ed*., **2008**, *47*, 8924.

(33) S. H. Joo, J. Y. Park, C.-K. Tsung, Y. Yamada, P.D. Yang, G. A. Somorjai, *Nat. Mater*., **2009**, *8*, 126.

(34) T. Zhang, J. Ge, Y. Hu, Q. Zhang, S. Aloni, Y. Yin, *Angew. Chem. Int. Ed*., **2008**, *120*, 5890.

(35) H. Li, C. –S. Ha, I. Kim, *J. Nanopart. Res*. **2010**, *12*, 958.

(36) Q. Zhang, T. Zhang, J. Ge, Y. Yin, *Nano Lett*. **2008**, *8*, 2867.

(37) X. Huang, C. Guo, J. Zuo, N. Zheng, G.D. Stucky, *Small,* **2009**, *5*, 361.

(38) X. Zhang, W. Jiang, Y. Zhou, S. Xuan, C. Peng, L.Zong, X. Gong, *Nanotechnology*, **2011**, 22.

(39) W. Stöber, A. Fink, E. Bohn, *J. Colloid Interface Sci*., **1968**, *26*, 62.

(40) S.E. Skrabalak, L. Au, X. Li, Y. Xia, *Nat. Protoc*., **2007**, *9*, 2182.

(41) M.A. Mahmoud, M.A. El–Sayed, *J. Am. Chem. Soc*., **2010**, *132*, 12704.

(42) Y. Lu, Y. Yin, Z.–Y. Li, Y. Xia, *Nano Lett*., **2002**, *2*, 785.

(43) A. Kudelski, S.Wojtysiak, *J. Phys. Chem. C*, **2012**, *116*, 16167.

(44) P. Veerakumar, M. Velayudham, K. –L. Lu, S. Rajagopal, *Appl. Catal. A: General*, **2012**, *439*, 197.

(45) T. Ung, L. M. Liz-Marzan, P. Mulvaney, *Langmuir*, **1998**, *14*, 3740.

(46) N.S. Langeroodi, Russ. *J. Phys. Chem. A*, **2012**, *86*, 628.

(47) A. Gangula, R. Podila, R. M, L. Karanam, C. Janardhana, A.M. Rao, *Langmuir*, **2011**, *27*, 15268.

(48) R. Narayanan, M.A. El–Sayed, *Nano Lett*., **2004**, *4*, 1343.

(49) J.G. Lee, J.C. Park, H.J. Song, *Adv. Mater*., **2008**, *20*, 1523.

(50) Z.X. Wang, X.B. Chen, M. Chen, L.M. Wu, *Langmuir*, **2009**, *25*, 7646.

(51) J. –A. Kwak, D.K. Lee, D. –J. Jang, *Appl. Catal. B: Environ*., **2013**, *142-143*, 323.

(52) X. Huang, X. Wang, X. Wang, X. Wang, M. Tan, W. Ding, X. Lu, *J. Catal*., **2013**, *301*, 217.

Appendices

A.1. List of Publications

1. **Jaewon Lee**, Kyusik Han, and Du-Jeon Jang "Silica-coated silver/gold composite nanoboxes having enhanced catalytic performances and reusability" Appl. Catal. A: General, 2014, 469, 380.

2. Myounghee Son, **Jaewon Lee**, and Du-Jeon Jang "Light-treated silica-coated gold nanorods having highly enhanced catalytic performances and reusability" J. Mol. Catal. A: Chem., 2014, 385, 38.

3. **Jaewon Lee** and Du-Jeon Jang "Laser-induced fabrication of Ag@SiO_2@Ag sandwich nanostructures having enhanced catalytic performances" RSC Adv., 2015, 5, 64268.

4. **Jaewon Lee** and Du-Jeon Jang "Highly efficient catalytic performances of eco-friendly grown silver nanoshells" J. Phys. Chem. C, 2016, 120, 4130.

5. Dongki Lee, **Jaewon Lee**, Ki-Hee Song, Hanju Rhee, and Du-Jeon Jang "Formation and decay of charge carriers in aggregate nanofibers consisting of poly-(3-hexylthiophene)-coated gold nanoparticles" Phys. Chem. Chem. Phys., 2016, 18, 2087.

6. **Jaewon Lee**, Yeonho Kim, Joon Ki Kim, Seongchan Kim, Dal-Hee Min, and Du-Jeon Jang "Highly efficient photocatalytic performances of SnO_2-deposited ZnS nanorods based on interfacial charge transfer" Appl. Catal. B: Environ., 2017, 205, 433.

7. **Jaewon Lee**, Sooho Ham, and Du-Jeon Jang "Facile fabrication of Cu-exchanged ZnS nanoadsorbents for highly efficient removal of contaminants" J. Environ. Chem. Eng., 2017, 5, 4431.

8. Tae-Hyeon Park. Hyeri Lee. **Jaewon Lee**, and Du-Jeon Jang "Morphology evolution of Ag/Au nanocomposites via temperature-controlled galvanic exchange to enhance catalytic activity" RSC Adv., 2017**,** *7,* 7718-7724.

A.2. List of Presentations

A.2.1. International Presentations

1. **Jaewon Lee,** Kyusik Han, and Du-Jeon Jang "Silica-coated silver/gold composite nanoboxes having enhanced catalytic performances and reusability" Gordon Research Conference on Colloidal Macromolecular & Polyelectrolyte Solutions, Ventura, CA, USA (**2014)**.

2. **Jaewon Lee,** Kyusik Han, and Du-Jeon Jang "Silica-coated silver/gold composite nanoboxes having enhanced catalytic performances and reusability" 5th International Colloids Conference, Amsterdam, Netherlands (**2015**).

3. **Jaewon Lee** and Du-Jeon Jang "Laser-induced fabrication of Ag@SiO_2@Ag nanostructures with highly catalytic performances" Gordon Research Conference, Hong Kong, China (**2016)**.

A.2.2. Domestic Presentations

1. Jong-Yeob Kim, **Jaewon Lee**, and Du-Jeon Jang "Laser Fabrication of Au@CdS One-Dimensional Nanocomposites" The 110th National Meeting of the Korean Chemical Society, Busan, Korea (**2012**).

2. **Jaewon Lee** and Du-Jeon Jang "Catalytic properties of Hollow Ag-Au@SiO2 Nanocomposites Synthesized via Galvanic Replacement of $Ag@SiO_2$ Nanocomposites" The 44th Winter Annual Conference of the Korean Vacuum Society, Pyeongchang, Korea (**2013**).

3. **Jaewon Lee** and Du-Jeon Jang "Catalytic Properties of Ag-Au alloy nanoboxes@SiO_2 synthesized via galvanic replacement" The 111st National Meeting of the Korean Chemical Society, Goyang, Korea (**2013**).

4. **Jaewon Lee** and Du-Jeon Jang "Catalytic performances of silica-coated Ag/Au alloy nanoboxes synthesized via galvanic replacement" The 113rd National Meeting of the Korean Chemical Society, Goyang, Korea (**2014**).

5. **Jaewon Lee** and Du-Jeon Jang "Laser-induce fabrication of $Ag@SiO_2@Ag$ sandwich nanostructures" The 115rd National Meeting of the Korean Chemical Society, Goyang, Korea (**2015**).

6. **Jaewon Lee** and Du-Jeon Jang "Eco-friendly fabrication of $Ag@SiO_2@Ag$ sandwich nanostructures" The 116th National Meeting of the Korean Chemical Society, Daegu, Korea (**2015**).

7. **Jaewon Lee** and Du-Jeon Jang "Catalytic Mechanism of Laser-Grown Silver Nanoshells" The 117th National Meeting of the Korean Chemical Society, Goyang, Korea (**2016**).

8. **Jaewon Lee** and Du-Jeon Jang "High photocatalytic activity of SnO_2/ZnS nanocomposites" The 119th National Meeting of the Korean Chemical Society, Goyang, Korea (**2017**).

Abstract (Korean)

다양한 형태와 구조를 갖는 반도체, 금속 기반 나노복합체를 수열, 용해열 반응 등 wetchemical synthesis 와 더불어 레이저유도 제조라는 금속의 특유한 광학적성질과 레이저 빛을 활용한 방법으로 제조하였다. 그리고 그에따른 나노복합체의 물리화학적 특성과 광학적 특성을 체계적으로 연구함과 동시에 오염물을 분해하는 수처리로 응용하였다. 제 1 장에서는 반도체 및 금속이 나노크기로 제한되었을 경우, 즉 양자제한효과에 따른 특성에 대해 소개하였다. 특히, 벌크사이즈와 비교하여, 나노사이즈의 물질에서 나타나는 금속과 반도체의 광학적 특성과 구조 및 형태제어에 따른 물리적, 화학적 특성 변화에 대해서 간략히 기술하였다. 또한, 나노입자를 합성하는 bottom-up 방식과 top-down 방식에 대한 소개와 더불어 나노물질의 광센서, 광촉매 장치, 태양전지와 같은 다양한 분야로의 응용가능성을 서술하였다.

2 장에서는 수열반응으로 ZnS 나노막대를 제조한 후, 주석(Sn) 전구체를 넣고 한번 더 수열반응을 보내 SnO_2 양자점들이 ZnS 나노막대위에 접합된 SnO_2/ZnS 이종접합 나노복합체를 제조하였다. 이는 단일 물질의 ZnS 나노 막대보다 빛 조사하에 유기염료 분해하는 광촉매 효율을 상당히 증대 시키는 결과를 얻게 되었다. 단일 ZnS 에 SnO_2 을 접합하게 되면, 빛 조사하에 생성된 전자와 정공들이 계면을 통해 서로 분리가 극대화 되어 더 많은 radical 종들을 생성시켜 유기염료 분해에 탁월한 능력을 보이게 된다. 이는 레이저를 이용한 형광과 형광 소멸시간을 통해 전자의 거동현상을

이해함으로써 작동 메커니즘을 이해하게 되었다. 또한, 이종접합에서 나타나는 interfacial absorption 을 관측하여 기존의 ZnS 가 자외선만을 감응하는 단점을 극복하여 visible 영역에서의 흡광증강도 함께 관측하였다. 손쉬운 수열합성 방법으로 두 나노구조체를 접합시키는 방법을 소개하였으며, 이에 따른 증강된 광촉매 효율 특성 분석과 처음으로 ZnS 의 band-edge 형광의 소멸시간을 측정하였다.

3 장에서는 반도체 나노물질들의 수처리로의 응용에 있어 광촉매외에 나노흡착제로 활용하고자 하였다. 우선, 다양한 형태를 갖는 ZnS 나노벨트, 나노막대, 나노시트를 오토클레이브를 이용하여 수열 및 용해열 반응으로 제조하였다. 양의 전하를 띠는 유기염료들과 중금속의 흡착을 정전기적인력으로 결합시키기위해 위의 ZnS 나노구조체를 음의전하로 유도 하고자 Cu^{1+} 전구체인 CuCl 을 위의 ZnS 나노물질에 몰 비율 (Zn/Cu)을 달리하면서 첨가하였다. ZnS 와 CuS 와의 용해도곱이 각각 10^{-24} 과 10^{-48} 으로 상당히 차이가 커서 자발적으로 양이온교환 반응이 발생한다. Zn^{2+}이온이 Cu^{1+}이온과 격자내에서 교환됨에 따라 전체적인 나노물질의 표면전하가 균형을 잃어 음의전하를 갖음을 Zeta potenitial 을 측정하여 확인하였다. Zn/Cu 의 최적화된 몰비율에서 가장 낮은 표면전하를 관측하고 이를 흡착제로 응용하였다. 보고된 다른 논문들의 무기물 나노흡착제와 비교하여 상당히 높은 수치의 흡착률을 보임을 확인하였고, Langmuir-isortherm 과 pseudo-second-order kinetics 을 통해 흡착이 발생되는 작동메커니즘을 자세히 분석하였다.

4 장에서는 금속/실리카 나노물질 합성방법에 있어 많이 사용되는 wetchemical synthesis 를 사용하지 않고 금속이 가지고 있는 고유한 SPR(surface plasmon resonance)의 광학적 성질과 레이저의 빛을 활용하여 laser-induced fabrication 이라는 독창적인 합성방법으로 금속/실리카 나노복합체를 제조하였다. Polyol 과정과 Stober 방법을 통해 균일한 크기의 은나노구에 실리카쉘을 쌓은 코어/쉘 나노복합체를 합성하였다. 그리고 용액내에 환원 되지 않고 남아있는 은 이온들을 pulse laser 빛을 활용하여 환원 시켜 실리카 쉘 표면에 흡착시키고 성장시키는 과정을 진행하였다. 물과 에탄올이 레이저 빛에 의해 라디칼을 생성시키고 이 라디칼 종들이 은 이온을 환원시켜 쉘 표면에 화학적 결합으로 흡착되어있는 은 나노입자들 위에서 성장한다는 메커니즘을 밝혔다. 또한, 환원제 $NaBH_4$ 존재하에서 유기염료인 로다민 B 분해 실험을 통한 촉매로의 응용에 있어서도 탁월한 능력을 보였주었으며, pseudo-first-order kinetics, Arrhenius plot 그리고 Erying plot 을 통해 전이 상태의 착화합물의 안정도와 활성화 에너지를 구해 촉매 반응의 메커니즘도 심층적으로 이해할 수 있었다.

마지막으로 5 장에서는 속빈 구조체를 제조 함에 있어서 산화/환원 전위차를 이용한 갈바닉 치환반응이라는 손쉬운 방법을 도입하여 속빈 형태의 나노 복합체를 합성하였다. 우선, 폴리올 과정을 통해 균일한 크기의 은 나노큐브를 제조하고, 금 전구체를 넣어줌으로써 갈바닉 치환과정을 유도하였다. 은은 산화되고 금은 환원되면서 속 빈형태의 금/은 나노 박스 형태로 자발적으로 변형

되게된다. 또한, 실리카 쉘로 둘러 쌓여 있기에 코어의 속 빈 형태가 갖는 내구성의 취약점을 보완해줄 수 있다. 이렇게 제조된 금/은 나노박스@실리카 나노 복합체의 촉매효율을 측정하기 위해 4-나이트로페놀 환원실험을 통해 촉해효율을 측정하였다. 속 빈 형태가 갖는 비표면적의 증강뿐만 아니라 속 빈 나노구조체에서만 관측되는 cage effect 이라는 특이한 특성으로 인해 속이 꽉찬 나노큐브에 비해 촉매효율이 상당히 높음을 입증하였다. pseudo-first-order kinetics, Arrhenius plot 그리고 Erying plot 을 통해 전이 상태의 착화합물의 안정도와 활성화 에너지를 구해 촉매 반응의 메커니즘을 심층적으로 밝혔다. 이와 더불어, 실리카 쉘로 금/은 나노박스를 보호하고 있기에 내구성의 증대도 높여 여러 번의 재사용 실험을 통해 촉매효율이 잘 유지됨을 보여주어 나노촉매제의 재사용 가능성도 시사하였다.

주요어: 이종접합, 하이브리드 나노구조체, 광촉매, 형광, 귀금속

학번: 2012-23049